SELF-ASSEMBLED ANISOTROPIC COLLOID SYSTEMS FOR PHOTONIC

APPLICATIONS

A Dissertation

Presented to the Faculty of the Graduate School

of Cornell University

In Partial Fulfillment of the Requirements for the Degree of

Doctor of Philosophy

by

Angela Carrier Stelson

January 2017

SELF-ASSEMBLED ANISOTROPIC COLLOID SYSTEMS FOR PHOTONIC
APPLICATIONS

Angela Carrier Stelson, Ph. D.

Cornell University 2016

Photonic crystals are optical structures periodic on the length scale of light, and

support useful attributes including photonic bandgaps (ranges of frequencies forbidden from

propagating in the material), negative refraction and slow light effects (extremely low group

velocity). Such effects have applications in sensors, waveguides, solid-state lighting,

photovoltaics and superlenses, among others. The optical characteristics of a photonic crystal

are determined by the interplay of structure, order and materials properties in the crystal. Self-

assembled anisotropic colloids are attractive templates for photonic crystals due to their cost

effectiveness and diversity of structures and symmetries. Introducing entropic and enthalpic

effects to engineer inter-particle interactions increases the variety of phases and mesophases in

anisotropic colloidal assemblies.

In this dissertation, the photonic properties of self-assembly inspired structures are

investigated *via* electromagnetic simulations. New paradigms for self-assembled photonic

crystals are developed, and desirable properties such as photonic bandgaps, negative

refraction, and slow light are correlated with structural and materials parameters informed by

colloidal assemblies. Specifically, the photonic crystal properties of partial order rotator

crystals, Archimedean tilings, and quasi-two dimensional 'slab' crystalline structures are

investigated. All three systems display large photonic bandgaps. Slow light effects are

observed in the rotator crystal and Archimedean tilings. As well, negative refractive index is

predicted in the 'slab' crystal and the Archimedean tiling. These projects open new frontiers for research to manipulate self-assembled systems for photonics.

Additionally, the assembly of colloidal C_{60} platelets is investigated under two-dimensional confinement and electric field. The C_{60} platelets are synthesized *via* a co-solvent precipitation method. The particles assemble under dipolar forces, dielectrophoretic forces, and electrohydrodynamic flows. Frequency-dependent phase transitions occur at the critical Maxwell-Wagner crossover frequency, where the effective polarizability of the particles in the medium is substantially reduced. Structures form as a function of field strength, frequency and confinement including hexagonal, oblique, string fluid, coexistent hexagonal-rhombic, and tetratic.

BIOGRAPHICAL SKETCH

Angela Carrier Stelson was born in Philadelphia, Pennsylvania on December 3rd, 1989 and grew up in Ann Arbor, Michigan and Roseburg, Oregon. She triple majored in Physics, Mathematics, and Political Science at the University of Oregon. During the summer of 2010, she completed an internship at Evonik Röhm GmbH where she implemented statistical methods to improve production of acrylic components for solar cells. From 2011 to 2012, she was a device engineering intern at Lattice Semiconductor Corporation, developing statistical algorithms to analyze defect data for semiconductor processing. She completed an undergraduate thesis under the guidance of Professor HoSang entitled "Affirmative Action and White Males: A Study on the Impacts of Framing". Under the guidance of Professor Gregory, she researched the optical emissions of sonoluminescence in an advanced undergraduate projects laboratory. She graduated *magna cum laude* with Honors in Physics and Political Science, and was nominated Phi Beta Kappa 'Oregon Six'. In 2012, she moved to Ithaca, New York to pursue a doctorate in Materials Science and Engineering as a Lester B. Knight Nanotechnology Fellow. She worked in the laboratory of Professor Chekesha Liddell Watson, investigating the electric field-directed assembly of colloids, and the photonic properties of self-assembled photonic crystals. She will move to Boulder, Colorado upon completing her degree to work as a National Research Council Research Associate at the Telecommunications Laboratory in the National Institute of Standards and Technology under Dr. James Booth.

To my family and friends who have supported and encouraged me through everything. To

Tony for your love, patience, and listening.

ACKNOWLEDGMENTS

This work would not have been possible without the support of a great number of people. First, I would like to thank my advisor, Professor Watson, whose teachings and passion for fostering her students' research made this possible. I would also like to thank my committee members, Professor Paulette Clancy and Professor Emmanuel Giannelis, for their support and assistance.

Thank you to all members of the Liddell Watson lab- Erin, Oath, Kenny, Sonny. Your scientific curiosity and insights were greatly appreciated. A special thanks to my undergraduate researcher, Wes, for the excellent 'crazy science' discussions and for your dedicated work. Many thanks to my 'unofficial scientific sounding board'- Teresa, Abby, and Jennie, for thoughtfully listening to my problems and providing innovative solutions. Many thanks to my collaborators- Carlos Avendano and James Stevenson- for answering all of my questions and giving excellent suggestions. I would also like to thank the stellar staff members of NBTC and CNF (Penny Burke, Teresa Porri, Brian Bowman, Jerry Drumheller, Aaron Windsor, and more) for helping me solve research problems, and lending a listening ear.

I would like to thank my friends and family, without which this would not have been possible. In particular, I would like to thank my mother, who never doubted me for a moment. Thanks to my father and uncles, who shared their love of science with me from an early age. To my friends in Ithaca- thank you for all of the fun times- you made grad school an unforgettable experience. To my friends, far away- Oanh, Carin, Alex B., Madi, Alex W.- thank you for letting friendships continue as if time and distance mean nothing. To Tony- you are my favorite, and I couldn't have done it without you.

TABLE OF CONTENTS

LIST OF FIGURES

LIST OF TABLES

CHAPTER 1

INTRODUCTION

Photonic Crystals to Glasses: Order-Dependent Properties

Photonic crystals are periodic structures on the length scale of light with interfaces between materials of varying dielectric constants. Reflections at such boundaries lead to constructive interference (allowed propagation of the electromagnetic wavelength) or destructive interference, forming a photonic band gap.[1] The light localization,[2] spontaneous emission suppression,[3] slow light[4] (i.e., extremely low group velocity) and anomalous refraction phenomena[5] in photonic crystals have been applied in sensors,[6] waveguides,[7] solid state lighting,[8] photovoltaics,[9] nonlinear optics,[10] and superlenses.[11] Tailored optical characteristics depend on the lattice constant, crystal structure, complexity of basis motifs, connectivity and filling fraction of materials, optical absorption, and refractive index contrast between spatial regions.[1] A challenge for the field is the coupling of structure-property predictions with ease of fabrication to fulfill the demands in frontier applications.

Recently, new paradigms have emerged predicting structures that may support large photonic band gaps without crystallinity. Specifically, the arrangements are distinguished by a structure factor S(k) tending toward zero as |k| approaches zero and include hyperuniform disordered structures,[12] continuous random networks,[13] icosahedral quasicrystals,[14] and Archimedean tilings.[15] These and other recent reports[16] suggest that neither periodicity nor quasi-periodicity is required for photonic bandgaps to form. Such arrangements support highly isotropic photonic bandgaps, unlike the common Bravais lattices. Isotropic bandgaps are desirable for free-form waveguides (i.e., line defects of arbitrary curvature),[12] flexible cavity designs,[17] and out-coupling across all incident angles from light emitting diodes,[18] as well as

supporting slow light effects.[4] Structures with greater disorder, e.g. random colloidal glasses, have been utilized as gain media in random lasers[19] and 'invisibility cloaks'.[20] The photonic properties of partial-order structures between crystals and glasses have hardly been explored.

Computational modeling of optical properties is commonly utilized to predict properties such as negative refraction and photonic band gaps in photonic crystals. Photonic modeling programs use the structure defined by the dielectric constants, basis shapes, and lattice pattern to solve Maxwell's Equations for the propagation of electromagnetic waves within the material.[21] Plane wave expansion programs such as MIT Photonic Bands (MPB) calculate the eigenvalues of the wave equation for nonhomogeneous materials:

$$\nabla \times \left(\frac{1}{\varepsilon(\mathbf{r})} \nabla \times \mathbf{H}(\mathbf{r}) \right) = \left(\frac{\omega}{c} \right)^2 \mathbf{H}(\mathbf{r})$$

(Equation 1.1)

This equation combines Maxwell's equations in the frequency domain, and explicitly assumes a Bloch wave function in a periodic structure with no absorption and magnetic permeability μ_o = 1. These assumptions are fulfilled for an ideal photonic crystal, and the eigenvalues $\omega(k)$ correspond to bands, or available modes, on a photonic band diagram. A range of frequencies with no modes corresponds to a photonic bandgap, as seen in the band diagram in Figure 1.1(a). By systematically changing the material and structural conformation of a crystal in the model (denoted by $\varepsilon(\mathbf{r})$ in the wave equation), the crystal's structural and photonic properties can be correlated.

Alternate methods of modelling electromagnetic fields in materials include finite difference time domain simulations, which propagate Maxwell's equations over time to numerically compute the propagation of a light source within a material. This technique is
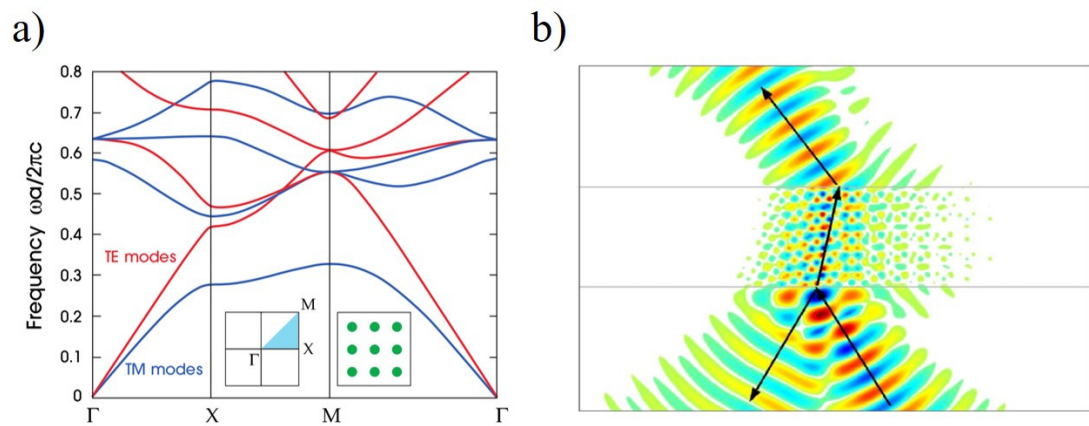
Figure 1.1 a) Representative photonic band diagram of a two-dimensional photonic crystal (structure as inset). Solutions ω(k) are plotted over the irreducible Brillouin zone (pictured in inset). A photonic bandgap exists between the TM modes. **b)** Finite difference time domain simulation of a Gaussian beam propagating through a photonic crystal (edges marked by black lines). The E_z component of the field is displayed as a heat map where red (blue) corresponds to positive (negative) E_z. Reproduced from references [1] and [22].

versatile, allowing for a wide variety of sources (plane waves, Gaussian beams, and point sources). Figure 1.1(b) displays a typical finite difference time domain simulation, where a Gaussian beam is propagated through a photonic crystal, displaying negative refraction. Because such simulations are conducted in the time domain, they are ideal for investigating the propagation properties of light in a material, and are used for photonic crystal properties such as negative refraction, slow light, and self-collimation.[4,23,24] Though these techniques were developed with crystalline structures in mind, the extension to disordered structures is straightforward by employing supercell methods, where a non-crystalline structure is approximated by a large 'unit cell' of disordered structure.[25]

Photonic Crystals: Challenges in Fabrication and Assembly

Multiple approaches have been used to address the fabrication challenge of generating three-dimensional photonic crystal structures including interference lithography,[26] biological templating,[27,28] and colloidal synthesis and self-assembly.[29–31] Interference lithography employs constructive interference between light sources impinging on a photoresist to etch unique patterns. This technique is complex and expensive, and requires simultaneous multiple laser focusing protocols.[26] Biological templating involves the infiltration of a multi-cellular structure with sol-gel precursors and initiating hydrolysis and condensation to generate an inverse template, then back-filling using a high refractive index material.[28] While this method is promising for generating intricate structures, problems exist in the fidelity of structures generated, and the ability to isolate structures in biological systems.

Colloidal synthesis and roll-to-roll processing present efficient approaches in terms of high yield particle creation for subsequent three-dimensional self-assembly processes. Colloidal synthesis relies on growth in solution to generate spheres and anisotropic shapes (i.e., sol-gel[32], hydrothermal[33,34] and co-solvent precipitations,[35,36] emulsion

polymerization[37–39]). An alternative to synthesis is particle replication in nonwetting

templates (PRINT),[40,41] where polymer solutions are cured in molds that define nonspherical

building block shapes. A wide range of atypical shapes are available through such methods

including peanut-shaped, mushroom cap, gear-shaped, hexagonal prisms, ellipsoids,

boomerangs, discs, etc. (Figure 1.2).[34,39,41–46] Strategies to access diverse arrangements of

particles include evaporation-assisted assembly,[44,47] electric and magnetic field assembly,[48–

53] and confinement-assisted assembly,[54–57] among others. Self-assembly of anisotropic

colloidal particles is an attractive method of achieving 'programmable' organization of

particles on the μm length scale, and provides fundamental insight into crystallization

thermodynamics. Self-assembly effects can be applied to anisotropic particle systems (e.g.,

dimers,[58] rods[59] and platelets[60]) to obtain a wide array of partial order mesophases and

complex crystal structures.

The structure of a self-assembled colloidal system is mainly determined by the

complex entropic and enthalpic interactions of individual colloidal particles with each other

and their environment. Application of an electric field across a colloidal solution induces

dipolar interactions that can influence the structure of colloidal system. An understanding of

the behavior of spherical particles under applied electric field has been developed for some

time, and simple close-packed hexagonal and face-centered cubic lattice, 2D and 3D photonic

crystals have been grown in electroplated glass cells.[50,61,62] Recently, great progress has been

made toward the understanding of anisotropic particle assembly under electric fields.[63,64]

Theoretical and experimental studies demonstrate the diverse phase behavior of many

different particle systems including dumbbells,[65,66] ellipsoids,[67,68] cubes,[69] rods,[48,70,71]

bowl-shaped particles,[72,73] and more. In particular, electric fields have been applied to induce

5
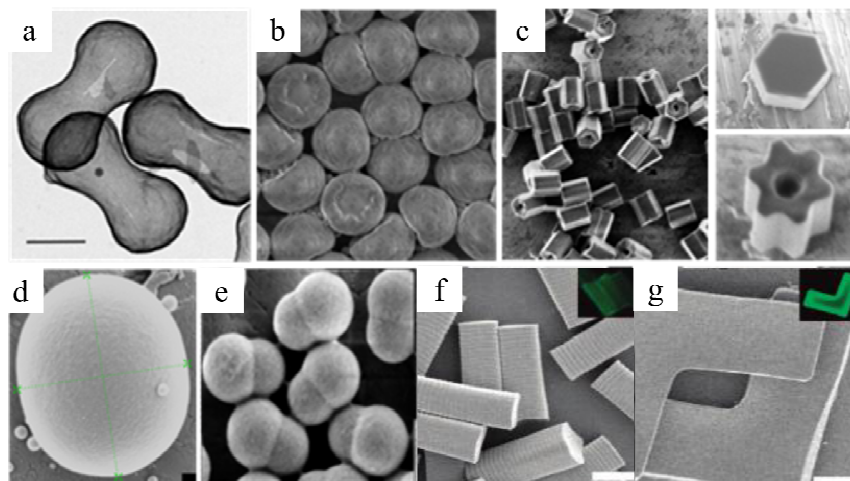
Figure 1.2 Anisotropic colloids manufactured by a variety of techniques for use in self-assembly. **a)** Hollow silica peanut-shaped particles synthesized *via* hydrothermal and sol-gel techniques. **b)** Polystyrene mushroom-cap shaped particles synthesized by emulsion-polymerization. **c)** C_{60} Gear-, flower-, and platelet-shaped particles formed by co-solvent precipitation. **d,e)** Polystyrene spherocylinders and pear-shaped particles fabricated with emulsion-polymerization. **f, g)** square rod- and cube-shaped colloids manufactured with PRINT. Reproduced from references [39–41,43,74].

martensitic transitions,[65] binary superlattices,[75] centered-rectangular monolayers,[67] string fluids,[41,76,77] liquid crystals,[68] and lock-and-key couplings[73] (see Figure 1.3). Anisotropic particle interactions can be theoretically explained by a variety of methods including coupled van der Waals models,[72,78] as well as simpler point-dipole approximations.[61,69,79] Additional forces can play a role in particle dynamics including dielectrophoretic forces, osmotic currents in the solvent, and polarization of electronic double layers. Typically, DC field directs particle flow parallel to electric field lines, while AC field drives particle motion perpendicular to the electric field lines. These forces are sensitive to experimental design and exhibit a complex frequency dependence, and are not taken into account in most theoretical treatments of anisotropic particle interactions under electric field.[61]

Assembling anisotropic particles under confinement incommensurate with the particle diameter can result in a rich diversity of phases due to entropic effects. For spherical particles, changes in confinement height allow for transitions from the hexagonal monolayer phase through buckled, rhombic, and prismatic phases into a square bilayer structure.[56,80] Anisotropic particle assemblies of peanut-, mushroom cap-, and ellipsoidal-shaped particles have displayed a wide array of structures including degenerate crystals and rotator phases.[55,81–83] Wedge confinement cells are a convenient method to access a continuous range of confinement heights and particle densities to control the excluded volume interactions that determine the lowest free energy configurations.[84]

Combinations of assembly mechanisms have been utilized to expand the library of structures available and improve control of particle position, orientation, and registry. Electric fields have been successfully employed with enthalpic patches and tuned double layer interactions, among others.[85,86] Additionally, a handful of studies explore two-dimensional assembly paired with magnetic fields.[87,88] However, combination of confinement and electric
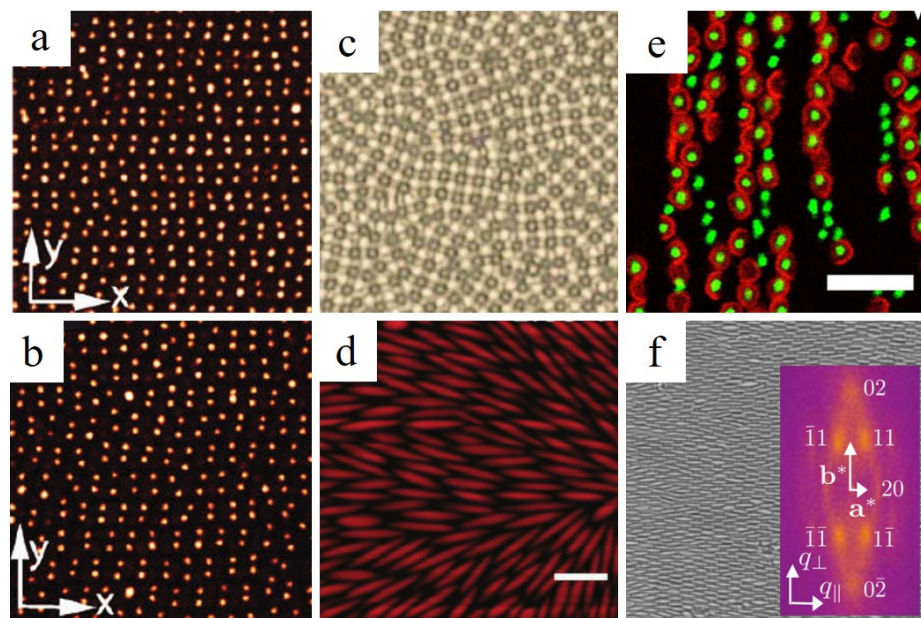
Figure 1.3 Structural diversity in anisotropic colloidal systems under electric field. **a, b)** Martensitic transition in dumbbell-shaped particles as a function of electric field strength. **c)** Square superlattice of binary sphere system under electric field. **d)** Nematic liquid crystal phase of colloidal ellipsoids. **e)** Lock-and-key interactions between spheres and bowl-shaped particles. **f)** Face-centered rectangular monolayers of ellipsoids. Figures reprinted from references [65,67,68,73,75].

field remains virtually unexplored[89] in anisotropic particle systems. The interplay of confinement, particle anisotropy, and electric field-induced forces results in a complex, dynamic system with enthalpic and entropic effects contributing to the assembly.

Thesis Outline

The computational component of this thesis work utilizes electromagnetic field simulations to correlate order, structure and photonic properties in self-assembly inspired photonic phases. Structural and materials parameters are varied (e.g. inter-particle spacing, particle anisotropy and refractive index) in keeping with established colloidal self-assembly techniques to map out the range of arrangements supporting desirable photonic properties. These studies are designed both to establish new design paradigms in the photonic crystal community, as well as to point self-assembly researchers toward high-payoff target structures. Specifically, plane-wave expansion and finite difference time domain simulations predict photonic properties including photonic bandgaps, slow light, negative refraction, and self-collimation of light.

To understand the impact of partial order in photonic crystals, the electromagnetic properties of photonic rotator crystals are predicted. Rotator crystals combine positional order and orientational disorder, and are found in diverse self-assembled colloidal systems.[82,86,90,91] This mesophase satisfies the S(k) criteria, and our findings demonstrate that orientational randomness can support large photonic bandgaps and slow light modes in waveguides. Within crystalline systems the impact of height variation in quasi-2D photonic crystals (photonic slabs) was explored in bilayers of cut-sphere particles. The particle model is based on collapsed spheres whose phase behavior was recently studied.[82] Bandgaps are found for a range of different assembly conditions and are attributed to Lorenz-Mie resonances in the basis shape. In addition, Archimedean tilings are studied, inspired by self-assemblies of

9

'patchy' square and triangle particle mixtures. These shape mixtures are semiregular tilings, as opposed to the common crystals, which are regular tilings (triangle or square). This system supports large photonic bandgaps, slow light and negative refraction leading to sub-wavelength imaging.

To enhance control of particle position, orientation, and registry in colloidal assemblies for photonic applications, anisotropic particles are self-assembled under two-dimensional confinement and electric field. The interplay of confinement, particle anisotropy and electric field-induced forces results in a dynamic system with enthalpic and entropic effects contributing to the assembly. *In situ* crystallization and mesophase formation of C_{60} microcrystal platelets was observed in the electric-field confinement cell and the phase behavior was characterized as a function of field strength, field frequency, particle packing fraction and confinement height. A wide variety of arrangements including string fluids, tetratic mesophases, and coexisting hexagonal-rhombic phases were found.

REFERENCES

[1]   R. D. Joannopoulos, John D., Johnson, Stephen G., Winn, Joshua N., Meade, *Molding the Flow of Light*, Princeton University Press, **2008**.

[2]   S. Fan, J. D. Joannopoulos, J. N. Winn, A. Devenyi, J. C. Chen, R. D. Meade, *J. Opt. Soc. Am. B* **1995**, *12*, 1267.

[3]   E. Yablonovitch, *Phys. Rev. Lett.* **1987**, *58*, 2059.

[4]   T. F. Krauss, *J. Phys. D. Appl. Phys.* **2007**, *40*, 2666.

[5]   Z.-Y. Li, L.-L. Lin, *Phys. Rev. B* **2003**, *68*, 245110.

[6]   S. A. Asher, S. F. Peteu, C. E. Reese, M. X. Lin, D. Finegold, *Anal. Bioanal. Chem.* **2002**, *373*, 632.

[7]   R. R. N. Simons, *Coplanar Waveguide Circuits, Components, and Systems*, **2001**.

[8]   C. Wiesmann, K. Bergenek, N. Linder, U. T. Schwarz, *Laser Photonics Rev.* **2009**, *3*, 262.

[9]   A. Mihi, F. J. López-Alcaraz, H. Míguez, *Appl. Phys. Lett.* **2006**, *88*, 193110.

[10]   B. Corcoran, C. Monat, C. Grillet, D. J. Moss, B. J. Eggleton, T. P. White, L. O'Faolain, T. F. Krauss, *Nat. Photonics* **2009**, *3*, 206.

[11]   R. Moussa, S. Foteinopoulou, L. Zhang, G. Tuttle, K. Guven, E. Ozbay, C. M.

Soukoulis, *Phys. Rev. B - Condens. Matter Mater. Phys.* **2005**, *71*, 1.

[12]   W. Man, M. Florescu, E. P. Williamson, Y. He, S. R. Hashemizad, B. Y. C. Leung, D. R. Liner, S. Torquato, P. M. Chaikin, P. J. Steinhardt, *Proc. Natl. Acad. Sci. U. S. A.* **2013**, *110*, 15886.

[13]   K. Edagawa, S. Kanoko, M. Notomi, *Phys. Rev. Lett.* **2008**, *100*, 13901.

[14]   X. Zhang, Z.-Q. Zhang, C. Chan, *Phys. Rev. B* **2001**, *63*, 81105.

[15]   D. Jovanović, R. Gajić, K. Hingerl, *Opt. Express* **2008**, *16*, 4048.

[16]   K. Edagawa, *Sci. Technol. Adv. Mater.* **2014**, *15*, 34805.

[17]   S. David, a. Chelnokov, J.-M. Lourtioz, *Opt. Lett.* **2000**, *25*, 1001.

[18]   M. Rattier, H. Benisty, E. Schwoob, C. Weisbuch, T. F. Krauss, C. J. M. Smith, R. Houdré, U. Oesterle, *Appl. Phys. Lett.* **2003**, *83*, 1283.

[19]   J. F. Galisteo-López, M. Ibisate, R. Sapienza, L. S. Froufe-Pérez, A. Blanco, C. López, *Adv. Mater.* **2011**, *23*, 30.

[20]   R. Schittny, M. Kadic, T. Bueckmann, M. Wegener, *Science (80-.).* **2014**, *345*, 427.

[21]   S. G. Johnson, J. D. Joannopoulos, *Opt. Express* **2001**, *8*, 173.

[22]   R. Moussa, B. Wang, G. Tuttle, T. Koschny, C. Soukoulis, *Phys. Rev. B* **2007**, *76*, DOI 10.1103/PhysRevB.76.235417.

[23]   D. Roundy, D. Roundy, M. Ibanescu, M. Ibanescu, P. Bermel, P. Bermel, "MIT

Electromagnetic Equation Propogation," can be found under http://ab-initio.mit.edu/~meep/meep.pdf, **2005**.

[24] D. W. Prather, S. S. S. Shi, J. Murakowski, G. J. Schneider, a. Sharkawy, C. C. C. Chen, B. M. B. Miao, *IEEE J. Sel. Top. Quantum Electron.* **2006**, *12*, 1416.

[25] L. Wu, F. Zhuang, S. He, *Phys. Rev. E* **2003**, *67*, DOI 10.1103/PhysRevE.67.026612.

[26] P. E. L. T. Dr. Martin Maldovan, P. Materials, *Periodic Materials and Interference Lithography: For Photonics, Phononics and Mechanics*, **2009**.

[27] B. A. Dong, Y. Wang, Y. Tang, N. Ren, Y. Zhang, Y. Yue, Z. G. Crystalline, **2002**, 926.

[28] J. W. Galusha, M. R. Jorgensen, M. H. Bartl, *Adv. Mater.* **2010**, *22*, 107.

[29] A.-P. Hynninen, J. H. J. Thijssen, E. C. M. Vermolen, M. Dijkstra, A. van Blaaderen, *Nat. Mater.* **2007**, *6*, 202.

[30] F. Meseguer, *Colloids Surfaces A Physicochem. Eng. Asp.* **2005**, *270*, 1.

[31] Y. Xia, B. Gates, Z. Y. Li, *Adv. Mater.* **2001**, *13*, 409.

[32] W. Stöber, A. Fink, E. Bohn, *J. Colloid Interface Sci.* **1968**, *26*, 62.

[33] X. Chuai, X. Guo, X. Liu, G. He, K. Zheng, C. He, W. Qin, *Opt. Mater. (Amst).* **2015**, *44*, 13.

[34] S. H. Lee, C. M. Liddell, *Small* **2009**, *5*, 1957.

[35] †,‡ Heng-Xing Ji, † Jin-Song Hu, †,‡ Qing-Xin Tang, † Wei-Guo Song, †
      Chun-Ru Wang, † Wen-Ping Hu, *,† and Li-Jun Wan, § Shuit-Tong Lee*,
      2007, DOI 10.1021/JP071912R.

[36] S. J. Penterman, C. M. Liddell Watson, *CrystEngComm* **2016**, *18*, 1775.

[37] M. Okubo, H. Minami, *Macromol. Symp.* **2000**, *150*, 201.

[38] C. I. Zoldesi, C. A. Van Walree, A. Imhof, *Langmuir* **2006**, *22*, 4343.

[39] E. Y. K. Fung, K. Muangnapoh, C. M. Liddell Watson, *J. Mater. Chem.* **2012**,
      22, 10507.

[40] M. J. Hampton, S. S. Williams, Z. Zhou, J. Nunes, D. H. Ko, J. L. Templeton,
      E. T. Samulski, J. M. DeSimone, *Adv. Mater.* **2008**, *20*, 2667.

[41] K. P. Herlihy, J. Nunes, J. M. Desimone, *Langmuir* **2008**, *24*, 8421.

[42] L. Xu, H. Li, X. Jiang, J. Wang, L. Li, Y. Song, L. Jiang, *Macromol. Rapid
      Commun.* **2010**, *31*, 1422.

[43] S. J. Penterman, A. Singh, W. R. Zipfel, C. M. Liddell Watson, *Adv. Opt.
      Mater.* **2014**, *2*, 1024.

[44] S. R. J. Oliver, N. Bowden, G. M. Whitesides, *J. Colloid Interface Sci.* **2000**,
      224, 425.

[45] A. Fernández-Nieves, G. Cristobal, V. Garcés-Chávez, G. C. Spalding, K.
      Dholakia, D. a. Weitz, *Adv. Mater.* **2005**, *17*, 680.

[46] J. Jeong, W. S. Kim, S. I. Park, T. S. Yoon, B. H. Chung, *J. Phys. Chem. C* **2010**, *114*, 12976.

[47] L. Malaquin, T. Kraus, H. Schmid, E. Delamarche, H. Wolf, *Langmuir* **2007**, *23*, 11513.

[48] A. Kuijk, T. Troppenz, L. Filion, A. Imhof, R. van Roij, M. Dijkstra, A. van Blaaderen, *Soft Matter* **2014**, *10*, 6249.

[49] C. . Chaffey, S. . Mason, *J. Colloid Sci.* **1964**, *19*, 525.

[50] M. Janjua, S. Nudurupati, P. Singh, N. Aubry, *Electrophoresis* **2011**, *32*, 518.

[51] Y. Zhang, L. Sun, Y. Fu, Z. C. Huang, X. J. Bai, Y. Zhai, J. Du, H. R. Zhai, *J. Phys. Chem. C* **2009**, *113*, 8152.

[52] J. W. Swan, J. L. Bauer, Y. Liu, E. M. Furst, *Soft Matter* **2014**, *10*, 1102.

[53] D. V. Byelov, J.-M. Meijer, I. Snigireva, A. Snigirev, L. Rossi, E. van den Pol, A. Kuijk, A. Philipse, A. Imhof, A. van Blaaderen, G. J. Vroege, A. V. Petukhov, *RSC Adv.* **2013**, *3*, 15670.

[54] S. A. Rice, *Chem. Phys. Lett.* **2009**, *479*, 1.

[55] K. Muangnapoh, C. Avendaño, F. a. Escobedo, C. M. Liddell Watson, *Soft Matter* **2014**, *10*, 9729.

[56] F. Ramiro-Manzano, E. Bonet, I. Rodriguez, F. Meseguer, *Phys. Rev. E* **2007**, *76*, DOI 10.1103/PhysRevE.76.050401.

[57] M. Schmidt, H. Löwen, *Phys. Rev. E* **1997**, *55*, 7228.

[58] S. H. Lee, E. Y. Fung, E. K. Riley, C. M. Liddell, *Langmuir* **2009**, *25*, 7193.

[59] M. Kotera, J. M. Lehn, J. P. Vigneron, *J. Chem. Soc. Chem. Commun.* **1994**, *5*, 197.

[60] K. Zhao, C. Harrison, D. Huse, W. B. Russel, P. M. Chaikin, *Phys. Rev. E - Stat. Nonlinear, Soft Matter Phys.* **2007**, *76*, 1.

[61] O. D. Velev, in *Colloids Colloid Assem.* (Ed: F. Caruso), **2004**, pp. 437–464.

[62] S. O. Lumsdon, E. W. Kaler, O. D. Velev, *Langmuir* **2004**, *20*, 2108.

[63] H. Loewen, *Eur. Phys. J. Spec. Top.* **2013**, *222*, 2727.

[64]   a. Blaaderen, M. Dijkstra, R. Roij, A. Imhof, M. Kamp, B. W. Kwaadgras, T. Vissers, B. Liu, *Eur. Phys. J. Spec. Top.* **2013**, *222*, 2895.

[65] A. F. Demirörs, P. M. Johnson, C. M. van Kats, A. van Blaaderen, A. Imhof, *Langmuir* **2010**, *26*, 14466.

[66] F. Ma, S. Wang, L. Smith, N. Wu, *Adv. Funct. Mater.* **2012**, *22*, 4334.

[67] J. P. Singh, P. P. Lele, F. Nettesheim, N. J. Wagner, E. M. Furst, *Phys. Rev. E. Stat. Nonlin. Soft Matter Phys.* **2009**, *79*, 50401.

[68] A. A. Shah, H. Kang, K. L. Kohlstedt, K. H. Ahn, S. C. Glotzer, C. W. Monroe, M. J. Solomon, *Small* **2012**, *8*, 1551.

[69] H. R. Vutukuri, F. Smallenburg, S. Badaire, A. Imhof, M. Dijkstra, A. van

Blaaderen, *Soft Matter* **2014**, *10*, 9110.

[70]   T. Troppenz, A. Kuijk, A. Imhof, A. van Blaaderen, M. Dijkstra, R. van Roij, *Phys. Chem. Chem. Phys.* **2015**, 22423.

[71]   T. Troppenz, L. Filion, R. Van Roij, M. Dijkstra, *J. Chem. Phys.* **2014**, *141*, DOI 10.1063/1.4897562.

[72]   B. W. Kwaadgras, M. Verdult, M. Dijkstra, R. Van Roij, *J. Chem. Phys.* **2011**, *135*, DOI 10.1063/1.3637046.

[73]   M. Kamp, N. A. Elbers, T. Troppenz, A. Imhof, M. Dijkstra, R. van Roij, A. van Blaaderen, *Chem. Mater.* **2016**, acs. chemmater.5b04152.

[74]   S. H. Lee, S. J. Gerbode, B. S. John, A. K. Wolfgang, F. A. Escobedo, I. Cohen, C. M. Liddell, *J. Mater. Chem.* **2008**, *18*, 4912.

[75]   W. Ristenpart, I. Aksay, D. Saville, *Phys. Rev. Lett.* **2003**, *90*, 128303.

[76]   O. D. Velev, K. H. Bhatt, *Soft Matter* **2006**, *2*, 738.

[77]   D. J. Klingenberg, F. Van Swol, C. F. Zukoski, *J. Chem. Phys.* **1989**, *91*, 7888.

[78]   B. W. Kwaadgras, M. Dijkstra, R. Van Roij, *J. Chem. Phys.* **2012**, *136*, DOI 10.1063/1.3701615.

[79]   M. Mittal, P. P. Lele, E. W. Kaler, E. M. Furst, *J. Chem. Phys.* **2008**, *129*, 64513.

[80]   F. Ramiro-Manzano, E. Bonet, I. Rodriguez, F. Meseguer, *Soft Matter* **2009**, *5*,

4279.

[81]   I. D. Hosein, C. M. Liddell, *Langmuir* **2007**, *23*, 10479.

[82]   E. K. Riley, C. M. Liddell, *Langmuir* **2010**, *26*, 11648.

[83]   Z. Zheng, R. Ni, F. Wang, M. Dijkstra, Y. Wang, Y. Han, *Nat. Commun.* **2014**, *5*, 3829.

[84]   B. Pieranski, Pa., Strzelecki, L., Pansu., *Phys. Rev. Lett.* **1983**, *50*, 900.

[85]   S. Gangwal, O. J. Cayre, O. D. Velev, *Langmuir* **2008**, *24*, 13312.

[86]   B. Liu, T. H. Besseling, M. Hermes, A. F. Demirörs, A. Imhof, A. van Blaaderen, *Nat. Commun.* **2014**, *5*, 3092.

[87]   W. Wen, L. Zhang, P. Sheng, *Phys. Rev. Lett.* **2000**, *85*, 5464.

[88]   N. Osterman, D. Babič, I. Poberaj, J. Dobnikar, P. Ziherl, *Phys. Rev. Lett.* **2007**, *99*, 1.

[89]   T. Gong, D. W. M. Marr, *Langmuir* **2001**, *17*, 2301.

[90]   I. D. Hosein, B. S. John, S. H. Lee, F. a. Escobedo, C. M. Liddell, *J. Mater. Chem.* **2009**, *19*, 344.

[91]   U. Agarwal, F. a Escobedo, *Nat. Mater.* **2011**, *10*, 230.

CHAPTER 2

COMPLETE PHOTONIC BANDGAPS IN SELF-ASSEMBLED SQUARE

BILAYER STRUCTURES[*1]

Introduction

Materials with photonic bandgap properties offer improvements in applications requiring enhanced optical control including slow-light waveguides,[1] flat lenses,[2] solar cells,[3] optical integrated circuits,[4] micro-cavities,[5] and optoelectronic devices.[6] Lithographic methods for generating structures have been extensively developed, enabling the generation of photonic crystals (PCs) with two-dimensional (2D) periodicity.[4] The extension of lithographic engineering into three-dimensional structures using holographic techniques is limited by the complexity in optical setups required to produce the necessary interference patterns. Additionally, lithographic processes have manufacturing limitations of feature size and sample area, expensive equipment, and clean room environments.[7] Self-assembled colloidal systems offer an attractive alternative to lithographic methods due to their scalability and cost-effectiveness.[8]

PCs supporting simultaneous even and odd mode (i.e., complete) bandgaps can be promoted by reduced symmetry or increased basis complexity to eliminate degeneracies at high symmetry points for two-dimensional (2D) systems.[9] In the latter case, architectures may be designed with isolated high dielectric constant scatterers and continuous matrices to promote large, overlapping TM (transverse magnetic) and TE (transverse electric) band gaps. For instance, annular scatterers with high dielectric cores in a high dielectric matrix supported bandgaps up to $\Delta\omega/\omega_{mid\text{-}gap} = 10\%$.[10] Utilizing anisotropic basis shapes in PCs reduces lattice

symmetry and can open complete bandgaps. For instance, rotating square cross-section pores 32° from the lattice translation vectors opened a bandgap with a maximum value of gap-to-midgap ratio, $\Delta\omega/\omega_{mid\text{-}gap}$ = 13.8%. In addition, a bandgap of size $\Delta\omega/\omega_{mid\text{-}gap}$ = 15.6% was found for a square lattice decorated with square cross-section motifs rotated 27° degrees and circular cross-section pores in the interstitial sites.[11]

Quasi-two-dimensional photonic crystal slabs provide an opportunity for further structural variation in the third dimension. Light is contained within the slab plane via total internal reflection. Slab structures capture the true height limitations in fabricated systems, but the size reduction in the z-direction increases the difficulty of obtaining complete bandgaps. Slab PCs with circular cross-section pores in a square lattice were investigated and no complete bandgaps were found for direct (i.e. high dielectric particle with air matrix) or inverted (i.e. high dielectric matrix with air pore) structures.[12] A rotated, square cross-section pore basis reduced the symmetry of the arrangement and resulted in a complete bandgap of size $\Delta\omega/\omega_{mid\text{-}gap}$ = 8.8% between the 4th and 5th bands.[13] In general, slab bandgap sizes are more modest as compared to infinite height (2D) bandgaps. The champion slab structure ($\Delta\omega/\omega_{mid\text{-}gap}$ = 15%) incorporated anisotropic dielectric constants from Tellurium and liquid crystals in circular cross-section pores on a hexagonal lattice.[14] The complexity of fabrication with the necessary materials parameters prohibits realization of the slab.

Colloidal self-assembly of anisotropic particles provides a mechanism for diverse structures with reduced symmetry in 3D and quasi-2D structures. Colloidal crystals can be utilized as templates for high dielectric material to prepare structures that promote photonic bandgaps at optical and telecommunications frequencies. The diversity of monodisperse particles available— including spherocylinder,[15] boomerang,[16] mushroom cap,[17] hexagonal prism,[18] square-cross,[19] bowl-shaped,[20] peanut,[21]— provide a rich variety of anisotropic

bases. Self-assembly strategies to access diverse arrangements of particles include evaporation-assisted assembly,[22] electric and magnetic field assembly,[23,24] and confinement-assisted assembly,[25] among others. In particular, assembly of colloidal suspensions in wedge confinement cells has allowed access to phases with quasi-2D geometry as a function of gap height.[26] Simulations of such quasi-2D phases- including centered rectangular dimer[27] and buckled mushroom cap structures[28] predict polarization dependent bandgaps up to $\Delta\omega/\omega_{mid-gap}$ = 19.3% and complete bandgaps up $\Delta\omega/\omega_{mid-gap}$ = 7.9% in the presence of moderate to high Brillouin zone isotropy (i.e. approaching square or hexagonal symmetry).

Here, we examine the photonic bandgap properties of the square bilayer (2□) structure formed of 75% cut height spheres as depicted in Figure 2.1(a) and 1(b). This structure is predicted to be thermodynamically stable[29] and has been realized experimentally using wedge cell confinement with anisotropic colloidal particles.[26] This square bilayer structure combines high rotational symmetry, complex basis shape and vertical cross-section variation. We explore the impact of structural deformation on the photonic bandgap properties by varying the slab height in the range of the particle diameter. A large polarization-independent gap (i.e., maximum gap size 10.2%) was found for the direct structure. This gap between the tenth and eleventh bands (10-11) is stable over a range of heights and dielectric constants and is maximized around ε_r=12. In the inverted structure, we find simultaneous polarization-independent gaps between the fourth and fifth (4-5), and the eighth and ninth (8-9) bands in the slab-guided wave vector region. Analysis of the equifrequency contours (EFCs) revealed right-handed negative refraction in the second band for the direct square bilayer structure.

Computational Methods
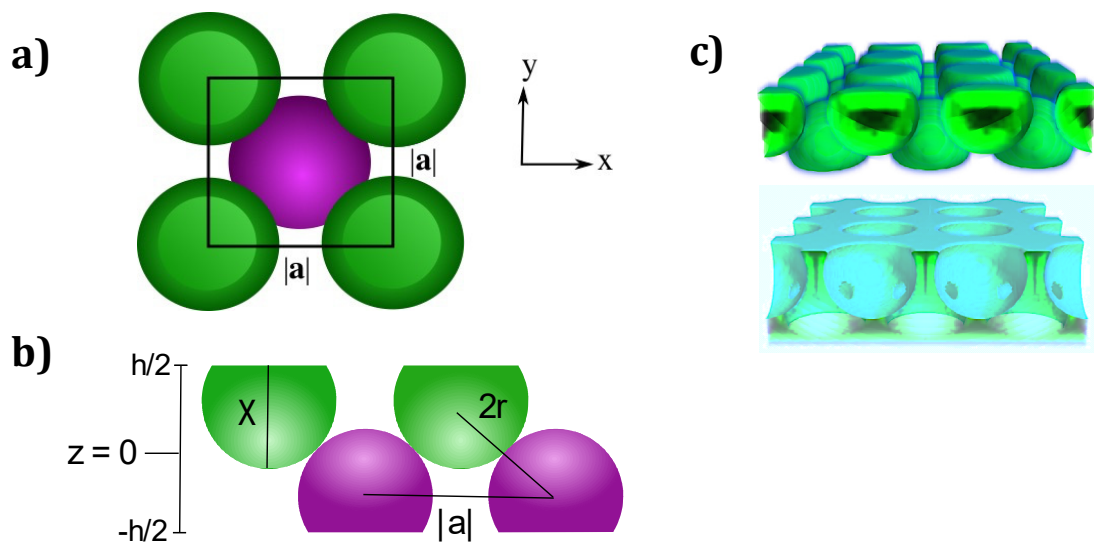
Figure 2.1. Model of the 2□, χ = 0.75 structure. (a) Cross-sectional view along [0 0 1]. (b) Square unit cell viewed along [1 0 0]. (c) Images of direct and inverted slab structures for h = 1.0.

The photonic band structure of the slab 2□ phase was calculated using the MIT Photonic

Bands (MPB) software package. The model for the cut sphere morphology was a truncated

sphere, with cut height χ defined as the fraction of a sphere diameter. The particles were

arranged in a square lattice with a two-particle basis yielding a 2□ phase (Figure 2.1). The

plane group symmetry of the arrangement was 4mm. The simulated slab heights (h, for 75%

cut height spheres) for the 2□ phase were in the range 1.8r to 2.1r. The lattice vector was

determined by the slab height and the particle tangency. The latter ensured that the

neighboring cut spheres were tangent. The lattice constant was given by

$|a| = 2\sqrt{2r^2 - \frac{(h-r)^2}{2}}$ with $|a_1|[1\ 0\ 0] = |a_2|[0\ 1\ 0] = |a|$. The cut spheres were centered

at $(0, 0, \frac{r}{2} - \frac{h}{2})$ and $(\frac{|a|}{2}, \frac{|a|}{2}, -\frac{r}{2} + \frac{h}{2})$ in Cartesian coordinates, with the cut face oriented toward

the edges of the slab. We varied the filling fraction while maintaining the sphere conformation

by decreasing the anisotropy of the particles (i.e., increasing χ). The cut fraction was varied

between 0.6 and 0.89, and the resulting slab height is given by $h_{eff} = h-2(0.75-χ)$.

A simulation path along the high symmetry points of the two-dimensional irreducible

Brillouin zone was employed [Figure 2.1(c)] to calculate the dispersion curves of light

frequency versus wave-vector. One hundred points were interpolated between the high

symmetry points and the first twenty solutions were evaluated within a 0.001% convergence

tolerance. A vertical spacing equal to eight times the slab height was included in the three-

dimensional simulation so that the mode frequencies were constant within ± 0.001% as a

function of the spacing. The band diagram is overlaid with a light cone (opaque light gray

region), corresponding to bulk background radiation. To calculate the lower limit of the light

cone, the magnitude of the wave-vector is divided by the refractive index of the air cladding (n

= 1). The results are polarization independent due to the lack of mirror-plane symmetry

through the z = 0 plane. A grid resolution of |**a**|/16 (|**a**|/32) yielded a typical minimum of 4096 (32768) plane waves. A mesh size of 5 was employed for averaging the dielectric constant between grid points. Guided modes were evaluated for the direct and inverted structures with ε_r from 6 to 16. Equifrequency contours were produced by interpolating mode frequencies calculated by MPB.

Results and Discussion

Figure 2.2 shows the band diagram for a square bilayer with slab height of 1.0, cut fraction of 0.8 and dielectric contrast of 12 (Si). Gray shading above the light cone represents all bulk background radiant frequencies. The complete bandgap lies between the 10th and 11th bands in the unrestricted wave vector region below the light cone shoulder. Guided modes span a highly limited range of the Brillouin zone above the light cone shoulder. The complete bandgap size reaches $\Delta\omega/\omega_{mid\text{-}gap} = 10.2\%$ and is centered at a mid-gap frequency of $\omega|\mathbf{a}|/2\pi c = 0.352$.

A contour map of gap size as a function of slab height and dielectric contrast is depicted in Figure 2.3(a) for the 10-11 bandgap at a cut fraction of 0.75. We vary the slab height to mimic self-assembly of cut sphere shapes under a range of confinement heights. The bandgap is large for a range of slab heights (h = 0.95-1.05) and dielectric contrasts ($\varepsilon_r = 10\text{-}16$). The maximum bandgap size of 8.7% occurs for $\varepsilon_r = 11\text{-}12$ and h = 1.0. The minimum dielectric contrast value that still supports the bandgap ($\Delta\omega/\omega_{mid\text{-}gap} = 1.7\%$ at h = 1.05) is $\varepsilon_r = 7$. A wide range of high dielectric constant materials can be used in this arrangement including rutile TiO_2, II-VI and III-V semiconductors as well as elemental semiconductors.

The impact of varying cut fraction on the bandgap size is plotted in Figure 2.3(b) for the largest bandgap structure (h = 1.0, $\varepsilon_r = 12$). We varied the cut fraction with no conformation change. As χ was varied from 0.75 to 0.8 the bandgap size increased from 8.2%
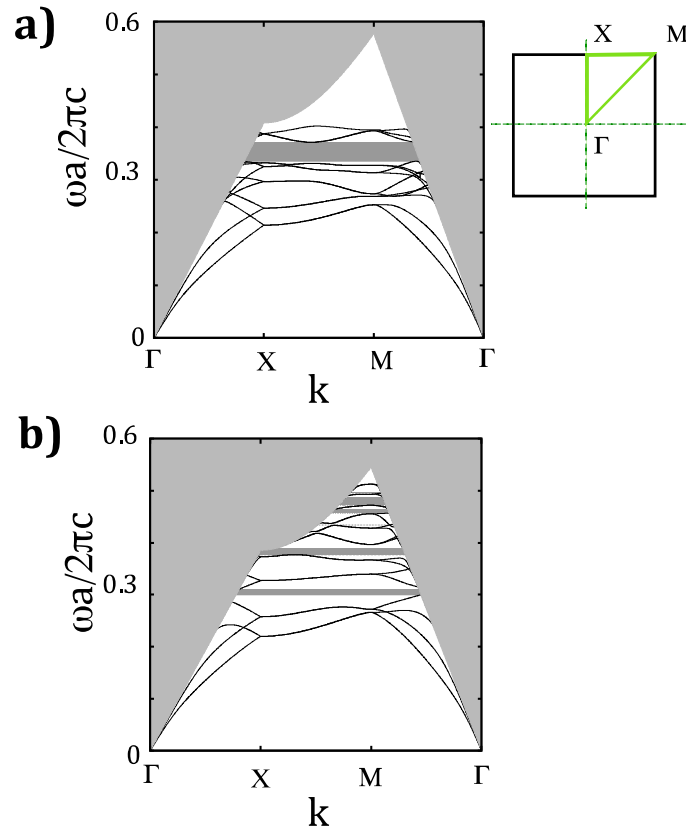
Figure 2.2. (a) Band diagram of direct structure with h = 1.0, χ = 0.80 and ε_r = 12. Inset at right is the Brillouin zone of a square lattice, with the high symmetry points M, X and Γ marked in the irreducible Brillouin zone. (b) Band diagram of inverted structure with h=0.9, χ = 0.75 and ε_r = 12. Light gray shading above the light cone represents all bulk background radiant frequencies

27

a)

b)
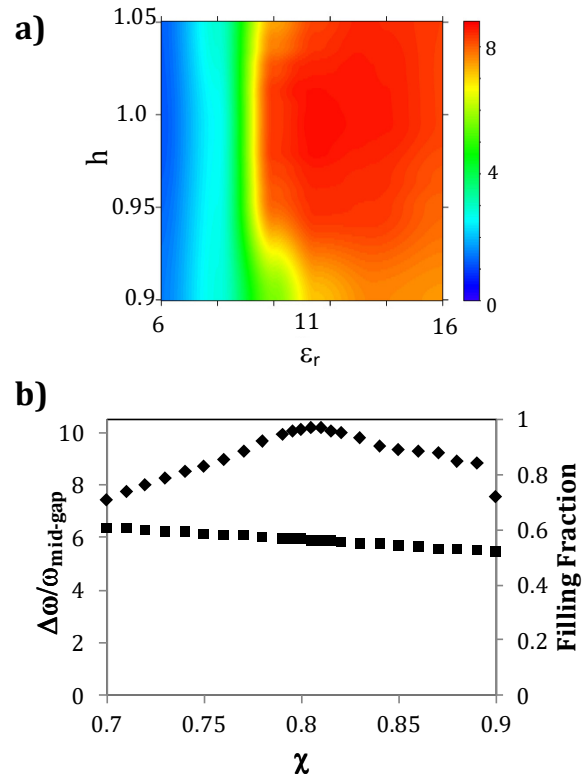
Figure 2.3. (a) Contour map of the gap size for the 10-11 gap in the direct structure. (b) The impact of cut fraction on the gap size (diamonds) and filling fraction χ (squares). The lattice parameters are constant.

to 10.2%. Modifying the cut fraction implicitly changes the filling fraction $\eta = \frac{V_{dielectric}}{V_{unit\ cell}}$;

however, the change in filling fraction over this region was less than 5%. This indicates that

the shape factor of the particle and the slab height are significant in widening the bandgap.

Typically, lower dielectric filling fraction increases the size of the bandgap,[30] but here the

bandgap size drops off after $\chi = 0.8$ ($\eta = 0.568$) down to 8.8% at $\chi = 0.89$ ($\eta = 0.526$).

We examine the field concentrations in the direct square bilayer structure to establish

the mechanism of bandgap formation. The displacement field distributions (i.e., dielectric

contrast multiplied by the electric field) at the X point for the lower- and upper- bounding

bands of the direct bandgap are shown in Figure 2.4 for different degrees of particle

anisotropy. The particle outlines are shown to aid visualization of the field distribution in the

structure. With respect to the center of the slab plane, the displacement field modes do not

display mirror-plane symmetry and thus are inseparable into even and odd modes.[12]

The bandgap is largest at $\chi = 0.80$ where the maximum shift in field density occurs for

the bands constraining the gap.[28,31] At this intermediate cut fraction, the density of the lower

band is distributed in a ring-shaped mode in the y-z plane of the particles, while the upper

band displays complementary dual node distributions (i.e., two nodal surfaces) in both particle

orientations [Figures 2.4(b) and 2.4(e)]. Both mode fields are concentrated in the high

dielectric. This is in contrast to other findings, where bandgaps are maximized between modes

contained in the dielectric and higher energy modes concentrated in air.[10] At $\chi = 0.7$, the

energy density is focused in the central slab region for the band below the bandgap [Figure

2.4(a)]. The eigenmode above the bandgap [Figure 2.4d] is concentrated in the lower layer of

cut spheres (i.e., particle with cut-face oriented down) and also has a dual node distribution.

The bandgap is more modest at these cut fractions. For $\chi = 0.89$, the structures have

displacement density distributed in rings for the low energy mode, similar to $\chi = 0.80$. In the
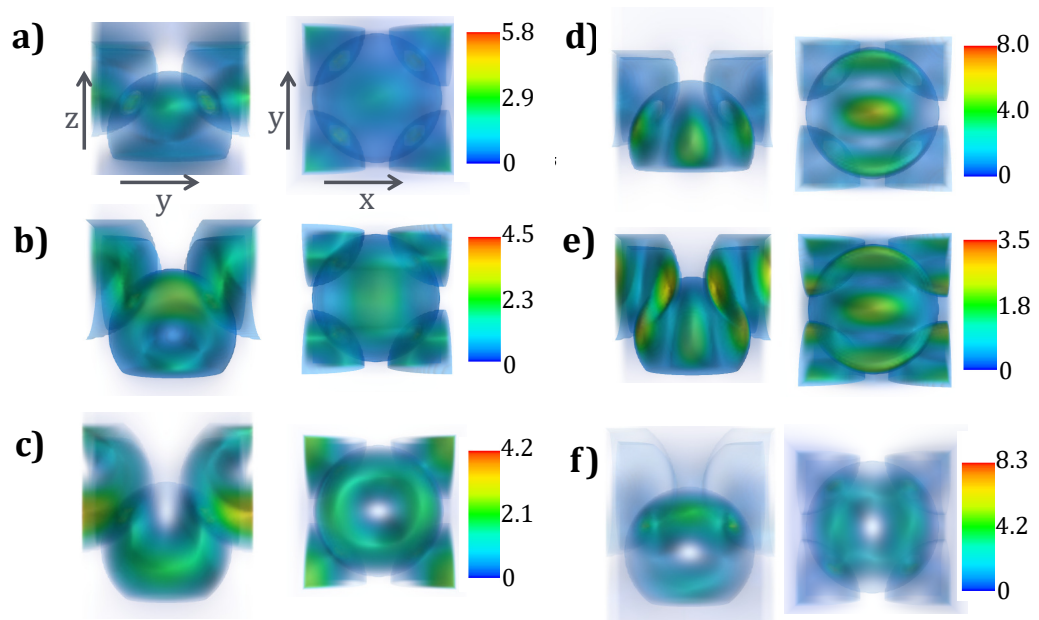
Figure 2.4. Electric displacement field density in the direct structure for (a, d) $\chi = 0.70$, (b, e) $\chi = 0.80$, and (c, f) $\chi = 0.89$, Field densities for (a-c) band 10 and (d-f) band 11 are displayed along [1 0 0] (left) and [0 0 1] (right).

upper band the decrease in particle anisotropy supports a mode with the field concentrated only in the lower layer of particles. Together this suggests that the band gap arises due to a significant Bragg scattering component because Lorenz-Mie resonances should be insensitive to particle anisotropy.[32]

To compare the photonic properties for a square bilayer crystal prepared by self-assembly[26] and the model employed here, the effect of the cut sphere and the colloidal mushroom cap morphologies on bandgap size is illustrated in Figure 2.5. Both experiment and simulation use similar anisotropic bases. The band diagrams for structure parameters $\chi = 0.75$, h = 1.0 and materials parameter $\varepsilon_r = 12$ are shown for the horned mushroom cap (Figure 2.5a) and cut-sphere (Figure 2.5b). The mushroom cap is modeled as a toroid with minor radius of r/2 and major radius of r, where r is the hemisphere radius.[28] This yields a particle height equivalent to a $\chi = 0.75$ cut sphere. For the same conformation, the bandgap size was nearly the same (i.e., a change of only 0.02%). As well, the band diagram is largely unchanged. In comparison, mushroom cap particles in buckled conformations have smaller bandgaps,[28] which can be attributed to the reduction in isotropy of the irreducible Brillouin zone from square to rectangular.[33]

The inverted structure supports two coexisting gaps between the 4-5 bands and the 8-9 bands. A representative band diagram (h = 0.9, $\varepsilon_r = 12$) is shown in Figure 2.2(c). Both bandgaps lie below the restricted k-vector region of the light cone, and are bounded by anisotropic bands. Figure 2.6 provides a map of the gap sizes for the 4-5 and 8-9 gaps as a function of slab height and dielectric constant. For the 8-9 gap, as the slab height increases the 11th band dips below the 9th band in frequency, and becomes the limiting feature for the bandgap. The 4-5 and 8-9 gaps are maximized in complimentary regions of the h-ε_r parameter space, which indicates gap competition.[28] The 4-5 gap is maximized at high dielectric
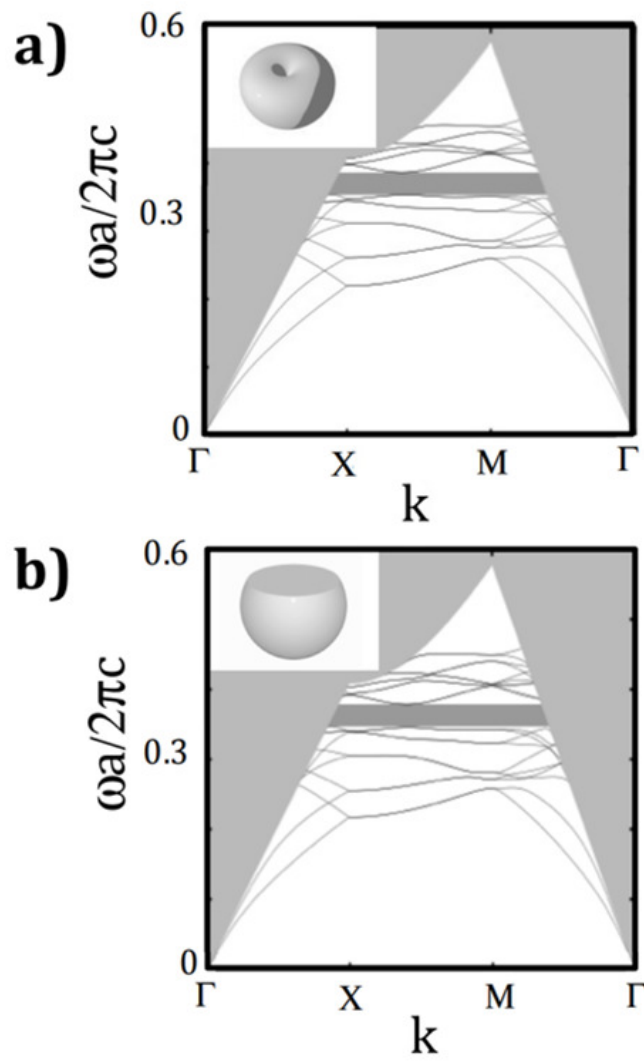
Figure 2.5. Band diagrams for (a) mushroom cap particles and (b) cut spheres with $\chi = 0.75$. Both structures are calculated for $h = 1.0$ and $\varepsilon_r = 12$. Images of the structures are inset
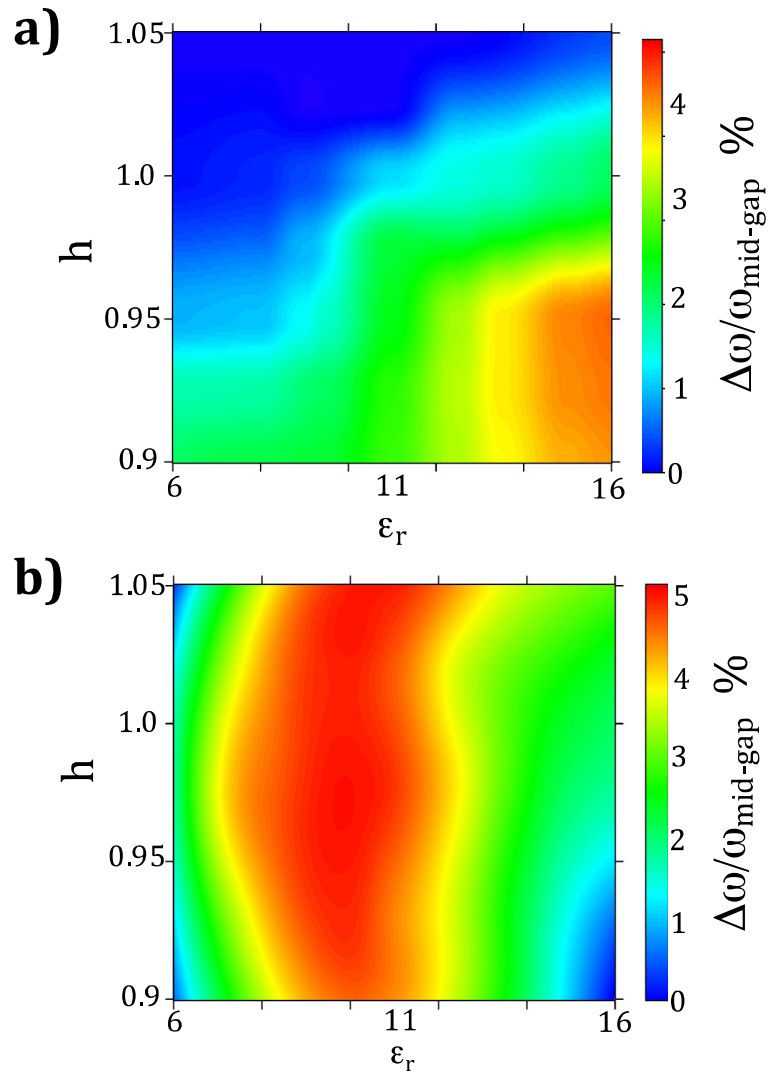
Figure 2.6. Contour map of the gap sizes for (a) 4-5 gaps and (b) 8-9 gaps in inverted structures with ε_r varied from 6 to 16 and height varied from 0.9 to 1.05. Gaps between bands 8-9 and 8-11 are plotted together in (b).

contrast and low slab height ($\Delta\omega/\omega_{\text{mid-gap}}$ = 5% for h = 0.95, ε_r = 16) and the 8-9 gap opens at

low to moderate dielectric contrast ($\Delta\omega/\omega_{\text{mid-gap}}$ = 5.2% for h = 0.95, ε_r = 9). Structures with

multiple bandgaps may be desirable for applications such as synchronous manipulation of

distinct signals.[34,35]

In addition to bandgaps, band curvature can promote useful properties such as

refraction and slow light. Specifically, refraction properties enable applications including flat

lensing and sub-wavelength imaging.[2] The refraction properties of the direct structure with h

= 1.0, ε_r = 12 and χ = 0.75 are depicted in Figure 2.7. Figure 2.7(a) displays the equifrequency

contour (EFC) of the second band. The concave contours with inward gradients are observed

around the Γ high symmetry point, suggesting negative refraction for a range of incident

angles.[36] Figure 2.7(b) displays the EFC contour analysis for $\omega|\mathbf{a}|/2\pi c$ = 0.225 with an

incidence angle of 45 degrees on the ΓM surface. The incident k-vector magnitude is defined

as $|k_{\text{incident}}|$ = $\omega|\mathbf{a}|/2\pi c$. For photonic crystals, the component of the k-vector within the crystal

parallel to the surface of incidence is conserved in refraction. The frequency must also be

conserved (i.e., the frequency in air and in the photonic crystal are equal). In particular, the

solutions are evaluated by a geometric analysis,[37] where a construction line perpendicular to

K_{parallel} (dotted line) is overlaid on the EFC. Intersections of this line with the frequency

contour ($\omega|\mathbf{a}|/2\pi c$ = 0.225) constitute solutions for the photonic crystal. An additional

constraint applies to the incident frequencies to prevent higher order

Bragg diffraction: $\omega|\mathbf{a}|/2\pi c \leq 0.353$ (for ΓM incidence). Refraction and reflection modes

[green vectors in Figure 2.7(b)], are found, respectively, when—

$$v_g^{PC, \text{ perpendicular}} \cdot v_g^{\text{incident, perpendicular}} > 0 \qquad\qquad \text{(Equation 2.1)}$$

$$v_g^{PC, \text{ perpendicular}} \cdot v_g^{\text{incident, perpendicular}} < 0 \qquad\qquad \text{(Equation 2.2)}$$

where the perpendicular superscript indicates the component perpendicular to $K_{parallel}$. The refraction and handedness of the solution are determined by the group velocity $v_g = \nabla_k \omega$ and the phase velocity $v_\phi = \omega/k$, respectively. Negative refraction occurs for $v_g^{PC,\ parallel} \cdot v_g^{incident,\ parallel} < 0$. In other words, the incident beam and refracted beam propagate on the same side of the surface normal. The handedness of the propagation is right-handed since, $v_g^{PC} \cdot v_\phi^{PC} > 0$. Therefore, the square bilayer structure supports right-handed negative refraction in the second band.

Dimpled polystyrene (PS) spheres similar to the cut spheres in this study have been synthesized via phase separation removal of the decane phase under heat treatment.[38] Similarly, dimpled spheres have been produced by nucleating polymerizable oil droplets on PS seeds, selectively dissolving PS and crosslinking the oil.[39] PS mushroom cap-shaped particles have also been synthesized by crosslinking PS and using toluene as a swelling solvent. The high solvent release rate results in the anisotropic morphology.[18] Self-assembly of such particles under confinement and double-inverse opal fabrication[40] could be used to manufacture the direct photonic crystal structure. Common dielectrics that could support large complete bandgaps in the square bilayer include SnS_2, Si, GaAs and Ge. Well-established atomic layer deposition and chemical vapor deposition methods could be used to infiltrate the colloidal template.[41]

Conclusion

In summary, this report explores photonic properties of anisometric particles in a square lattice. Unlike the sphere-based square bilayer structure, which has no band gap,[29] a complete band gap was found in the cut-sphere based structure. Large, stable bandgaps (bandgap size = 10.2%) in the direct structure were found as a function of cut-fraction and
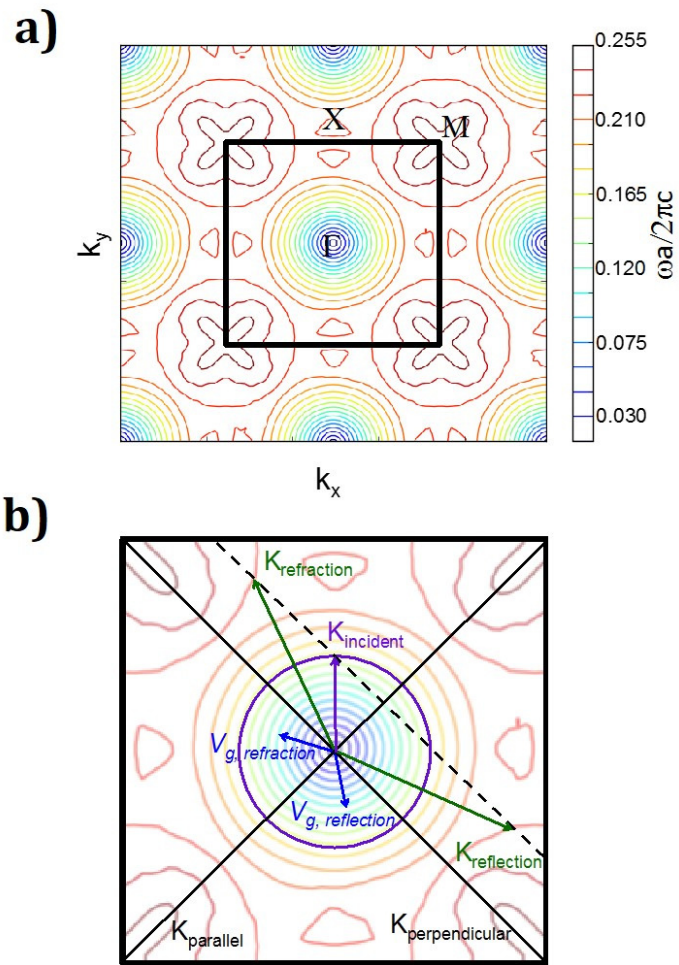
Figure 2.7. (a) Equifrequency contour (EFC) for band 2 of the direct structure with h = 1.0, ε_r = 12 and χ = 0.75. (b) Schematic refraction analysis for Gaussian beam with frequency $\omega|\mathbf{a}|/2\pi c$ = 0.225 and 45° incident angle on the ΓM interface. Right-handed negative refraction (RHNR) is predicted.

slab height. Multiple smaller bandgaps in the inverted structure were also predicted. Vertical cross-section variation combined with a relatively isotropic Brillouin zone is central in promoting the complete gaps. The direct bandgap is of comparable size to structures requiring high precision lithographic design, but can be achieved by colloidal synthesis and self-assembly techniques. The direct bandgap character can be attributed in large part to the Bragg scattering component, dependent on the particle cut fraction. Other photonic properties that would also be interesting to pursue include all angle negative refraction and slow light effects. This work highlights the importance of anisotropic bases in promoting photonic properties.

REFERENCES

[1]   T. F. Krauss, *J. Phys. D. Appl. Phys.* **2007**, *40*, 2666.

[2]   Z.-Y. Li, L.-L. Lin, *Phys. Rev. B* **2003**, *68*, 245110.

[3]   A. Mihi, F. J. López-Alcaraz, H. Míguez, *Appl. Phys. Lett.* **2006**, *88*, 193110.

[4]   D. W. Prather, S. S. S. Shi, J. Murakowski, G. J. Schneider, a. Sharkawy, C. C. C. Chen, B. M. B. Miao, *IEEE J. Sel. Top. Quantum Electron.* **2006**, *12*, 1416.

[5]   C. Reese, B. Gayral, B. Gerardot, A. Kiraz, A. Imamoglu, P. M. Petroff, E. L. Hu, in *Proc. SPIE* (Eds: A. Adibi, A. Scherer, S.-Y. Lin), **2002**, pp. 215–220.

[6]   R. R. N. Simons, *Coplanar Waveguide Circuits, Components, and Systems*, **2001**.

[7]   J. Fischer, G. von Freymann, M. Wegener, *Adv. Mater.* **2010**, *22*, 3578.

[8]   J. F. Galisteo-López, M. Ibisate, R. Sapienza, L. S. Froufe-Pérez, A. Blanco, C. López, *Adv. Mater.* **2011**, *23*, 30.

[9]   P. R. P. Villeneuve, M. Piche, Michel Piche, *Phys. Rev. B* **1992**, *46*, 4969.

[10]   H. Kurt, D. S. Citrin, *Opt. Express* **2005**, *13*, 10316.

[11]   T. Trifonov, L. Marsal, A. Rodríguez, J. Pallarès, R. Alcubilla, *Phys. Rev. B* **2004**, *69*, DOI 10.1103/PhysRevB.69.235112.

[12]   S. G. S. Johnson, S. Fan, P. R. P. Villeneuve, J. Joannopoulos, L. Kolodziejski, *Phys. Rev. B* **1999**, *60*, 5751.

[13]   C. G. Bostan, R. M. de Ridder, *J. Opt. Adv. Mat* **2002**, *4*, 921.

[14]   T. Fathollahi Khalkhali, B. Rezaei, a Soltani Vala, M. Kalafi, *Appl. Opt.* **2013**, *52*, 3745.

[15]   I. D. Hosein, B. S. John, S. H. Lee, F. a. Escobedo, C. M. Liddell, *J. Mater. Chem.* **2009**, *19*, 344.

[16]   K. P. Herlihy, J. Nunes, J. M. Desimone, *Langmuir* **2008**, *24*, 8421.

[17]   E. Y. K. Fung, K. Muangnapoh, C. M. Liddell Watson, *J. Mater. Chem.* **2012**, *22*, 10507.

[18]   S. J. Penterman, A. Singh, W. R. Zipfel, C. M. Liddell Watson, *Adv. Opt. Mater.* **2014**, *2*, 1024.

[19]   C. J. Hernandez, T. G. Mason, *J. Phys. Chem. C* **2007**, *111*, 4477.

[20]   C. I. Zoldesi, C. A. Van Walree, A. Imhof, *Langmuir* **2006**, *22*, 4343.

[21]   S. H. Lee, C. M. Liddell, *Small* **2009**, *5*, 1957.

[22]   L. Malaquin, T. Kraus, H. Schmid, E. Delamarche, H. Wolf, *Langmuir* **2007**, *23*, 11513.

[23]   O. D. Velev, K. H. Bhatt, *Soft Matter* **2006**, *2*, 738.

[24]   M. Golosovsky, Y. Saado, D. Davidov, *Appl. Phys. Lett.* **1999**, *75*, 4168.

[25]   B. Pieranski, Pa., Strzelecki, L., Pansu., *Phys. Rev. Lett.* **1983**, *50*, 900.

[26]   E. K. Riley, C. M. Liddell, *Langmuir* **2010**, *26*, 11648.

[27]   E. K. Riley, C. M. Liddell Watson, *J. Appl. Phys.* **2014**, *115*, DOI 10.1063/1.4880743.

[28]   E. K. Riley, E. Y. Fung, C. M. Watson, *J. Appl. Phys.* **2012**, *111*, 93504.

[29]   C. Avendaño, C. M. Liddell Watson, F. a. Escobedo, *Soft Matter* **2013**, *9*, 9153.

[30]   T. F. Krauss, R. M. D. La Rue, S. Brand, *Nature* **1996**, *383*, 699.

[31]   R.-L. Chern, S. D. Chao, *Opt. Express* **2008**, *16*, 16600.

[32]   M. I. Mishchenko, *J. Quant. Spectrosc. Radiat. Transf.* **2009**, *110*, 808.

[33] C. T. Chan, S. Datta, K. M. Ho, C. M. Soukoulis, *Phys. Rev. B* **1994**, *50*, 1988.

[34] J.-W. Gao, Y. Zhang, N. Ba, C.-L. Cui, J.-H. Wu, *Opt. Lett.* **2010**, *35*, 709.

[35] P. Light, F. Couny, Y. Y. Wang, N. V. Wheeler, P. J. Roberts, F. Benabid, *Opt. Express* **2009**, *17*, 16238.

[36] Y. Huang, W. Lu, S. Sridhar, *Phys. Rev. A* **2007**, *76*, DOI 10.1103/PhysRevA.76.013824.

[37] R. Gajić, R. Meisels, F. Kuchar, K. Hingerl, *Opt. Express* **2005**, *13*, 8596.

[38] T. Tanaka, Y. Komatsu, T. Fujibayashi, H. Minami, M. Okubo, *Langmuir* **2010**, *26*, 3848.

[39] S. Sacanna, M. Korpics, K. Rodriguez, L. Colón-Meléndez, S.-H. Kim, D. J. Pine, G.-R. Yi, *Nat. Commun.* **2013**, *4*, 1688.

[40] T. Ruhl, P. Spahn, C. Hermann, C. Jamois, O. Hess, *Adv. Funct. Mater.* **2006**, *16*, 885.

[41] J. H. Moon, S. Yang, *Chem. Rev.* **2010**, *110*, 547.

CHAPTER 3

PHOTONIC MESOPHASES FROM CUT ROD ROTATORS[*]

Introduction

Photonic crystals (PCs) dramatically alter the dispersion relations and the spatial power distribution of electromagnetic (EM) modes in dielectric materials with a periodic refractive index. Specific designs of photonic crystals promote photonic bandgaps, i.e., frequency ranges over which propagation is disallowed in the material for all directions and polarizations of light. The anomalous dispersion in PCs enables light localization[1] spontaneous emission enhancement or suppression,[2] slow light,[3] and effective negative refraction[4]. Such PC properties have been applied in sensors, waveguides,[1,5] solid state lighting,[6] photovoltaics,[7] nonlinear optics,[8] superlenses,[9] etc. As well, photonic glasses provide control over light diffusion via the optical resonances of building blocks with short range positional order[10,11]. The superposition of multiply scattered light in disordered media with optical gain leads to self-tuned lasing.[12]

Recently, new concepts have emerged as unifying characteristics for predicting structures that may support large photonic band gaps, namely the arrangements should have hyperuniform long-range density fluctuations and uniform nearest neighbor connectivity. Such patterns are distinguished by a structure factor $S(\mathbf{k})$ tending toward zero as $|\mathbf{k}|$ approaches zero and include hyperuniform disordered structures,[13,14] continuous random networks,[15] icosahedral quasicrystals,[16] and Archimedean tilings[4,17]. These and other recent reports[11] suggest that neither periodicity nor quasi-periodicity is mandatory for the formation of photonic bandgaps. In particular, the aforementioned arrangements support highly isotropic

photonic bandgaps, unlike the common Bravais lattices. Isotropic bandgaps are desirable for free-form waveguides (i.e., line defects of arbitrary curvature),[18] flexible cavity designs,[19] and out-coupling across all incident angles from light emitting diodes.[20]

Photonic mesophases (PMs) exhibit ordering with structural characteristics between those of crystals and glasses. PMs hold promise to strongly modify spectral and angular transport of light (i.e., similar to crystals) and also to promote bandgaps with high isotropy (i.e., similar to glasses). Mesophases are thermodynamically stable for anisotropic particles self-assembled in bulk[21] at volume fractions between that of the crystal and the fluid or under physical confinement[22]. The partial order arrangements are stabilized by the optimization of specific types of entropy (translational, rotational, conformational, packing entropy).[23]

In particular, rotator mesophases are characterized by translational order and orientational disorder. Such assemblies have been achieved in 2D or bulk colloidal systems of spherocylinders using evaporation-assisted methods[24] and depletion interactions,[25] respectively. Pentagonal particles have also been assembled into rotators using depletion agents to provide 2D confinement.[26] However, fabricating desired structures with building block separations is difficult and additional techniques are required to prepare non-tangent motifs.[27]

A handful of reports demonstrate device applications using rotator structures fabricated with lithography. For example, waveguides with randomly oriented pentagonal pores in a silicon substrate supported random cavities with high-Q of up to 150,000.[28] Embedded PbSe quantum dots in microcavities with randomly oriented square pores showed enhanced photoluminescence with spectral narrowing to 4 nm.[2] Furthermore, random rotation of square motifs on translationally ordered sites were determined to exhibit negative refraction and flat lens focusing of a point source image.[29]

Here, we study photonic bandgap formation in rotator 'mesophases' of rods with circular segment (cut rod) cross sections. The rods lie on a perfect lattice and the cut faces are oriented randomly. The shape parameter of cut fraction describes the truncation of the rod cross section. Within the overall context of the thesis, this study highlights the bandgap mechanisms that support disordered structures having bandgaps, and demonstrates novel applications including slow light for partial order structures. Such arrangements satisfy the structure factor criteria for bandgap formation [Figure 3.1(a,b)].[30] We explore the effect of cut fraction, dielectric contrast, filling fraction and degree of ordering on photonic band gap size in direct and inverted arrangements. In addition, mode field distributions provide insight on the physical origins of the band gap in partial order structures. Highly isotropic photonic bandgaps are found, i.e., up to 34.5% (gap-to-midgap ratio) for the transverse magnetic polarization (TM) in the direct structure and up to 33.5% for the transverse electric polarization (TE) in the inverted structure. We also demonstrate a slow light waveguide using finite-difference time domain (FDTD) methods. Slow-down factors up to 5×10^4 are predicted for waveguides in the $\Gamma - X$ direction.

Methods

The photonic band structure was simulated using the MIT Photonic Bands (MPB) software package. Figure 3.1(c,d) illustrates the model of the cut rods rotator structure and its hexagonal Brillouin zone. The cut rods were centered on the hexagonal lattice points, with unit lattice vectors, $\boldsymbol{a_1} = (\sqrt{3}/2, 1/2, 0)$ and $\boldsymbol{a_2} = (\sqrt{3}/2, -1/2, 0)$. The basis shape parameter is the cut fraction χ and satisfies the condition, $\chi > \vec{\boldsymbol{n}} \cdot (\vec{\boldsymbol{p}} - \vec{\boldsymbol{c}}) + 0.5$, where $|\vec{\boldsymbol{n}}|$ is a unit vector normal to the cut plane, $|\vec{\boldsymbol{p}}|$ is an arbitrary point in the computational grid and $|\vec{\boldsymbol{c}}|$ vector to the center of the circle circumscribing the cut rod. The magnitude of $\vec{\boldsymbol{n}}$ is equal to the lattice constant. Random rotations of the cut faces were generated using a Monte Carlo simulation of freely rotating cut spheres with $\chi = 0.75$, confined by parallel walls of spacing
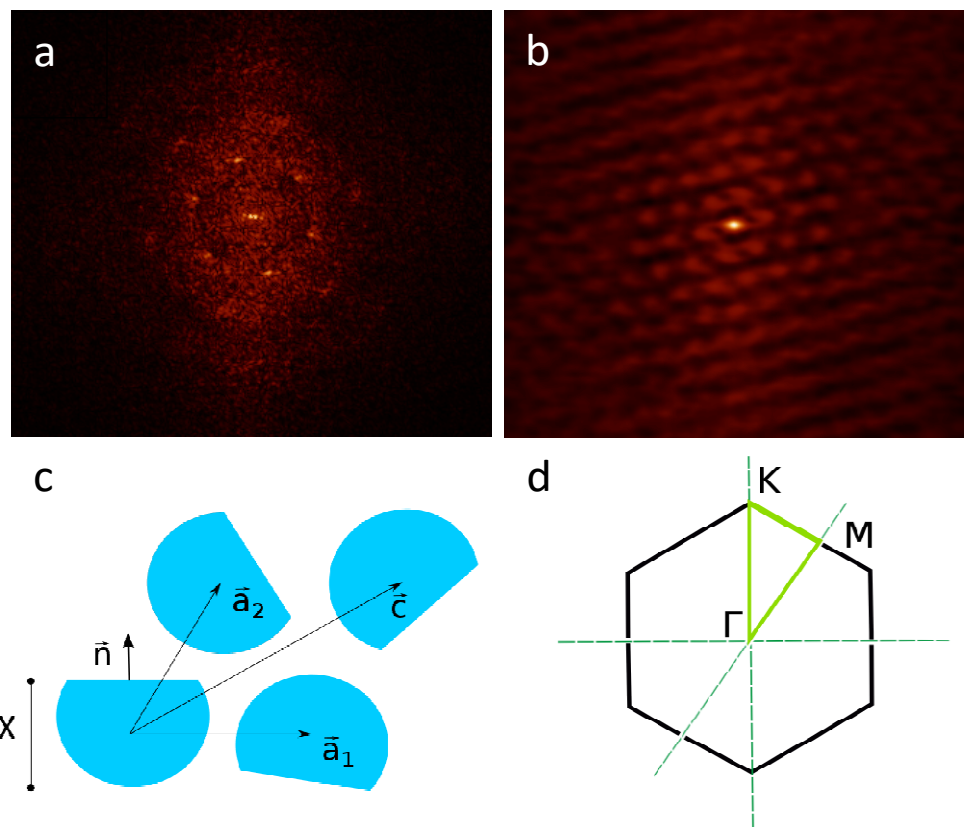
Figure 3.1. a) Fast Fourier Transform (FFT) and **b)** 2D positional correlation function for rotator colloidal mesophase from collapsed spheres.[20] The structure factor criteria appears to be fulfilled for the colloidal arrangement and this motivates the present study. **c)** Schematic of 2D cut rod rotator structure ($\chi = 0.75$) with view along <001> direction. **d)** Brillouin zone of hexagonal lattice, with high symmetry points Γ, M and K marked in the irreducible Brillouin zone.

$P^* = 50 = PV_P/k_BT$, where V_p is the volume of the particle, P is the absolute 1.025σ where

σ is the diameter of the cut sphere particle. The vector $|\vec{n}|$ was defined as the projection onto

the x-y plane of the face orientation vectors generated at normalized pressure, pressure, T is

the temperature and k_B is the Boltzmann constant. For studies on degree of ordering, particle

orientations were defined by a random number generator, i.e., angles in the range from 0 to

n2π were selected, where n is the fractional degree of disorder. The solid volume filling

fractions η were varied via cut fraction and radius R of the rod, from $\chi = 0.5$ to

0.8 and R = 0.3 to 0.5. The rods are tangent at an R value of 0.5 and the cut rod cross-section

is a semicircle at a χ value of 0.5. The filling fraction for the direct and inverted structures as a

function of R and χ was calculated from the expression (see Figure 3.S2 for values):

$$\eta = (2/\sqrt{3})R^2[\cos^{-1}(1 - 2\chi) + (4\chi - 2)\sqrt{\chi - \chi^2}]. \qquad \text{(Equation 3.1)}$$

A supercell of the cut rods was used for calculating the band diagram due to lack of

orientational order. Supercells were spaced by 0.1|a| to ensure that basis particles at the cell

edges were not artificially truncated. Bandgap size was found to vary by less than 1% as a

function of spacing parameter within the range 0 to 0.2|a|. Reducing the basis symmetry from

a rod to a randomly oriented cut rod changes the plane group symmetry from p6mm to p1. The

predicted band properties for the infinite structure were checked by increasing the number of

unit cells and confirming convergence of the bandgap size (Figure 3.S1). Due to the band

folding in supercell calculations, the number of bands was between N+5 and N+26, where N

is the number of unit cells contained in the supercell.

The guided modes were evaluated for structures for direct and inverted structures (i.e.,

air cut rods in dielectric matrix) at dielectric contrasts (ε_r) from 1.5 to 14. A path along the

high symmetry points of the two-dimensional irreducible Brillouin zone of the unit cell

[Figure 3.1(d)] was used to calculate the dispersion curves of light frequency versus wavevector. The first fifty (for 5x5 supercell) solutions were determined by interpolating 25 points between the high symmetry points. The band structures were obtained for transverse electric (TE) and transverse magnetic (TM) modes within a 10^{-8} convergence tolerance. A resolution parameter of 32 and a mesh size of 5 yielded 26,896 plane waves for the typical case and 175,729 plane waves for the convergence analysis. For slow light calculations, a supercell area of 71 unit cells was used, with a line defect of length 5|$\mathbf{a}$| in the $\Gamma-X$ direction. Waveguide propagation and transmission spectra were calculated using MIT Electromagnetic Equation Program (MEEP). For the FDTD simulations, the time step resolution is $\Delta t = S \, \Delta x$,, where S is the Courant factor of 0.5 and Δx is the spatial resolution of 32. 500 normalized frequency values were interpolated between ω|a|/$2\pi c$ = 0.15 to 0.35 for the transmission calculations. A perfectly matched layer of thickness |$\mathbf{a}$| surrounded the waveguide supercell. Transmission was calculated for a Gaussian pulse,[31] where the pulse was allowed to decay to 0.1% of its original value.

Results and Discussion

Figure 3.2 maps the TE and TM bandgap sizes as a function of cut fraction, dielectric contrast and rod radius. The direct structure has large TM bandgaps over a wide range of shape parameters and dielectric contrasts up to 34.5% for the greatest basis spacing (i.e., low R). For the inverted structure, the large TE bandgaps are supported up to 33.5% only for high cut fraction of the air pores at moderate to high ε_c and intermediate basis spacing. The TE bandgaps closed at pore tangency because of lack of interconnectivity for the high refractive index material. The veins of high dielectric should be unbroken so that the continuous TE field lines can be contained within them. At high spacing, the filling fraction becomes too high (70-80%) to support the gap. Moreover, the TM bandgaps closed at rod tangency because the
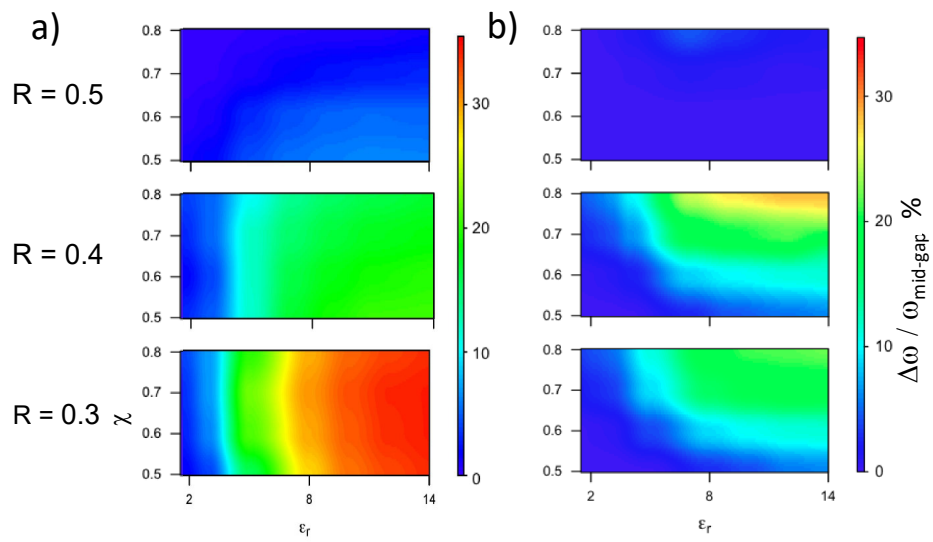
Figure 3.2. Contour map of the gap size for **a)** direct structure and **b)** inverted structure with ε mapped from 2 to 14, χ from 0.5 to 0.8 and R from 0.3 to 0.5.

scalar displacement field favors localization in isolated rods. The TM gap sizes are largest at very low filling fractions (20-30%), which are consistent with the greatest basis spacing. A low filling fraction is favorable to maintain comparable optical path lengths in air and dielectric.[32] The effects of varying the cut fraction of the basis are low in the TM case, and correspond to a maximal 12% change in filling fraction for the direct structure with R=0.3. Notably, the minimum dielectric contrasts to open TE and TM gaps are very low, i.e., ε_r = 2.25 (2.65% at R = 0.4, χ = 0.8) and ε_r = 2.00 (3.69% at R = 0.3, χ = 0.8), respectively. These

low dielectric constant values should allow photonic solids made from common polymers (i.e., polystyrene, polymethylmethacrylate) and ceramics (i.e., alumina, silica, calcite, magnesium fluoride). To date, only quasicrystals have comparable minimum dielectric contrast values (for TM gaps) of ε_r = 2.4 for 5- fold and 8-fold structures.[33] Structural optimization reduced the minimum dielectric contrast value to ε_r = 1.5 (2% gap size for 5-fold). [33]

Figure 3.3 shows the TM (TE) band diagrams for a supercell (i.e., 169 unit cells) of the cut rod (inverted cut rod) structures. Band diagrams for both the TE and TM structure maintained highly isotropic bands bounding the gap, with 1.6% (TM) and 1.1% (TE) change in frequency across the irreducible Brillouin zone. High densities of isotropic bands bound both bandgaps. Such bands may provide low group velocity and high DOS for amplifying non-linear effects, self-tuned lasing, increasing the efficiency of photocatalysis and light-harvesting in solar cells.[3] Bandgap properties are maintained with increasing supercell unit size [Figure 3.S2], confirming that the bandgap is not an artifact of the supercell approximation. The mid-gap frequency of both TE and TM bandgaps remains constant as the supercell size increased. Because the bandgap occurs between the N and N+1 bands, the density of bands increases in the frequencies surrounding the bandgap with increasing
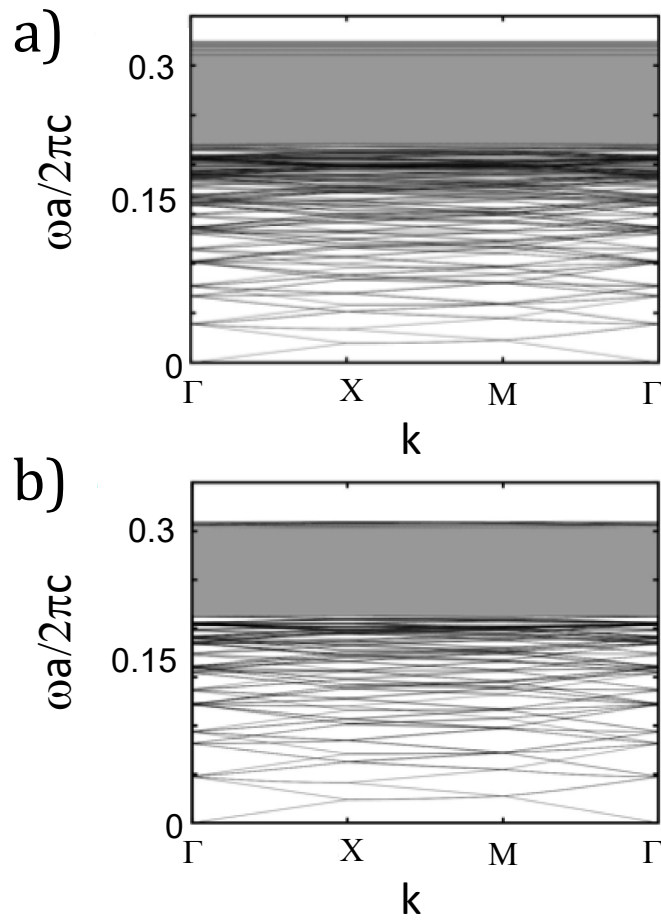
Figure 3.3. a) TE polarization band diagram for inverted structure with $\chi = 0.8$ cut rods with $R = 0.4$, $\varepsilon_r = 14$ and 100% disorder. The TE bandgap has size $\Delta\omega/\omega_{mid\text{-}gap} = 33.5\%$. **b)** TM polarization band diagram for $\chi = 0.7$ cut rods with $R = 0.3$, $\varepsilon_r = 14$ and 100% disorder for TM polarization. The TM bandgap has size $\Delta\omega/\omega_{mid\text{-}gap} = 34.5\%$. Both bandgaps lie between the N and N+1 bands, where N is the number of unit cells within the computational supercell.
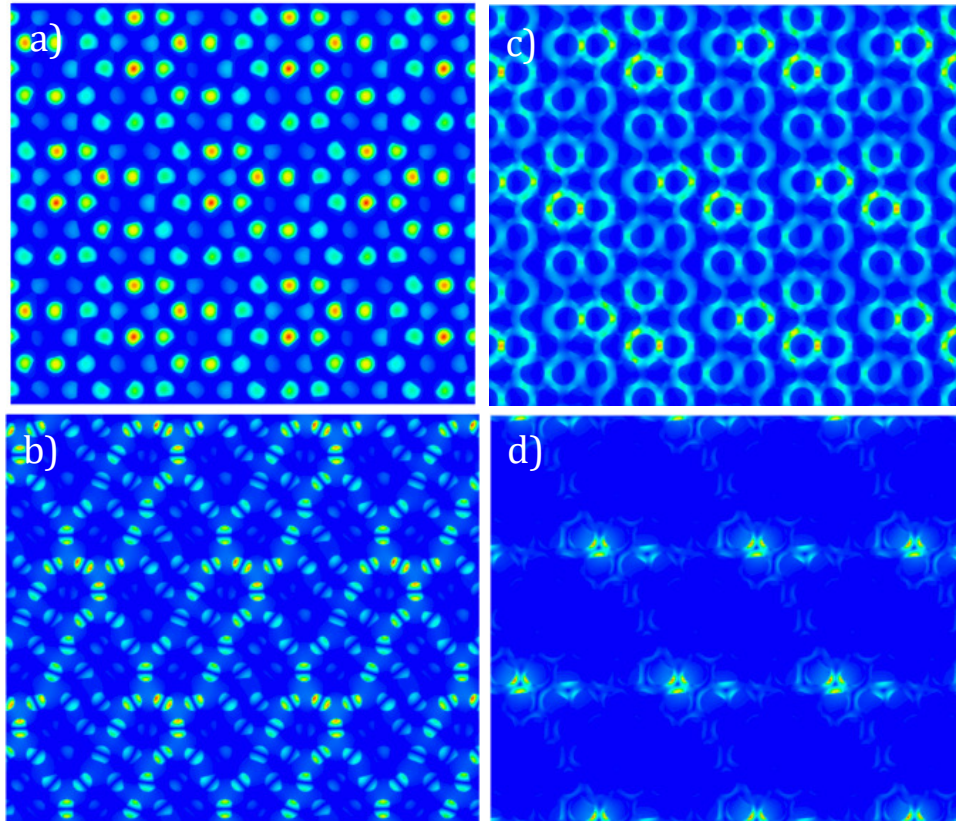
Figure 3.4. a, b) electric displacement field density distribution for the TM polarization in the optimal direct structure (R = 0.3, χ = 0.7, ε_r = 14, 100% disorder). a) lower photonic bandgap edge, b) upper photonic bandgap edge. **c, d)** electric displacement field density distribution for TE polarization in the optimal inverted structure (R = 0.4, χ = 0.8, ε_r = 14, 100% disorder). c) lower photonic bandgap edge, d) upper photonic bandgap edge.

supercell size. The expression ωa/2πc still determines the gap location. No TE band gap was found for the cut rod case and no TM band gap was found for the inverted cut rod case. None of the above properties require a polarization independent badgap,[34] but ideally the slowdown factor would increase, further enhancing the desired properties.

The electric displacement field (i.e., dielectric contrast multiplied by the electric field) was examined at the M high symmetry point for the bands bounding the TE and TM bandgaps, as shown in Figure 3.4. For the TE polarization [Figures 3.4(c, d)], the field is concentrated in the dielectric matrix surrounding the air holes. The upper band exhibits a high degree of localization (i.e., band edge localization) in a complementary region of the high dielectric. Unlike the more common 'air band'-'dielectric band' gaps[13], here the bandgap arises from re-distribution of the mode within the high dielectric.[35] The TM bandgaps form due to consecutive 'Lorenz-Mie' resonances in the dielectric cut rods. Specifically, Figure 3.4(a) shows the inphase oscillations and Figure 3.4(b) shows the antiphase oscillations.

We also examined how the electric displacement fields varied with cut fraction for the bands bounding the TM bandgap since the gap sizes were insensitive to the cut fraction (Figure 3.2). The field density at the M high symmetry point is displayed for direct structures with the largest bandgap in Figure 3.5. The displacement field for the lower gap limiting bands shows first Lorenz-Mie resonances in hexagonal ring-like patterns. Particles at the center of the ring exhibit lower energy density. For $\chi = 0.5$, the energy density was concentrated in a smaller percentage of the particles, while the higher cut fraction arrangements supported a more uniform field distribution. All structures displayed second Lorenz-Mie-type resonances for the higher gap limiting bands. However, the nodal planes show alignment for the most isotropic particle shape with $\chi = 0.8$, similar to the crystal. The findings suggest that because these TM bandgaps are based on the same Lorenz-Mie resonances (at constant frequencies),
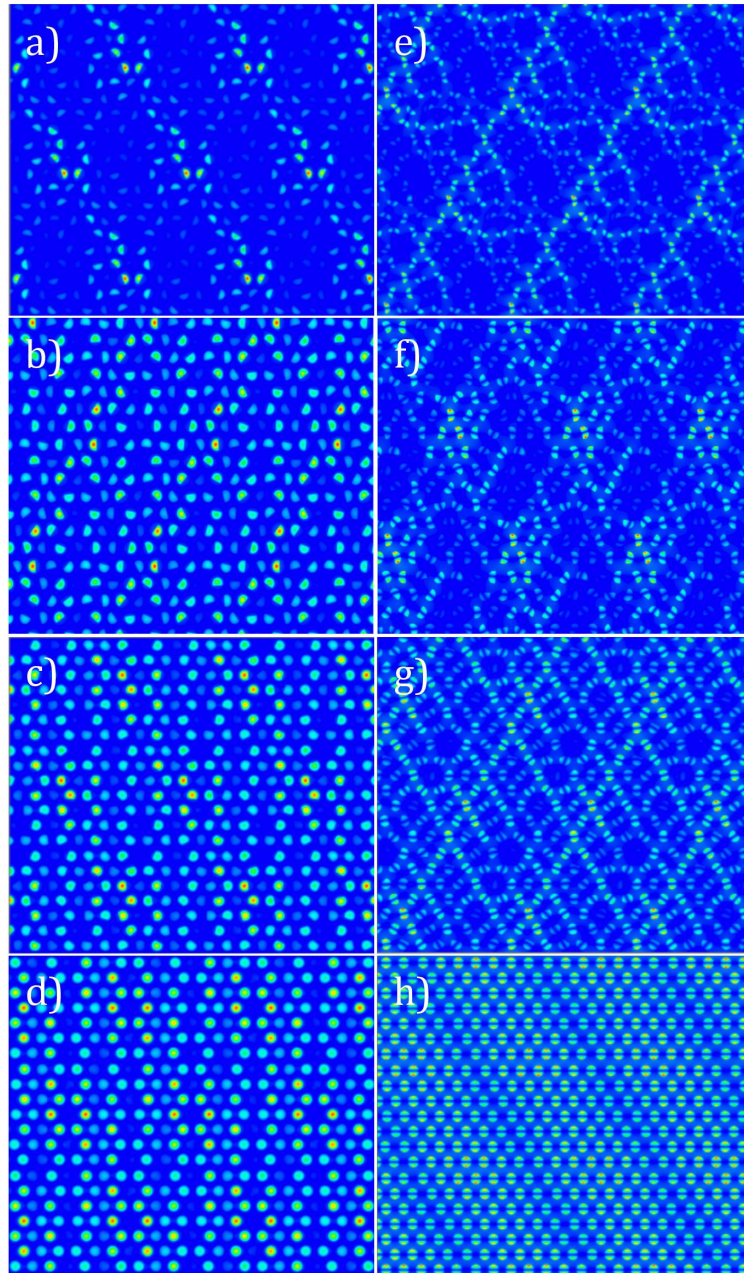
Figure 3.5. Electric displacement field density distribution for TM polarization in the direct structure for different χ values of lower photonic bandgap edge (a, b, c, d) and upper photonic bandgap edge (e, f, g, h). Structural parameters are R = 0.3, ε_r = 14, 100% disorder, with χ = 0.5 (a, e), χ = 0.6 (b, f), χ = 0.7 (c, g) and χ = 0.8 (d, h).

the gap size is largely independent of the rod shape.[36] In comparison to the hexagonal crystal

of cylindrical rods (gap size 27.8% at R = 0.3, ε_r = 14), the cut rod rotator has a larger TM

bandgap for the same radius value. In contrast, the inverse hexagonal crystal supports a much

larger TE bandgap (gap size 51.9% at R = 0.4, ε_r = 14) than the rotator arrangement. The latter

finding is analogous to the trends found for quasicrystals compared to photonic crystals;

namely, that crystals provide a larger bandgap at high dielectric contrasts, while quasicrystals

allow a much lower minimum refractive index contrast for opening a bandgap.[11] With regard

to fabrication, the cut rod rotator could be made using electron beam lithography and physical

(chemical) vapor deposition of Si (GaAs). Fabrication via photolithography is also possible

with photoresist as the higher index material versus air.[28,37,38]

Previous studies on disorder in photonic crystals have found it to be detrimental to

band gap stability. For instance, geometrical non-uniformity in inverse opal photonic crystals

such as variations in the radii of spheres or random displacements from lattice sites greatly

reduced the 8-9 bandgap. In fact, disorder as small as two percent of the lattice constant

completely closed the bandgap.[39] A photonic crystal lens with inverse hexagonal 2D pattern

yielded deteriorated images due to misorientation disorder values of 10%.[40] However, for the

Lorenz-Mie resonance-type band gap the gap size could be independent of the orientational

disorder of the scatterers since the resonances promote an attractive potential for photons in

isolated dielectric scatterers.[41]

We examined the bandgap size variations with degree of disorder ranging from 0-

100% for direct and inverted structures with the maximum bandgap size. The bandgap sizes

for the direct TM arrangement vary by 1.3% over the range of disorder (Figure 3.6). The

variation in gap size with disorder for the TE case was as large as 4.5% and no trend was
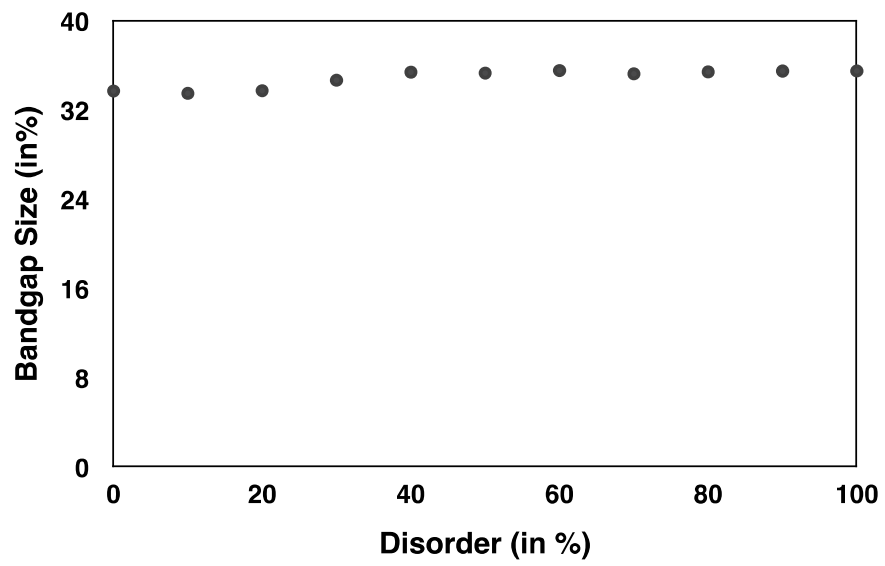
Figure 3.6. Bandgap size ($\Delta\omega/\omega_{\text{mid-gap}}$) dependence on disorder for the direct TM bandgap with structural parameters R = 0.3, ε_r = 14, and χ = 0.7.

apparent, as expected. Additionally, we mapped the TM bandgap sizes as a function of cut fraction, dielectric contrast and rod radius for an arrangement with 20% disorder (Figure 3.S3). The map generally shows a higher minimum dielectric contrast than the one for the completely disordered case, otherwise the maps are similar.

The electric displacement field densities for bands bounding the bandgaps were examined to explore why the TM bandgap is insensitive to orientational disorder (Figure 3.7). The first and second Lorenz-Mie resonances occurred below and above the bandgap, respectively. The first Lorenz-Mie resonances had similar field density distributions. The nodal planes became increasingly aligned as the disorder is decreased to 20%, resulting in a displacement field similar to that of the crystalline rod case. The frequencies of the Lorenz-Mie resonances were also not substantially affected by disorder in the structure, which accounts for the comparable bandgap sizes.

To investigate the dependence of bandgap size on cut-rod conformation at constant disorder, nine simulations at 100% disorder were performed for randomly generated inverted conformations. The bandgap size varied by 8.3%. This sensitivity to conformation is due to the inverted bandgap partially depending on Bragg scattering.

In addition, the slow light properties were investigated for a line defect waveguide in the rotator structure (R = 0.3, χ = 0.7, ε_r = 14) for TM polarized light. The band diagram of the waveguide in Figure 3.8(a) displays a highly isotropic defect mode at $\omega|a|/2\pi c$ = 0.285 (0.6% change across k-space). This corresponds to a peak in the transmission spectra of the waveguide calculated using FDTD methods [Figure 3.9(b)]. The slowdown factor $S = v_\phi / v_g$ is plotted in Figure 3.9(a) for the defect mode between high symmetry points Γ and X. For dispersion in a photonic crystal, $v_g = \nabla k$ and $v_\phi = \omega/|k|$. S is maximized at the
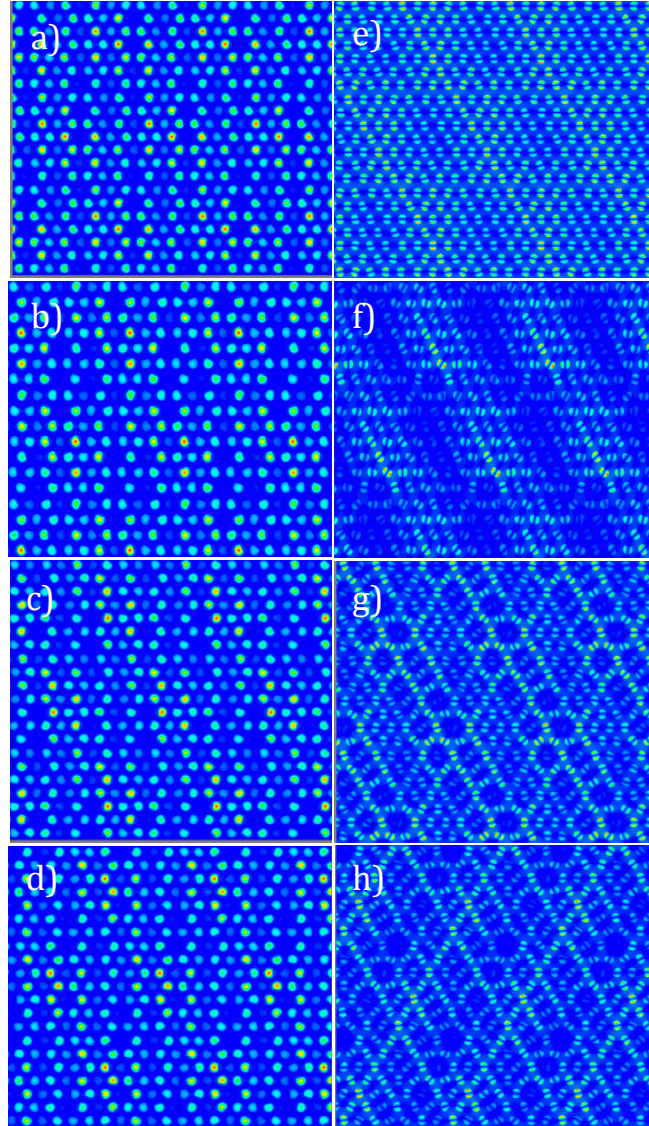
Figure 3.7. Electric displacement field density distribution of lower photonic bandgap edge (a, b, c, d) and upper photonic bandgap edge (e, f, g, h) for TM polarization in the direct structure for varied disorder. Structural parameters are R = 0.3, ε_r = 14, and χ = 0.7 with 20% disorder (a, e), 40% disorder (b, f), 80% disorder (c, g) and 100% disorder (d, h).
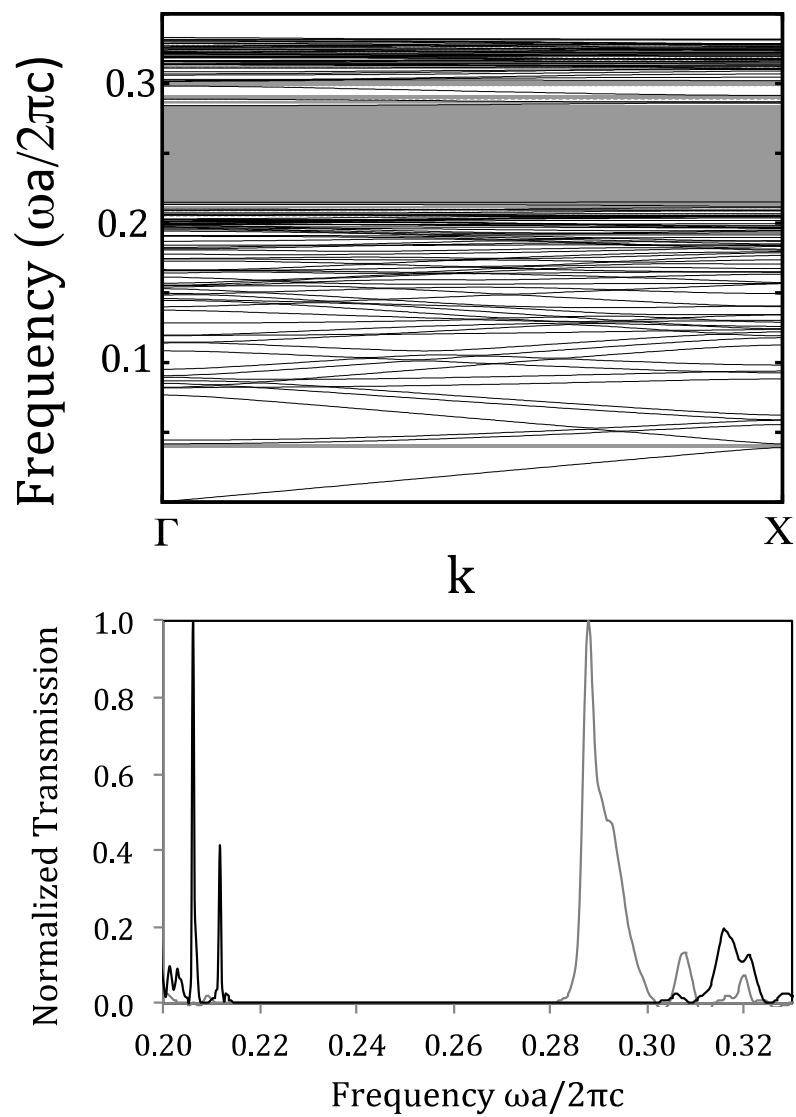
Figure 3.8. a) Band diagram of rotator supercell waveguide in the ΓX direction. Defect modes occur in gap at ω|a|/2πc =0.285. b) Normalized transmission spectrum for rotator structure (black line) and waveguide supercell (gray line). Transmission peak in waveguide occurs at ω|a|/2πc =0.285.
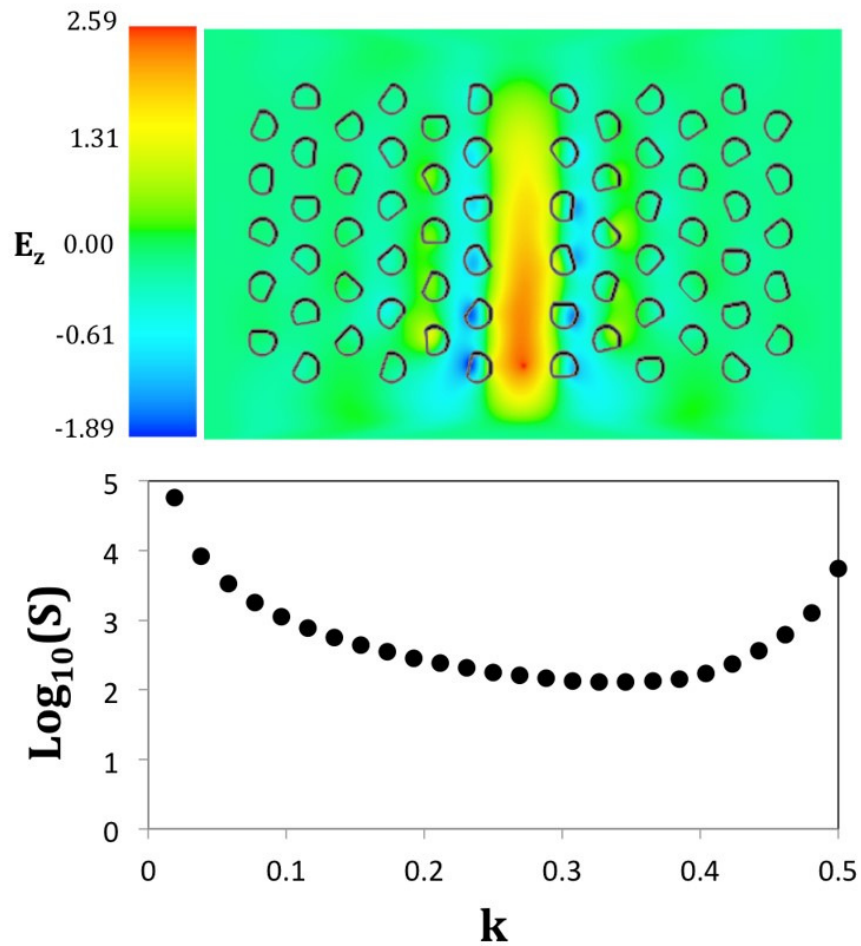
Figure 3.9. a) FDTD of point source propagation through rotator mesophase waveguide. Point source has amplitude 1.0, and the snapshot is taken after 300 time steps. b) Slowdown factor over k-space along the Γ−X direction. S is maximized at high symmetry points with values up to 5 x 10⁴ and has minimum values of above 10² for intermediate k-values.

high symmetry points of the Brillouin zone for k = 0 and k = 0.5, and reaches 5 x 10^4. S

maintains minimum values of 10^2-10^3 across the k-vector range. Slowdown factors in photonic

crystal systems have been reported with values approaching 10^3, but typical values are in the

range of 10^2.[42,43]

Slow light is confirmed with FDTD simulations, where a point source with frequency

ω|a|/2πc = 0.285 is placed at the start of the waveguide and allowed to propagate. An

enhancement of 250% in electric field intensity above the initial amplitude is found. Thdis

demonstrates the compression of the signal within the waveguide. As is typical of waveguides

with high S values, the point source signal samples into the structure up to three unit cells.[42]

Lorenz-Mie resonance-induced localization within the cut spheres is also observed along the

waveguide, similar to the defect-free material in Figure 3.4.

Conclusion

In summary, we find highly isotropic photonic bandgaps that open at low dielectric

contrasts for both polarizations in cut rod-based rotators. In this system, order and disorder

cohabit so that both Lorenz-Mie resonances from the randomly oriented cut rods and Bragg

scattering from the periodic lattice are the source of the bandgaps, dependent on the geometry

of the high dielectric. The TM bandgap insensitivity to the degree of disorder and cut-rod

shape is rationalized from the Lorenz-Mie resonances occurring at constant frequency. The TE

bandgap varied with conformation because the gap arises from redistribution of mode field

within the high dielectric and has a strong Bragg scattering component. A rotator waveguide

was predicted with a remarkably high slowdown factor. This demonstrates the promise of

slow light in the highly isotropic defect states of photonic mesophases. Related mesophases

satisfy the structure factor criteria and thus hold promise as self-assembled photonic solids.

Our work opens a frontier for research to manipulate mesophase partial order effects for

photonics.
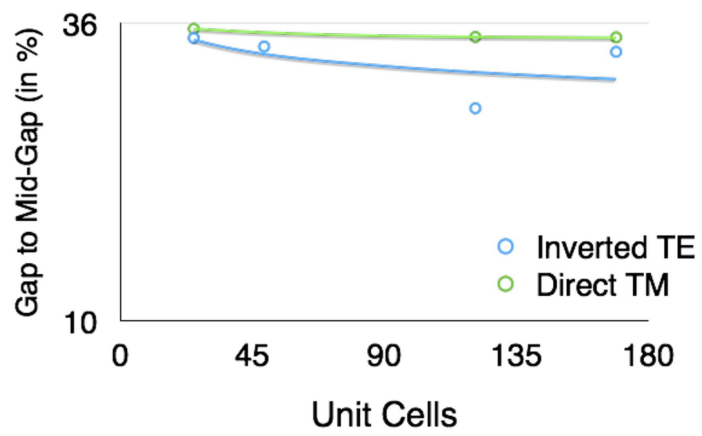
Figure 3.S1. Photonic band gap maximum sizes for direct rotator structures (green) and inverted rotator structures (blue).
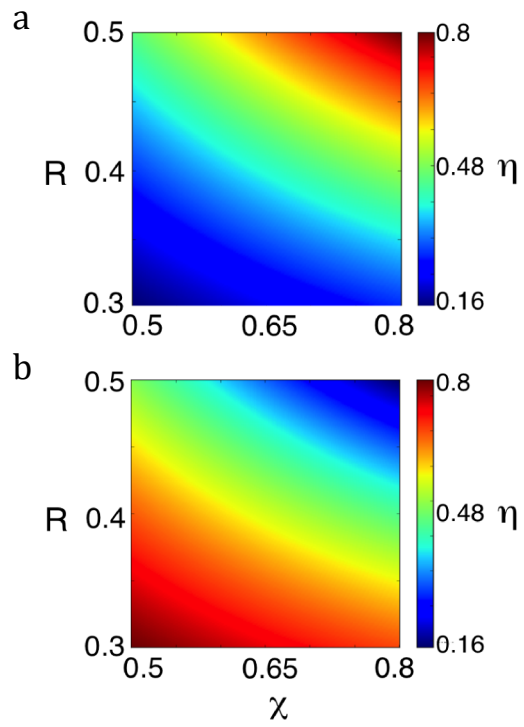
Figure 3.S2. Dielectric filling fraction η for **a)** direct structure and **b)** inverted structure as a function of cut fraction χ and separation parameter R. The mapping ranges are from χ of 0.5 to 0.8 and from R of 0.3 to 0.5.
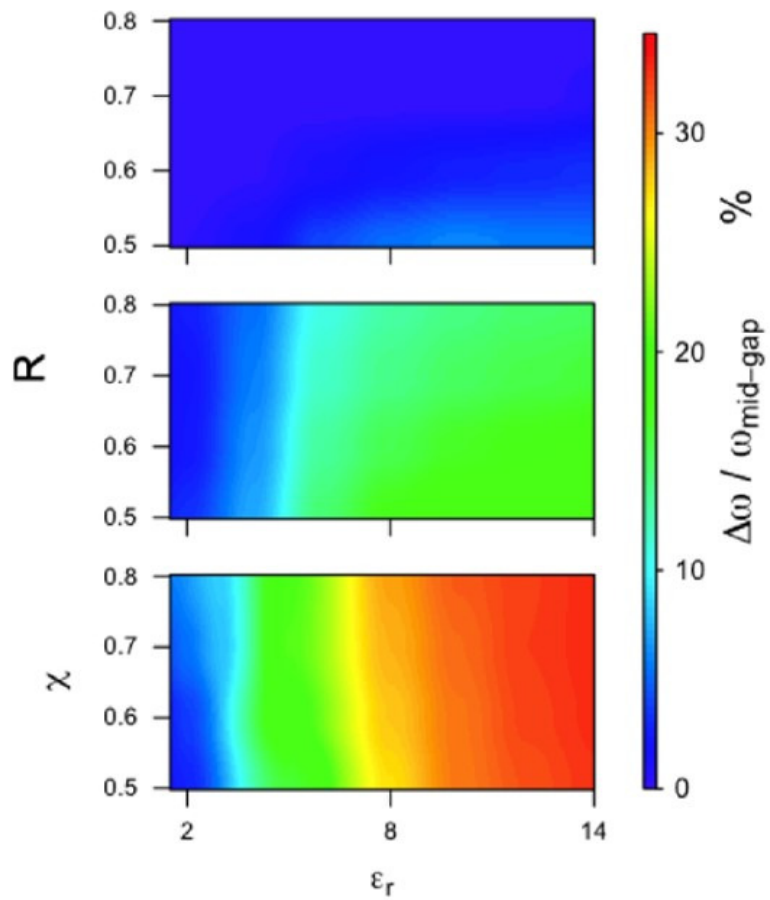
Figure 3.S3. Contour map of the gap size for direct structure with 20% disorder with ε mapped from 2 to 14, χ from 0.5 to 0.8 and R from 0.3 to 0.5.

REFERENCES

[1]   J. D. Joannopoulos, P. R. Villeneuve, S. Fan, *Nature* **1997**, *386*, 143.

[2]   J. Yang, J. Heo, T. Zhu, J. Xu, J. Topolancik, F. Vollmer, R. Ilic, P. Bhattacharya, *Appl. Phys. Lett.* **2008**, *92*, 261110.

[3]   T. Baba, *Nat. Photonics* **2008**, *2*, 465.

[4]   D. Jovanović, R. Gajić, K. Hingerl, *Opt. Express* **2008**, *16*, 4048.

[5]   S. G. S. Johnson, S. Fan, P. R. P. Villeneuve, J. Joannopoulos, L. Kolodziejski, *Phys. Rev. B* **1999**, *60*, 5751.

[6]   M. Boroditsky, T. F. Krauss, R. Coccioli, R. Vrijen, R. Bhat, E. Yablonovitch, *Appl. Phys. Lett.* **1999**, *75*, 1036.

[7]   H. L. Chen, S. Y. Chuang, C. H. Lin, Y. H. Lin, *Opt. Express* **2007**, *15*, 14793.

[8]   E. Centeno, C. Ciraci, D. Felbacq, D. Cassagne, *Proc. SPIE* **2008**, *6989*, 698915.

[9]   R. Meisels, R. Gajic, F. Kuchar, K. Hingerl, *Opt. Express* **2006**, *14*, 6766.

[10]   J. F. Galisteo-López, M. Ibisate, R. Sapienza, L. S. Froufe-Pérez, A. Blanco, C. López, *Adv. Mater.* **2011**, *23*, 30.

[11]   K. Edagawa, *Sci. Technol. Adv. Mater.* **2014**, *15*, 34805.

[12]   P. D. García, R. Sapienza, C. López, *Adv. Mater.* **2010**, *22*, 12.

[13]   M. Florescu, S. Torquato, P. J. Steinhardt, *Proc. Natl. Acad. Sci. U. S. A.* **2009**, *106*, 20658.

[14]   W. Man, M. Florescu, K. Matsuyama, P. Yadak, S. Torquato, P. Steinhardt, **2010**, 1.

[15]   K. Edagawa, S. Kanoko, M. Notomi, *Phys. Rev. Lett.* **2008**, *100*, 13901.

[16]   W. Man, M. Megens, P. J. Steinhardt, P. M. Chaikin, *Nature* **2005**, *436*, 993.

[17]   S. David, a. Chelnokov, J.-M. Lourtioz, *Opt. Lett.* **2000**, *25*, 1001.

[18]   W. Man, M. Florescu, E. P. Williamson, Y. He, S. R. Hashemizad, B. Y. C. Leung, D.

R. Liner, S. Torquato, P. M. Chaikin, P. J. Steinhardt, *Proc. Natl. Acad. Sci. U. S. A.* **2013**, *110*, 15886.

[19]   S. Tsitrin, Y. He, S. Hewatt, B. Leung, W. Man, M. Florescu, P. J. Steinhardt, S. Torquato, P. Chaikin, *Front. Opt. 2012/Laser Sci. XXVIII* **2012**, FTh3F.4.

[20]   A. A. David, T. Fujii, E. Matioli, R. Sharma, S. Nakamura, S. P. Denbaars, C. Weisbuch, H. Benisty, *Appl. Phys. Lett.* **2006**, *88*, 10.

[21]   F. a Escobedo, *Soft Matter* **2014**, *10*, 8388.

[22]   C. Avendaño, C. M. Liddell Watson, F. a. Escobedo, *Soft Matter* **2013**, *9*, 9153.

[23]   K. Muangnapoh, C. Avendaño, F. a. Escobedo, C. M. Liddell Watson, *Soft Matter* **2014**, *10*, 9729.

[24]   I. D. Hosein, B. S. John, S. H. Lee, F. a. Escobedo, C. M. Liddell, *J. Mater. Chem.* **2009**, *19*, 344.

[25]   E. B. Mock, C. F. Zukoski, *Langmuir* **2007**, *23*, 8760.

[26]   K. Zhao, T. Mason, *Phys. Rev. Lett.* **2009**, *103*, DOI 10.1103/PhysRevLett.103.208302.

[27]   B. Liu, T. H. Besseling, M. Hermes, A. F. Demirörs, A. Imhof, A. van Blaaderen, *Nat. Commun.* **2014**, *5*, 3092.

[28]   J. Topolancik, F. Vollmer, B. Ilic, *Appl. Phys. Lett.* **2007**, *91*, 201102.

[29]   Z. Feng, X. Zhang, S. Feng, K. Ren, Z.-Y. Li, B. Cheng, D. Zhang, *J. Opt. A Pure Appl. Opt.* **2007**, *9*, 101.

[30]   E. Y. K. Fung, K. Muangnapoh, C. M. Liddell Watson, *J. Mater. Chem.* **2012**, *22*, 10507.

[31]   S. Fan, J. D. Joannopoulos, J. N. Winn, A. Devenyi, J. C. Chen, R. D. Meade, *J. Opt. Soc. Am. B* **1995**, *12*, 1267.

[32]   T. F. Krauss, R. M. De La Rue, *Prog. Quantum Electron.* **1999**, *23*, 51.

[33] M. Rechtsman, H.-C. Jeong, P. Chaikin, S. Torquato, P. Steinhardt, *Phys. Rev. Lett.* **2008**, *101*, DOI 10.1103/PhysRevLett.101.073902.

[34] H. Chen, S. Chen, X. Quan, Y. Zhang, *Environ. Sci. Technol.* **2010**, *44*, 451.

[35] R.-L. Chern, S. D. Chao, *Opt. Express* **2008**, *16*, 16600.

[36] M. I. Mishchenko, A. Lacis, *Appl. Opt.* **2003**, *42*, 5551.

[37] M. De Vittorio, M. T. Todaro, T. Stomeo, R. Cingolani, D. Cojoc, E. Di Fabrizio, *Microelectron. Eng.* **2004**, *73–74*, 388.

[38] Z.-Y. Li, Z.-Q. Zhang, *Adv. Mater.* **2001**, *13*, 433.

[39] C. C. Cheng, A. Scherer, *J. Vac. Sci. Technol. B Microelectron. Nanom. Struct.* **1995**, *13*, 2696.

[40] X. Wang, K. Kempa, *arXiv Prepr. cond-mat/0409780* **2004**.

[41] C. Luo, S. Johnson, J. Joannopoulos, J. Pendry, *Phys. Rev. B* **2002**, *65*, DOI 10.1103/PhysRevB.65.201104.

[42] T. F. Krauss, *J. Phys. D. Appl. Phys.* **2007**, *40*, 2666.

[43] J. P. Hugonin, P. Lalanne, T. P. White, T. F. Krauss, *Opt. Lett.* **2007**, *32*, 2638.

PHOTONIC CRYSTAL PROPERTIES OF SELF-ASSEMBLED ARCHIMEDEAN TILINGS

Introduction

Photonic crystals (PCs) are dielectric materials with a periodic refractive index that dramatically affects the dispersion relation and spatial power distribution of electromagnetic modes.[1] The light localization, spontaneous emission suppression, slow light (i.e., extreme low group velocity) and anomalous refraction phenomena in PCs have been applied in sensors, waveguides, solid state lighting, photovoltaics, nonlinear optics, and superlenses.[1–4] A variety of parameters including orientational ordering, symmetry, motif shape, dielectric connectivity, dielectric constants, and filling fraction determine the optical properties of a photonic material.[5,6] Recently, a unifying framework has emerged that predicts sizable bandgaps for structures that have a static structure factor that approaches zero as the wavenumber $k \rightarrow 0$.[7] Such structures include hyperuniform disordered networks, continuous random networks, icosahedral quasicrystals, and Archimedean tilings.[7–10]

Shape-binary mixtures of regular polygons may form Archimedean tilings which promote large isotropic photonic bandgaps due to their high rotational symmetry. The tilings are denoted by symbols (e.g., $3^2.4.3.4$) that represent the cyclic order of squares (4) and equilateral triangles (3) surrounding the vertices, with the degeneracy of the identical polygons indicated by the superscript. The $3^2.4.3.4$ tiling of high dielectric rods at vertices of the polygons has near 12-fold local rotational symmetry and band gap variation of only 1-3% over all incident angles. The structure was found to show left-handedness (i.e., product of group and phase velocity less than zero) and negative refraction for both linear polarizations.[11]

Bandgap isotropy is desirable for applications including free-form waveguides (i.e., line defects of arbitrary curvature), flexible cavity designs, and light emitting diodes (LEDs).[12,13] In the latter case, Archimedean PCs have been utilized to produce compact, omnidirectional light extraction.[14,15] Reports on the photonic properties of Archimedean lattices have focused primarily on structures made from isolated rods consistent with a lithographic fabrication process at the microscale.

Nanoscale materials such as binary mixtures of Fe_3O_4 and Au nanoparticles, [16] micellar phases of dendritic polymers,[17] and ABC star-branched terpolymers[18] have been shown to self-organize into Archimedean tilings. The latter supramolecular materials were predicted to have TM (transverse magnetic) bandgaps (gap-to-midgap ratio $\Delta\omega/\omega_{mid-gap}$ up to 6.6%) and TE (transverse electric) bandgaps ($\Delta\omega/\omega_{mid-gap}$ up to 9.3%) for the $3^2.4.3.4$ and $4.6.12$ structures, respectively.[19] However, the bandgaps in this system are much smaller than the bandgaps for lithographically patterned Archimedean lattices made of circular rods in air ($\Delta\omega/\omega_{mid-gap}$ up to 45%).[11]

Here, we investigate the photonic properties of Archimedean tilings made from triangular and square cross-section rods, inspired by self-assembly of binary colloidal mixtures. Such structures have recently been predicted in Monte Carlo simulations of square and triangular platelets with enthalpic shape-specific and edge-specific patches.[20] We find large isotropic bandgaps for both the TE ($\Delta\omega/\omega_{mid-gap}$ up to 29.6%) and TM ($\Delta\omega/\omega_{mid-gap}$ up to 29.3%) polarizations in the $3^2.4.3.4$ tiling. Relative dielectric contrasts were varied for each particle geometry independently over the range 2 to 16, mimicking binary materials assembly. A wide range of interparticle spacings and relative dielectric contrasts promote bandgaps. Displacement field distributions indicate a bandgap origin of Lorenz-Mie scattering for direct structures (i.e. high dielectric particles in an air matrix) and dielectric band-air band or dielectric band-dielectric band for inverted structures (i.e. air pores in a high dielectric matrix).

Additionally, near all-angle negative refraction (AANR) and self-collimation of light are demonstrated for the $3^{2}.4.3.4$ tiling using finite difference time domain (FDTD) methods. These properties are desirable for applications including superlenses (sub-wavelength imaging), waveguideless confinement of light and nonlinear optics.

Methods

The model $3^{2}.4.3.4$ Archimedean tiling [Figure 4.1(a)] is composed of two squares and four triangles on a square lattice and displays P4gm plane group symmetry. The side length of the triangle and square cross-section rods are described by a basis size parameter, R_p. This size parameter describes the fractional side length with respect to the tangent rod case and was varied from 0.7 to 0.9. The square rods are centered at the points $(0,0,0)$ and $(a/2, 0, 0)$ where the lattice constant $a = 1$, and the triangular rods are centered at

$$\left(\frac{a}{2} - \frac{a}{2\sqrt{6}+6\sqrt{2}}, \frac{a}{2\sqrt{6}+6\sqrt{2}}, 0\right), \left(\frac{a}{2\sqrt{6}+6\sqrt{2}}, \frac{a}{2} + \frac{a}{2\sqrt{6}+6\sqrt{2}}, 0\right), \left(\frac{a}{2} + \frac{a}{2\sqrt{6}+6\sqrt{2}}, a - \frac{a}{2\sqrt{6}+6\sqrt{2}}, 0\right), \text{ and}$$

$$\left(a - \frac{a}{2\sqrt{6}+6\sqrt{2}}, \frac{a}{2} - \frac{a}{2\sqrt{6}+6\sqrt{2}}, 0\right). \text{ Square and triangular rods are rotated 15 degrees and 45}$$

degrees from the lattice vector, respectively. The side length for both rod types is $R_p / (1 + \sqrt{3})$. The dielectric filling fraction parameter η_d is described as the area fractions of the square rod, triangular rod and matrix regions weighted by their respective dielectric contrasts relative to air (ε_x where x= square, triangle or matrix)—

$$\eta_d = (\varepsilon_{square} A_{square} + \varepsilon_{triangle} A_{triangle} + \varepsilon_{matrix} A_{matrix}) / A_{total}$$

The filling fraction parameter as a function of R_p was calculated from the expression

$$\eta_d = 2 \times (2 - \sqrt{3}) \varepsilon_{square} R_p^{2} + \sqrt{3} \times (2 - \sqrt{3}) \varepsilon_{triangle} R_p^{2} + \varepsilon_{matrix} (1 - R_p^{2})$$
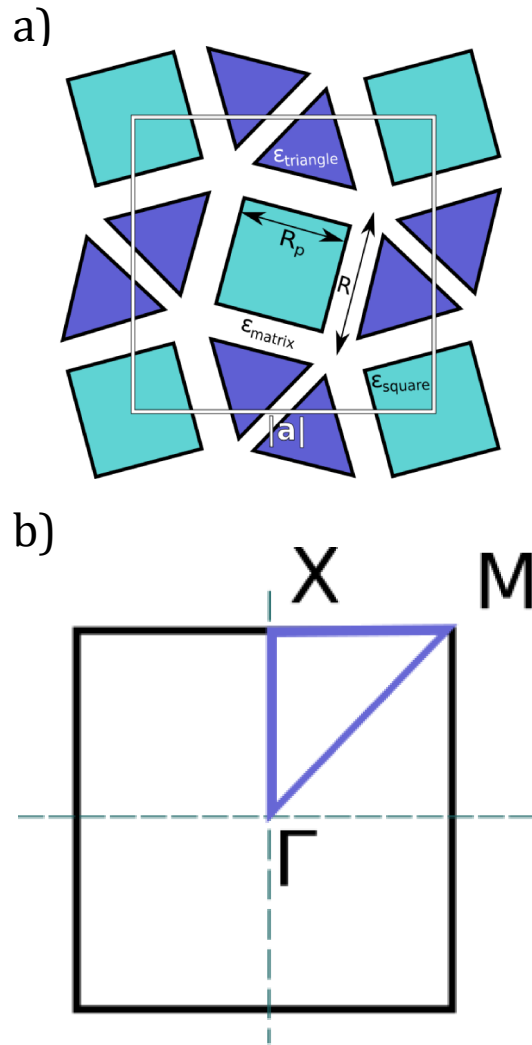
Figure 4.1. a) Schematic of Archimedean tiling $3^{2.}4.3.4$. The unit cell contains square rods with dielectric constant ε_{square} and four triangular rods with dielectric contrast $\varepsilon_{triangle}$. Rods have side lengths equal to $R_p = R \times p$ where R is the side length for tangent rods, and p is the particle spacing parameter expressed in fraction of R. The unit cell is outlined in white. **b)** First Brillouin zone of $3^{2.}4.3.4$ structure with square symmetry. High symmetry points are marked and the irreducible Brillouin Zone is outlined in purple.

and is plotted in Figure 4.S1. The area fraction of solid ($A_{dielectric}$ / A_{total}) is $R_p{}^2$ for the direct structure and $1 - R_p{}^2$ for the inverted structure.

Photonic band structures were simulated using the MIT Photonic Bands (MPB) software package. Figure 4.1(b) displays the square Brillouin zone, with high symmetry points (Γ, X and M) of the irreducible Brillouin zone labeled. The guided modes were evaluated for direct and inverted structures at dielectric contrasts from 2 to 16. Dispersion curves of light frequency versus wave-vector were calculated along a path through high symmetry points [Figure 4.1(b)]. The first twenty bands were determined by interpolating 100 points between the high symmetry k-points of the irreducible Brillouin zone. The high number of k-points provide detailed band behavior to produce EFCs. For transverse electric (TE) and transverse magnetic (TM) modes, frequencies were calculated within a tolerance of $\pm$ 0.001%. For the typical case, 4096 plane waves were produced by setting the resolution grid size to |a|/64. A mesh grid size of 5 was utilized to average the dielectric constant between grid points. For slow light simulations, a supercell (32 unit cells) with a linear defect was utilized to calculate the frequency of the defect mode, with 105 bands calculated in total. For slow light simulations, a supercell model (32 unit cells) with a linear defect was utilized to calculate the frequency of the defect mode and 105 bands were calculated in total. For slab simulations, a spacing of eight times the slab height was used included in the simulation to isolate the modes.

Frequency values were plotted over reciprocal space and interpolated to produce contours of constant frequency (equifrequency contours, EFCs). In brief, the EFC analysis is as described below. For an incident beam on a square lattice PC, the wavevector magnitude is is $|k_{incident}| = \omega|a| / 2\pi c$. Within the PC, the component of the wavevector (k_{PC}) parallel to the surface of incidence is conserved. Conservation of energy dictates that the frequency be conserved, allowing solutions to be determined by a geometric analysis where a construction

line parallel to the surface normal is overlaid on the EFC. Intersections of this line with PC

contours of equivalent frequency to the incident k-vector constitute solutions (i.e. modes that

propagate within the PC). An additional constraint applies to the incident frequency (on the

ΓX surface) to prevent higher order Bragg diffraction— $\omega|a| / 2\pi c \leq 0.5$.[21]

The refraction and handedness of the solution are determined by the group velocity

$v_g = \nabla_k \omega$ and the phase velocity $v_\phi = \omega/k$. Refracting or reflecting modes arise for the

following conditions on the wavevector components perpendicular to the PC surface,

respectively:

$$v_{g,\ incident}^{\perp} \cdot v_{g,\ PC}^{\perp} > 0$$

(Equation 3.1)

$$v_{g,\ incident}^{\perp} \cdot v_{g,\ PC}^{\perp} < 0$$

(Equation 3.2)

Negative refraction occurs at an obtuse angle for parallel components of the group velocity in

air ($v_{g,\ incident}^{\parallel}$) and in the PC ($v_{g,\ PC}^{\parallel}$), i.e., $v_{g,\ incident}^{\parallel} \cdot v_{g,\ PC}^{\parallel} < 0$. This indicates that the

incident and refracted beams lie on same side of the surface normal. The handedness of the

propagation in the photonic crystal is determined by $v_{g,\ PC} \cdot v_{\phi,\ PC} < 0$ and

$v_{g,\ PC} \cdot v_{\phi,\ PC} > 0$, which imply left-handed and right-handed refraction, respectively.[21]

Light propagation was also simulated using finite difference time domain (FDTD)

methods, specifically MIT Electromagnetic Equation Propagation (MEEP) software for

refraction and slow light studies. For the FDTD simulations, the time step resolution was Δt

$= S\,\Delta x$, where S is the Courant factor of 0.5 and Δx is the spatial resolution of 32. Frequencies

were normalized for a unit cell with length of 1.0 and the dielectric constant was not spatially

averaged. A perfectly matched layer of thickness $5|a|$ ($2|a|$) surrounded the simulation region

for the refraction (slow light) studies. Simulations were performed on the E_z component of TM

polarized sources. PCs are oriented with the ΓX crystal surface as the incident surface for refraction studies. Rods at the PC interface were not truncated at the edge of the unit cell. Continuous point sources were centered at one unit cell distance from PC within a simulation box size of 20 x 30 unit cells. Point source simulations were run for a total of 196 time steps (units $c/|\mathbf{a}|$) for refraction studies. Slow light simulations were performed on waveguide line defects (width $|\mathbf{a}|$) in the ΓX direction with a length of 42 unit cells. A point source located in the center of the waveguide propagated for a total of 10^4 time steps. A slow light simulations was performed for a waveguide line defect (width $|\mathbf{a}|$) in the ΓX direction with a length of 42 unit cells. A point source located in the center of the waveguide propagated for a total of 10^4 time steps.

To simulate the propagation of a beam through a PC, we modeled a Gaussian beam incident on a PC with a thickness of 20 unit cells. The Gaussian beam was centered at the edge of the perfectly matched layer in a simulation box size of 80 x 80 unit cells. The Gaussian profile beam size ω_o was 11 unit cells. The temporal width of the smoothing parameter was set to 5 and the beam propagated for 9.87 x 10^{-7} seconds with a total of 296 time steps. The axial propagation distance is offset by the constant 0.15$|\mathbf{a}|$.

Results and Discussion

Contour maps of the TM bandgap size as a function of rod size parameter (R_p) and dielectric contrasts ($\varepsilon_{triangle}/\varepsilon_{air}$, $\varepsilon_{square}/\varepsilon_{air}$) are provided for the direct structure in Figure 4.2. The direct structure supports large TM bandgaps between the second and third (2-3), fourth and fifth (4-5), and sixth and seventh (6-7) bands. All bandgaps open at low dielectric contrast, as shown in Table 4.S1. Bandgap sizes increase with basis spacing (i.e. low R_p). The 2-3 and 6-7 gaps are simultaneously maximized ($\Delta\omega/\omega_{mid\text{-}gap}$ = 27.3% and $\Delta\omega/\omega_{mid\text{-}gap}$ =
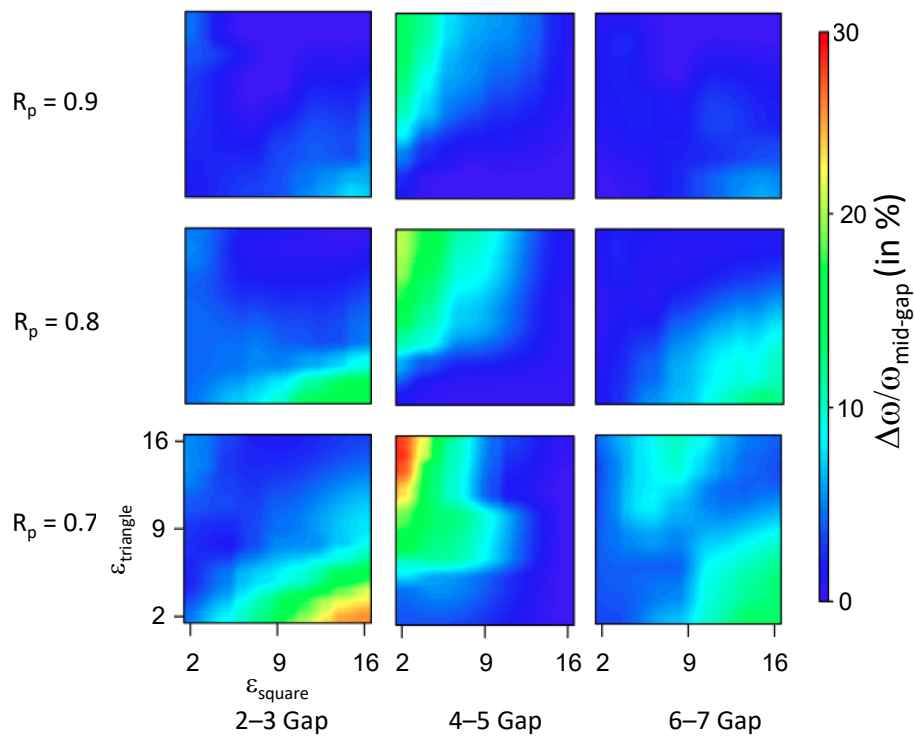
Figure 4.2. Contour map of the gap size $\Delta\omega/\omega_{\text{mid-gap}}$ for TM polarization in the direct structure.

18.1%, respectively) for high ε_{square} and low $\varepsilon_{triangle}$. In contrast, multiple bandgaps within a single structure generally undergo bandgap competition[22] and are not optimized under the same structural parameters. The 4-5 gap is largest (up to $\Delta\omega/\omega_{mid-gap} = 29.3\%$) for low ε_{square} and high $\varepsilon_{triangle}$, and occurs for all values of R_p. The dielectric filling fraction parameter η_d maintains values between 5 and 9 in structures supporting bandgaps. This range of η_d values is achieved for large and small differences between ε_{square} and $\varepsilon_{triangle}$ for the rod shapes as illustrated by Figure 4.S1. A large region of the ε_{square}, $\varepsilon_{triangle}$ map at $R_p = 0.7$ has η_d in the desired range and this corresponds to the richest bandgap regions in the contour map (Figure 4.2). Similar to many binary PCs, large bandgap sizes are promoted when the composition of the three-component PC consists of a high dielectric component (i.e., ε_{square} or $\varepsilon_{triangle}$) contrasted with low dielectric components (i.e., ε_{matrix} and complementary shape).

The TM photonic band structure for the direct $3^2.4.3.4$ structure is provided in Figure 4.3. In Figure 4.3(a), the 2-3 and 6-7 bandgaps are indicated in gray for high dielectric square rods ($\varepsilon_{square} = 16$, $\varepsilon_{triangle} = 2$, $R_p = 0.7$). Structures with dual bandgaps are of interest for systems that require synchronous manipulation of distinct signals, or photonic isolation of a waveguide light source from electrical contacts.[23,24] In addition, engineering band curvature has been utilized to promote refraction properties for subwavelength imaging and, in the limit of no curvature (i.e., flat bands), to enhance light extraction from LEDs.[14,15] Relatively flat bands surround the 6-7 gap with 10% change in frequency across the irreducible Brillouin zone, whereas the bands surrounding the 2-3 gap display high anisotropy (42% and 18% for bands 2 and 3, respectively). For high dielectric triangular rods [Figure 4.3(b)] there is a single 4-5 gap ($\varepsilon_{square} = 2$, $\varepsilon_{triangle} = 16$, $R_p = 0.7$). These bandgap sizes are comparable with those found in lithographically designed Archimedean tilings,[11] and larger than those found for other self-assembly routes to Archimedean tiling structures.[19] The fourth and fifth bands
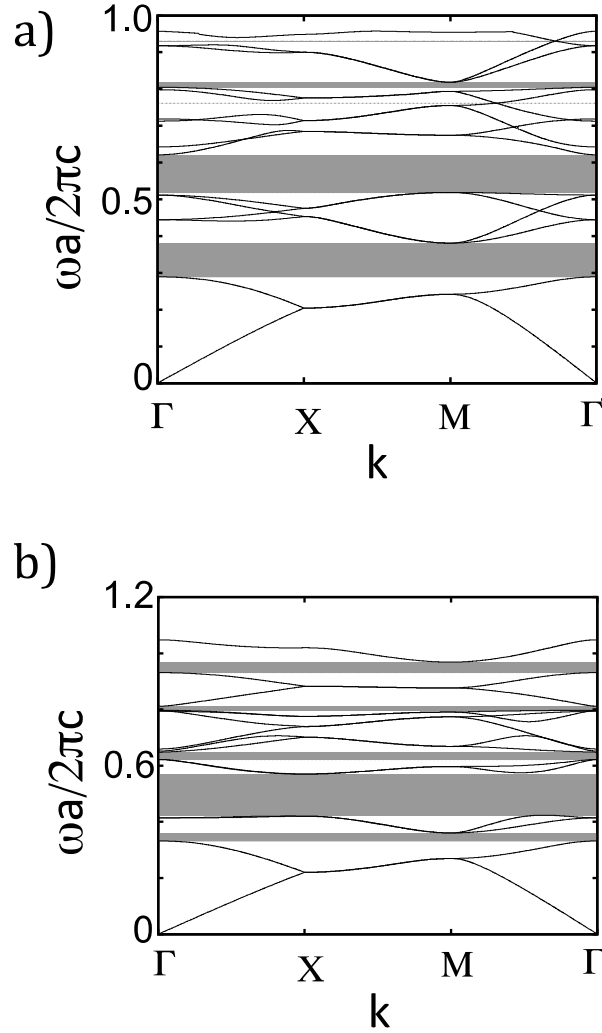
Figure 4.3. a) TM polarization band diagram for the direct $3^2.4.3.4$ Archimedean tiling with $\varepsilon_{square} = 16$ and $\varepsilon_{triangle} = 2$, and $R_p = 0.7$. The TM bandgaps have sizes $\Delta\omega/\omega_{mid\text{-}gap} = 27.3\%$ for the 2-3 gap and $\Delta\omega/\omega_{mid\text{-}gap} = 18.1\%$ for the 6-7 gap. **b)** TM polarization band diagram for the direct structure with $\varepsilon_{square} = 2$, $\varepsilon_{triangle} = 16$, and $R_p = 0.7$. The 4-5 TM bandgap size is $\Delta\omega/\omega_{mid\text{-}gap} = 29.4\%$.

surrounding the gap exhibit 8.6% and 10% change in frequency across the irreducible Brillouin zone, respectively. No TE bandgaps greater than 5% were found in the direct structure as TE bandgaps are primarily found in interconnected networks of high dielectrics.[1]

We assess the field concentrations in the direct $3^2.4.3.4$ structure to clarify the mechanisms of bandgap formation. The TM electric displacement field, i.e., dielectric contrast multiplied by the electric field, was examined at the Γ high symmetry point. Figures 4.4(a-f) show the displacement fields for bands 2-7 in the structure with high dielectric square rods. In this case, the TM bandgaps form due to the energy differences of consecutive Lorenz-Mie resonances in the high dielectric rods.[25] Specifically, Figure 4.4(a) shows the in-phase oscillations and Figures 4.4(b-e) show the anti-phase oscillations (with nodal plane) that produce the 2-3 bandgap. Figure 4.4(f) displays a higher order Lorenz-Mie resonance in band 7, which has a ring-like nodal pattern within the square rod and opens the 6-7 bandgap. Figures 4.4(g-j) displays the displacement fields for bands 2-5 in the structure with high dielectric triangular rods. The energy difference between the in-phase [Figures 4.4(g-i)] and anti-phase Lorenz-Mie resonances [Figure 4.4(j)] leads to the 4-5 bandgap. Lorenz-Mie resonance-type bandgaps are desirable due to their insensitivity to disorder as the resonances promote an attractive potential for photons in isolated dielectric scatterers.[26,27]

To investigate the impact of finite height on the Archimedean tiling, quasi-2D 'slab' simulations were performed for the direct structure with $\varepsilon_{square} = 16$, $\varepsilon_{triangle} = 2$ and $R_p = 0.7$. Slab bandgaps are typically more modest than their 2D counterparts. In the band diagram [Figure 4.5(a)], a lightcone is overlaid to indicate the modes not contained in the slab *via* total internal reflection. The gap size as a function of slab height is shown in Figure 4.5(b), and several gaps are available over the slab height range 0.1a to 1.5a. The 6-7 bandgap size reaches a maximum of 21.8% for h = 0.45. For h < 0.45, the upper bounding band lies entirely within the lightcone and frequencies in the bandgap are not contained to the slab. As the bands
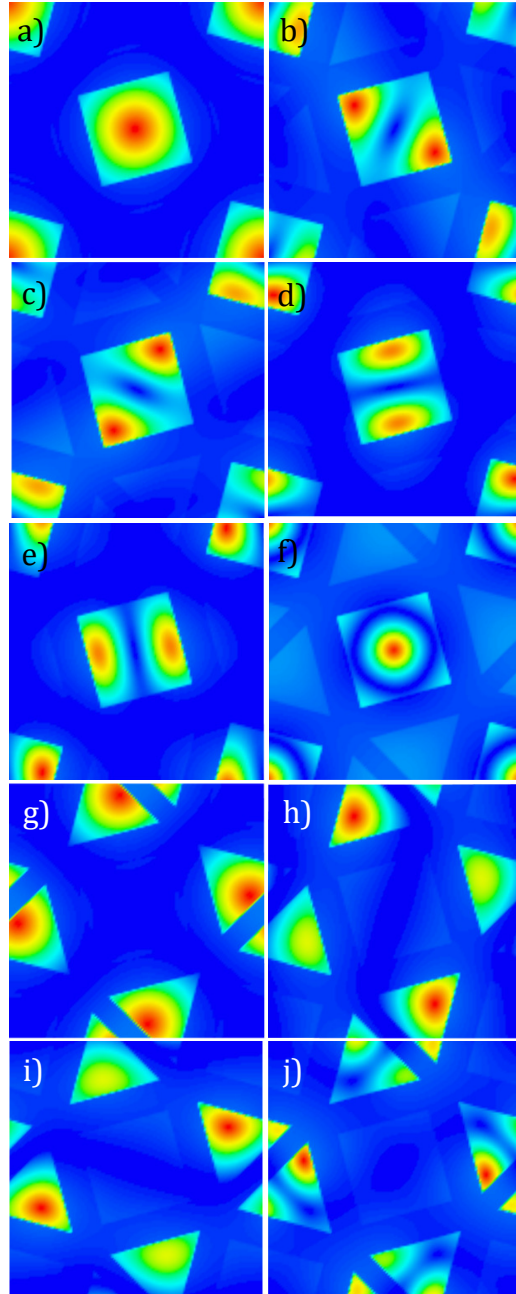
Figure 4.4. a-f) TM electric displacement field density for bands 2-7 (a-f) in the direct $3^2.4.3.4$ structure with $\varepsilon_{square} = 16$, $\varepsilon_{triangle} = 2$, and $R_p = 0.7$. The bandgaps lie between bands 2-3 and 6-7. **g-j)** Electric displacement density for bands 2-5 (g-j) with $\varepsilon_{square} = 2$, $\varepsilon_{triangle} = 16$, and $R_p = 0.7$. The bandgap lies between bands 4 and 5.

a)

b)
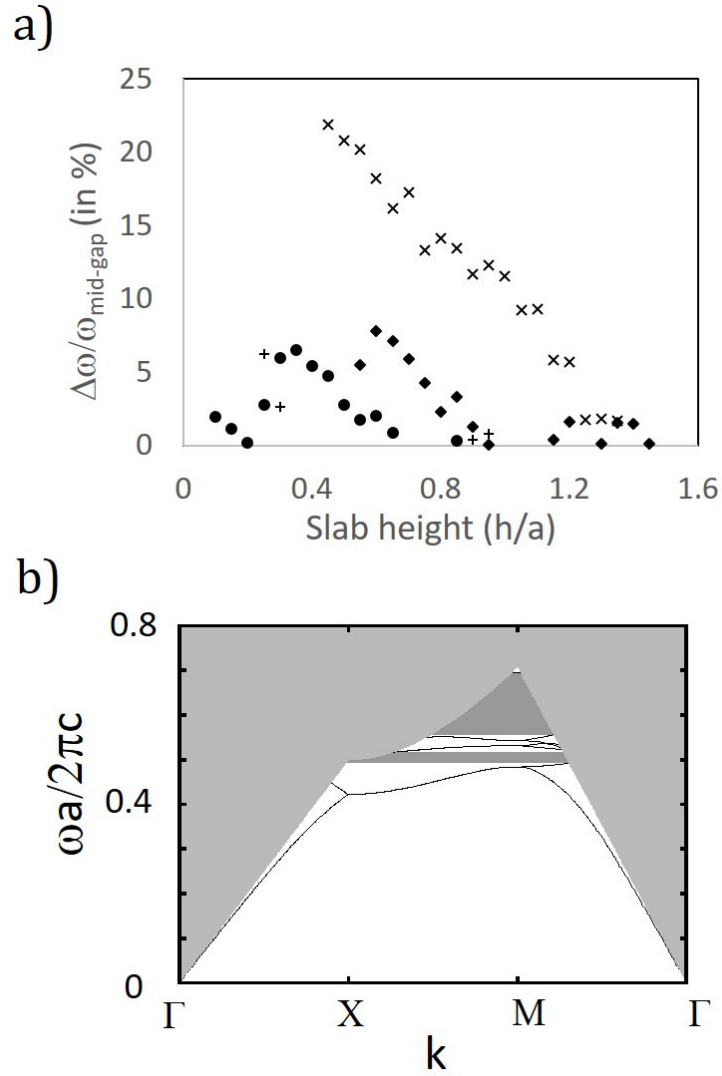
Figure 4.5 a) TM gap sizes $\Delta\omega/\omega_{\text{mid-gap}}$ for direct slab structure with $\varepsilon_{\text{square}} = 16$ and $\varepsilon_{\text{triangle}} = 2$, and $R_p = 0.7$ as a function of slab height. Gap size is plotted for 2-3 (circle), 4-5 (plus), 6-7 (cross), and 8-9 (diamond) gaps. **b)** TM polarization band diagram for the direct $3^2.4.3.4$ Archimedean tiling with $\varepsilon_{\text{square}} = 16$ and $\varepsilon_{\text{triangle}} = 2$, $R_p = 0.7$ and $h = 0.45$. The TM bandgaps have sizes $\Delta\omega/\omega_{\text{mid-gap}} = 21.8\%$ for the 6-7 gap and $\Delta\omega/\omega_{\text{mid-gap}} = 4.7\%$ for the 2-3 gap.

76

are suppressed to lower frequency for h > 0.45, the gap size is reduced. Additionally, gap competition between smaller 2-3, 4-5, and 8-9 bandgaps and the large 6-7 gap is observed.

For the inverted $3^{2}.4.3.4$ arrangement, the structure is composed of square and triangular pores separated by high dielectric matrix (i.e., $\varepsilon_{square} = 1$, $\varepsilon_{triangle} = 1$, $\varepsilon_{matrix} > 1$). The TE bandgap size is mapped as a function of pore size parameter (R_{p}) and dielectric constant (ε_{matrix}) in Figure 4.6(a). The gap lies between bands 6-7 and large values of bandgap size are achieved for ε_{matrix} between 9 and 16 over the full range of pore size parameter. Figure 4.6(b) displays the band diagram for the structure with maximum gap size ($\varepsilon_{matrix} = 16$, $R_{p} = 0.8$, $\Delta\omega/\omega_{mid-gap} = 29.6\%$). The area fraction in this case is 36% and lies within the typical range reported for large bandgaps (e.g., 22.5%-43%).[28] In particular, the optical path lengths in the materials should be roughly equal and therefore for high dielectric constant materials the filling fraction should be low to support large bandgaps.[29]

The inverted structure also supports a TM bandgap between the bands 4-5. The contour map of bandgap size as a function of R_{p} and ε_{matrix} is shown in Figure 4.7(a). Generally, TM bandgaps are supported in structures with concave dielectric structures that allow resonances.[25] However, here the bandgap size is large for narrow dielectric veins ($R_{p} \geq$ 0.8) and sharply decreases as the veins thicken, similar to circular cross-section air holes in a square lattice.[1] Fig 7(b) displays the band diagram for the structure with the largest bandgap ($\varepsilon_{matrix} = 16$ and $R_{p} = 0.9$, $\Delta\omega/\omega_{mid-gap} = 16.8\%$). There are no complete bandgaps in the inverted PC because no overlap in frequency between TE and TM gaps occurs.

The electric displacement fields at the Γ high symmetry point for the TE and TM polarizations in the inverted structures are displayed in Figure 4.8. Figures 4.8(a-f) display the TE displacement fields for bands 2-7 in the structure with $\varepsilon_{matrix} = 16$ and $R_{p} = 0.8$. Here, the field is concentrated in the dielectric matrix surrounding the air pores (square and triangular) for the modes below the bandgap, and shifts into the air pores in the mode above the bandgap.
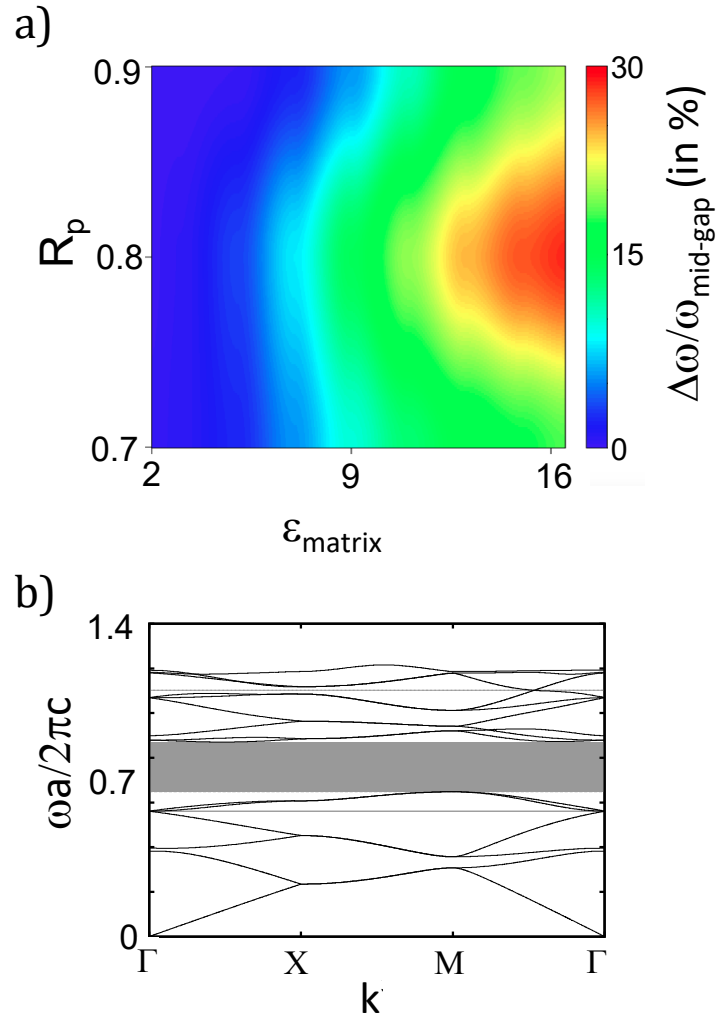
Figure 4.6. a) Contour map of gap size $\Delta\omega/\omega_{mid\text{-}gap}$ as a function of ε_{matrix} and R_p. **b)** TE polarization band diagram for the inverted $3^2.4.3.4$ structure with $R_p = 0.8$ and $\varepsilon_{matrix} = 16$. The 6-7 bandgap size is $\Delta\omega/\omega_{\mu\iota\delta-\gamma\alpha\pi} = 29.7\%$.
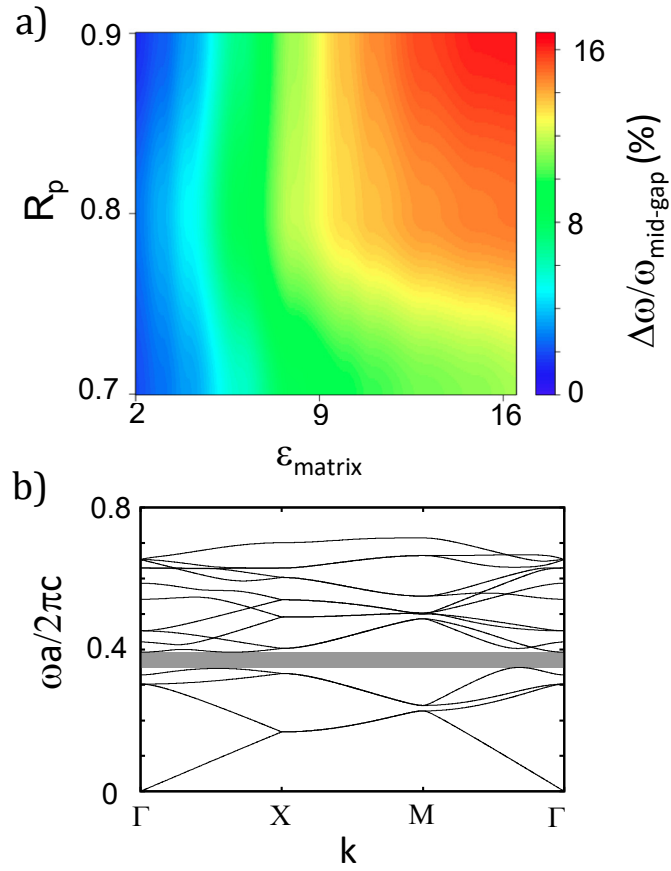
Figure 4.7. a) Contour map of the gap size $\Delta\omega/\omega_{\text{mid-gap}}$ as a function of $\varepsilon_{\text{matrix}}$ and R_p. **b)** TM polarization band diagram for the inverted $3^2.4.3.4$ structure with $R_p = 0.9$ and $\varepsilon_{\text{matrix}} = 16$. The TM 4-5 bandgap size is $\Delta\omega/\omega_{\text{mid-gap}} = 16.8\%$.
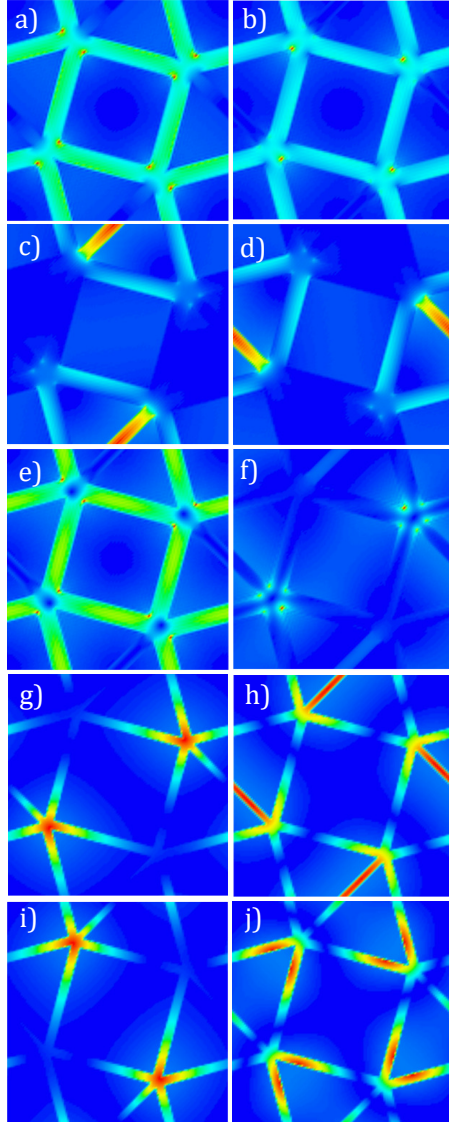
Figure 4.8. a-f) TE electric displacement field distribution for bands 2-7 (a-f) in the inverted structure with $R_p = 0.8$ and $\varepsilon_{matrix} = 16$. Bandgaps lie between bands 6 and 7 in this structure. **g-j)** Electric displacement density distribution for TM polarization for bands 2-5 (g-j) in the inverted structure with $R_p = 0.9$ and $\varepsilon_{matrix} = 16$. Bandgaps lie between bands 4 and 5 in this structure.

This transition between 'dielectric bands' and 'air bands' is commonly found in PCs and is attributed to a combination of Mie and Bragg scattering.[1,12] Figures 4.8(g-j) display the TM displacement fields for bands 2-5 in the structure with ε_{matrix} = 16 and R_p = 0.9. In contrast to the TE case, this bandgap arises from re-distribution of the mode within the high dielectric, which results in a large energy difference between the modes.[25] The lowest energy mode fields are concentrated in the dielectric matrix (i.e., five arm star) for the modes below the bandgap. The lower bounding band exhibits localization to three arms of the star motif, while the upper bounding band is concentrated in complementary arms of the star motif.

The refraction properties for the second TM band in the direct structure with ε_{square} = 16, $\varepsilon_{triangle}$ = 2 and R_p = 0.7 are shown in Figure 4.9. The contours of equal frequency are mapped over the first Brillouin zone (marked) with high symmetry points labeled in Figure 4.9(a). EFC analysis is performed [Figure 4.9(b)] for $\omega a/2\pi c$ = 0.27 with 30° incident angle ($\boldsymbol{k_{incident}}$) on the ΓX interface. Two solutions are found ($\boldsymbol{k_{refraction}}$ and $\boldsymbol{k_{reflection}}$) with group velocities ($\boldsymbol{v_{g,\ refraction}}$ and $\boldsymbol{v_{g,\ reflection}}$) plotted. Negative refraction is apparent because $\boldsymbol{k_{incident}}$ and $\boldsymbol{v_{g,\ refraction}}$ lie on the same side of the normal to the surface when placed head-to-tail. Left-handed negative refraction (LHNR) is verified using FDTD methods, as pictured in Figure 4.9(c), where a Gaussian beam is allowed to propagate through the $3^2.4.3.4$ slab.

In Figures 4.9(a) and 4.9(b), the concave contour lines around the Γ high symmetry point for all angles indicate a wide availability of incident angles with negative refraction, suggesting nearly AANR for normalized frequencies in the range 0.255-0.85. Negative refraction for $\omega|\boldsymbol{a}|/2\pi c$ = 0.27 occurs at angles of incidence between -75° and 75°, with higher incident angles blocked by the bandgap. For the PC thickness of 2|$\boldsymbol{a}$| unit cells at constant frequency, an image of the source is obtained, as shown in Figure 4.9(c). Flatlens imaging is

Figure 4.9. a) EFC of TM polarization band 2 for direct structure with $\varepsilon_{square} = 16$, $\varepsilon_{triangle} = 2$, and $R_p = 0.7$. **b)** Refraction analysis for Gaussian beam with frequency $\omega a/2\pi c = 0.27$ with 30° incident angle on the ΓX interface (note that the group velocity vectors are plotted to show direction and do not represent the magnitude). Refraction analysis predicts left-handed negative refraction. **c)** Gaussian beam with frequency and incident angle from (b). Blue, white and red correspond respectively to negative, zero and positive E_z fields in Figs. (c-e). **d)** Point source with frequency $\omega a/2\pi c = 0.27$ placed one unit cell away from a PC flat lens with 2 unit cells. The PC promotes almost AANR. **e)** Point source with frequency $\omega a/2\pi c = 0.27$ placed one unit cell away from a PC flat lens with 7 unit cells, showing self-collimation.

made possible by the nearly AANR in the PC. The distortion in the image occurs because the smaller incident angles show weaker refraction. These results are on par with the best AANR structures designed with photolithography,[30] and demonstrate the promise of self-assembled PC structures as a means of achieving low loss flat lenses.

The flat regions of the bands in Figure 4.9(a) promote beam collimation for thicker PCs, as pictured in Figure 4.9(e). A point source with $\omega a/2\pi c = 0.27$ placed close (i.e., 1 unit cell distance) to the PC experiences collimation on passing through the PC, for incident angles -45° to 45°. At larger incident angles, the light is refracted to larger angles and is absorbed by the perfectly matched layer.

The EFCs for the second TM band in the direct structure with $\varepsilon_{square} = 2$, $\varepsilon_{triangle} = 16$, and $R_p = 0.7$ are depicted in Figure 4.10(a). Figure 4.10(b) displays the EFC contour analysis for $\omega|\mathbf{a}|/2\pi c = 0.32$, which predicts LHNR refraction with large negative effective index, as indicated by the large angle between $\boldsymbol{v_{g,\ refraction}}$ and $\boldsymbol{k_{perpendicular}}$. FDTD simulations

pictured in Figure 4.10(c) verify LHNR in the structure. Since band structure in the lower modes is primarily determined by the symmetry of the structure, Figure 4.10(a) displays concave EFCs, similar to Figure 4.9(a).[11] In Figure 4.10(d), a point source with $\omega|\mathbf{a}|/2\pi c = 0.32$ is placed at 1 unit cell distance from a PC slab and allowed to propagate. Nearly AANR is observed at $\omega|\mathbf{a}|/2\pi c = 0.30$ for incident angles between -50° and 50°, with other incident angles blocked by a small bandgap [see Figure 4.3(b)]. The half-wave distance is 0.45λ for the image source (measured parallel to the PC surface), clearly demonstrating sub-wavelength imaging. As illustrated in Figure 4.10(e), self-collimation is additionally observed for incident angles in the range (-25°, 25°).

Slow light properties were investigated for a line defect waveguide along the ΓX direction in the direct structure ($\varepsilon_{square} = 2$, $\varepsilon_{triangle} = 16$, $R_p = 0.8$). The TM band diagram
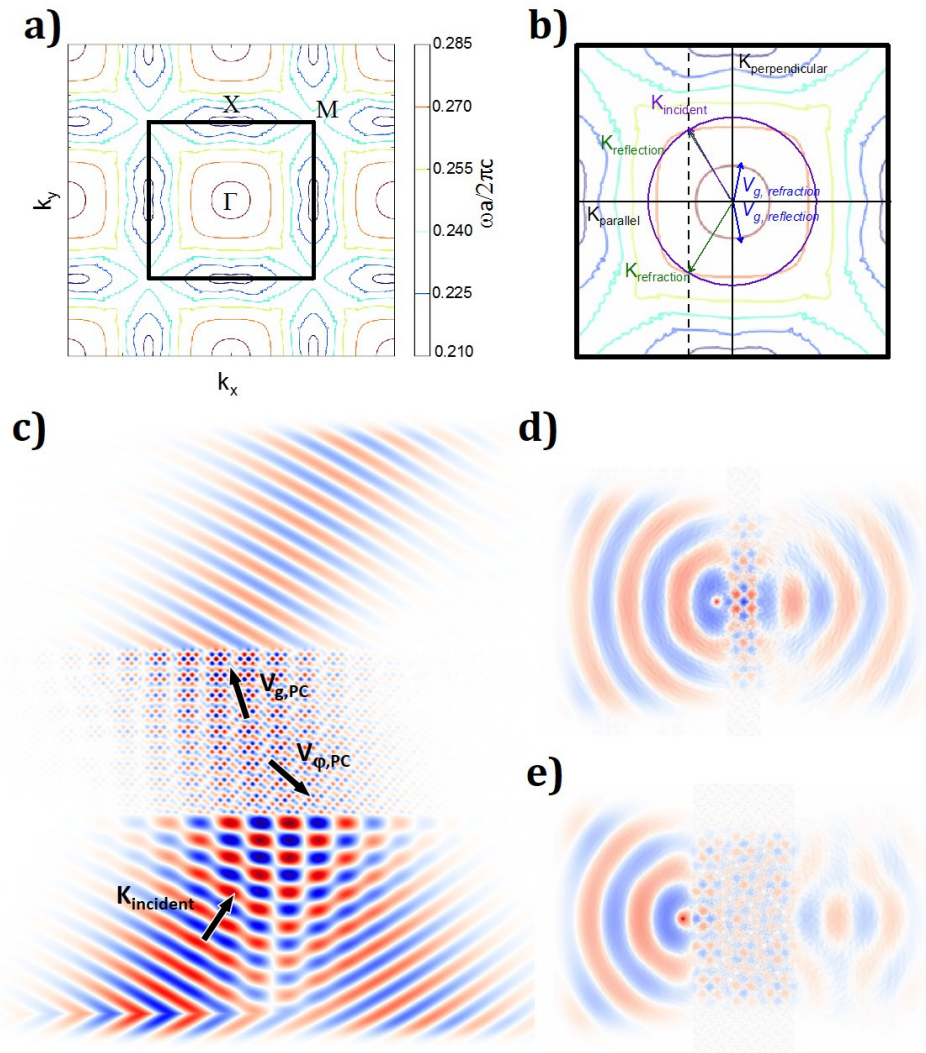
83
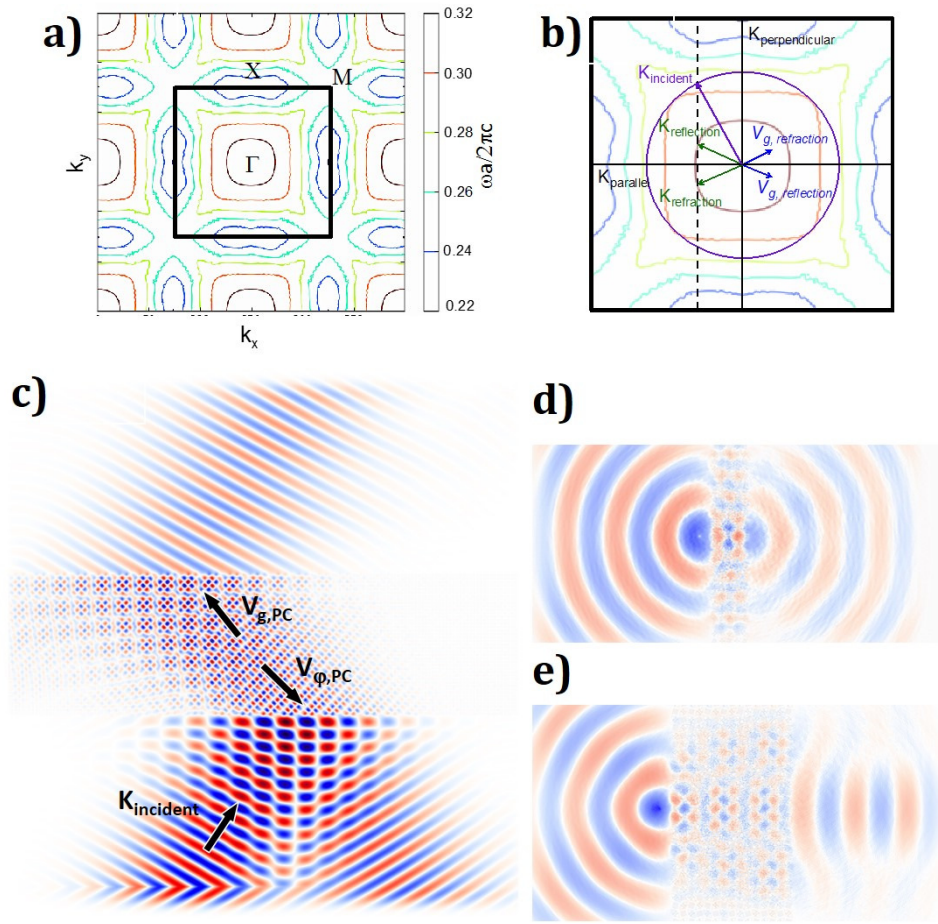
Figure 4.10. a) EFC of TM polarization band 2 for the direct structure with $\varepsilon_{square} = 2$, $\varepsilon_{triangle} = 16$, and $R_p = 0.7$. **b)** Refraction analysis for Gaussian beam with frequency $\omega a/2\pi c = 0.32$ at an incident angle of 30° on the ΓX interface. Refraction analysis predicts left-handed negative refraction. **c)** Gaussian beam with frequency and incident angle from (b). **d)** Point source with frequency $\omega a/2\pi c = 0.30$ placed one unit cell away from a PC flat lens with 2 unit cells produces almost AANR. **e)** Point source with frequency $\omega a/2\pi c = 0.32$ placed one unit cell away from a PC flat lens with 7 unit cells, demonstrating collimation of the point source into a beam.

for the waveguide in Fig. 11(a) displays a highly isotropic defect band (0.6% frequency change across k-space) at $\omega|\mathbf{a}|/2\pi c = 0.436$. The slowdown factor $S = v_{\varphi}/v_g$ has values in the range 10^3 to 10^5 for the k-vector range. Typical values for S are in the range of 10^2, but values up to $\sim 10^3$ have been reported.[31,32] Slow light is confirmed with FDTD simulations shown in Fig. 11(b) where a point source with frequency $\omega|\mathbf{a}|/2\pi c = 0.436$ is placed at the center of the waveguide and allowed to propagate. The resulting electric field intensity was 75 times the initial amplitude, demonstrating the compression of the signal within the waveguide. Figure 4.S2 displays the E_z profile with scale set to the amplitude of the point source emission. The emitted light from the waveguide has a similar spatial distribution to the point source, but the amplitude has been enhanced outside the waveguide by a factor of 2. Such waveguides are desirable in enhancing optical nonlinearities such as second- and third-harmonic generation, where signals are typically weak.[33]

With regard to fabrication of the Archimedean PC, the $3^2.4.3.4$ structure can form if interactions between geometrically distinct particles are the most energetically favorable (i.e. triangles attracted to squares). Monodisperse building blocks with triangular and square geometries have been manufactured via photolithographic patterning of SU8 photoresists;[34] stop-flow lithography for high throughput;[35] and PRINT (particle replication in nonwetting templates) for roll-to-roll processing.[36] The latter can also directly generate high dielectric motifs.[37] Double inversion techniques can be utilized to prepare inorganic anisotropic particles with a range of dielectric constants.[38,39] A single infiltration of high dielectric material and template removal would produce the inverted PC.[40] Appropriate dielectric materials for supporting bandgaps and negative refraction in $3^2.4.3.4$ structures include Si ($\varepsilon = 12.0$), GaAs ($\varepsilon = 13.0$), Ge ($\varepsilon = 16$), and TiO$_2$ ($\varepsilon = 6.8$-8.4); as well as low dielectric constant materials Al$_2$O$_3$ ($\varepsilon = 3.1$), SiO$_2$ ($\varepsilon = 2.2$) and polymers ($\varepsilon \sim 2.2$). The inorganic
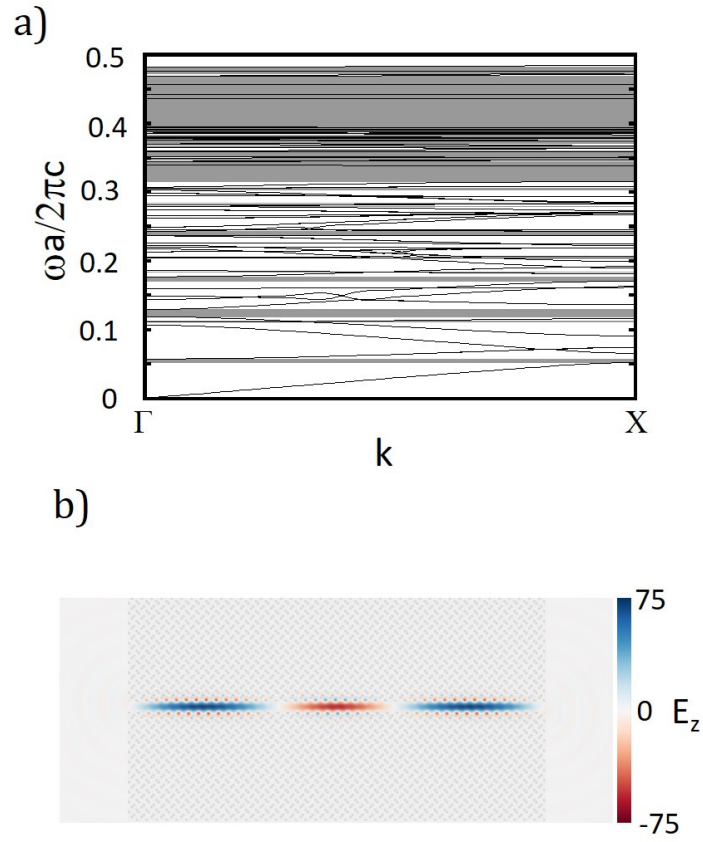
Figure 4.11. a) TM polarization band diagram for the inverted $3^2 \cdot 4 \cdot 3 \cdot 4$ structure with $R_p = 0.8$, $\varepsilon_{triangle} = 16$ and $\varepsilon_{square} = 2$ for a waveguide supercell. The slow light defect mode occurs at frequency $\omega a/2\pi c = 0.436$. **b)** FDTD of point source propagation through the waveguide. The point source has amplitude 1.0, and the snapshot is taken after 6141 time steps.

86

materials can be deposited via chemical vapor deposition, physical vapor deposition, or atomic layer deposition.[41,42] In addition, several approaches have been used to control inter-particle spacing including use of low ionic strengths (electrostatic interactions),[43] electric fields,[44] and polymerizable fluids between the particles.[45]

Conclusion

In summary, we find large TE and TM bandgaps in shape-binary tilings consistent with self-assembly of particle mixtures. These large bandgaps are comparable in size to those of structures requiring high precision lithographic design, but are achievable by colloidal fabrication and self-assembly techniques. In addition, the bandgaps open at low relative contrasts (i.e., low particle dielectric constants relative to the matrix and vice versa). Lorenz-Mie resonances in shaped scatterers are determined to be the physical origin of the TM bandgaps in the direct $3^2.4.3.4$ Archimedean tiling. Finite difference time domain (FDTD) simulations predict nearly AANR leading to subwavelength imaging and self-collimation from a point source, and slow light-based signal enhancement. For square and triangle dielectric constants of 2 and 16, respectively, the half-wave distance is 0.45λ for the TM polarized image source and demonstrates sub-wavelength imaging from the PC flatlens. Recently, thermodynamic simulations of shape-binary mixtures with enthalpic shape-specific or edge-specific patches predict the self-organization of all 11 semi-regular tilings. Our theoretical modeling distinctly points experimentalists in colloidal synthesis and assembly toward these high payoff target structures for photonics.

Gap Index	R_p	ε_{matrix}	$\varepsilon_{triangle}$	ε_{square}	Polarization	$\Delta\omega/\omega_{mid\text{-}gap}$
2-3	0.7	1	2	5	TM	4.4%
4-5	0.9	1	4	2	TM	2.3%
6-7	0.7	1	2	6	TM	1.1%
4-5	0.8	6	1	1	TE	4.0%
6-7	0.8	3	1	1	TM	1.6%

Table 4.S1. Minimum dielectric constant values supporting bandgaps in the $3^2.4.3.4$ shape-binary tiling.
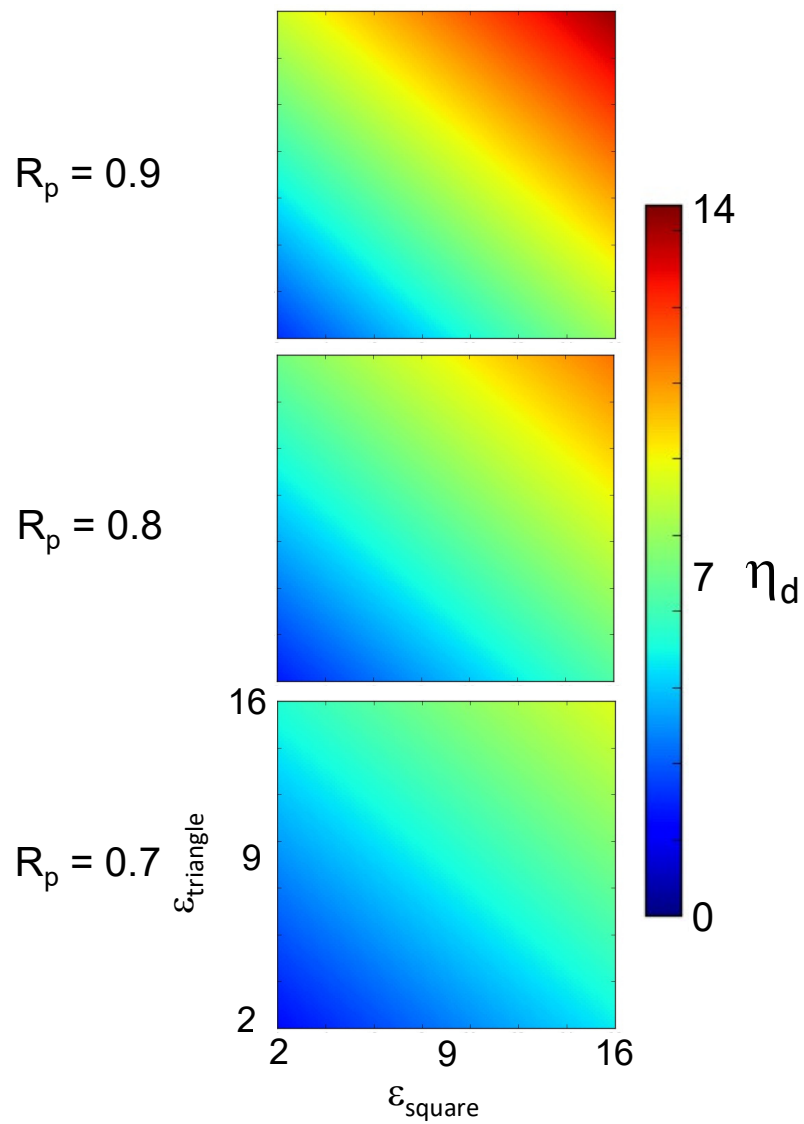
Figure 4.S1. Contour maps of dielectric fill fraction η_d in the direct structure as a function of constituent dielectric contrasts and particle spacing parameter.
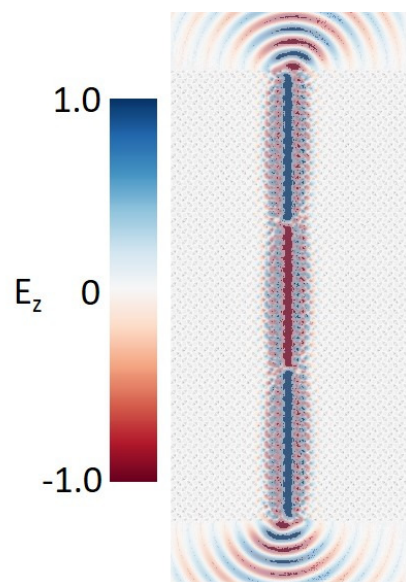
Figure 4.S2 FDTD of point source propagation through the waveguide. The color is scaled to the amplitude of the point source (1.0) and the snapshot is taken after 6141 time steps.

REFERENCES

[1]   R. D. Joannopoulos, John D., Johnson, Stephen G., Winn, Joshua N., Meade, *Molding the Flow of Light*, Princeton University Press, **2008**.

[2]   W. Zhang, N. Ganesh, I. D. Block, B. T. Cunningham, *Sensors Actuators, B Chem.* **2008**, *131*, 279.

[3]   A. Mihi, F. J. López-Alcaraz, H. Míguez, *Appl. Phys. Lett.* **2006**, *88*, 193110.

[4]   E. Cubukcu, K. Aydin, E. Ozbay, S. Foteinopoulou, C. M. Soukoulis, *Phys. Rev. Lett.* **2003**, *91*, 207401.

[5]   C. M. Anderson, K. P. Giapis, *Phys. Rev. Lett.* **1996**, *77*, 2949.

[6]   C. M. Soukoulis, *Phys. Scr.* **1996**, *T66*, 146.

[7]   M. Florescu, S. Torquato, P. J. Steinhardt, *Proc. Natl. Acad. Sci. U. S. A.* **2009**, *106*, 20658.

[8]   K. Edagawa, S. Kanoko, M. Notomi, *Phys. Rev. Lett.* **2008**, *100*, 13901.

[9]   W. Man, M. Megens, P. J. Steinhardt, P. M. Chaikin, *Nature* **2005**, *436*, 993.

[10]   S. David, A. Chelnokov, J. M. Lourtioz, *IEEE J. Quantum Electron.* **2001**, *37*, 1427.

[11]   D. Jovanović, R. Gajić, K. Hingerl, *Opt. Express* **2008**, *16*, 4048.

[12]   W. Man, M. Florescu, E. P. Williamson, Y. He, S. R. Hashemizad, B. Y. C. Leung, D. R. Liner, S. Torquato, P. M. Chaikin, P. J. Steinhardt, *Proc. Natl. Acad. Sci. U. S. A.* **2013**, *110*, 15886.

[13]   C. Wiesmann, K. Bergenek, N. Linder, U. T. Schwarz, *Laser Photonics Rev.* **2009**, *3*,

262.

[14] A. A. David, T. Fujii, E. Matioli, R. Sharma, S. Nakamura, S. P. Denbaars, C. Weisbuch, H. Benisty, *Appl. Phys. Lett.* **2006**, *88*, 10.

[15] M. Rattier, H. Benisty, E. Schwoob, C. Weisbuch, T. F. Krauss, C. J. M. Smith, R. Houdré, U. Oesterle, *Appl. Phys. Lett.* **2003**, *83*, 1283.

[16] D. V. Talapin, E. V. Shevchenko, M. I. Bodnarchuk, X. Ye, J. Chen, C. B. Murray, *Nature* **2009**, *461*, 964.

[17] X. Zeng, G. Ungar, Y. Liu, V. Percec, A. E. Dulcey, J. K. Hobbs, *Nature* **2004**, *428*, 157.

[18] a. Takano, W. Kawashima, a. Noro, Y. Isono, N. Tanaka, T. Dotera, Y. Matsushita, *J. Polym. Sci. Part B Polym. Phys.* **2005**, *43*, 2427.

[19] K. Ueda, T. Dotera, T. Gemma, *Phys. Rev. B - Condens. Matter Mater. Phys.* **2007**, *75*, 1.

[20] J. a Millan, D. Ortiz, G. van Anders, S. C. Glotzer, *ACS Nano* **2014**, *8*, 2918.

[21] R. Gajić, R. Meisels, F. Kuchar, K. Hingerl, *Opt. Express* **2005**, *13*, 8596.

[22] E. C. M. Vermolen, J. H. J. Thijssen, A. Moroz, M. Megens, A. van Blaaderen, *Opt. Express* **2009**, *17*, 6952.

[23] S. G. Romanov, H. M. Yates, M. E. Pemble, R. M. D. La Rue, *J. Phys. Condens. Matter* **2000**, *12*, 8221.

[24] J.-W. Gao, Y. Zhang, N. Ba, C.-L. Cui, J.-H. Wu, *Opt. Lett.* **2010**, *35*, 709.

[25] R.-L. Chern, S. D. Chao, *Opt. Express* **2008**, *16*, 16600.

[26]   C. Rockstuhl, F. Lederer, *New J. Phys.* **2006**, *8*, DOI 10.1088/1367-2630/8/9/206.

[27]   E. Lidorikis, M. M. Sigalas, E. N. Economou, C. M. Soukoulis, *Phys. Rev. B* **2000**, *61*, 13458.

[28]   P. R. Villeneuve, Michel Piche, *Phys. Rev. B* **1992**, *46*, 4973.

[29]   T. F. Krauss, R. M. De La Rue, *Prog. Quantum Electron.* **1999**, *23*, 51.

[30]   C. Luo, S. Johnson, J. Joannopoulos, J. Pendry, *Phys. Rev. B* **2002**, *65*, DOI 10.1103/PhysRevB.65.201104.

[31]   T. F. Krauss, *J. Phys. D. Appl. Phys.* **2007**, *40*, 2666.

[32]   J. P. Hugonin, P. Lalanne, T. P. White, T. F. Krauss, *Opt. Lett.* **2007**, *32*, 2638.

[33]   B. Corcoran, C. Monat, C. Grillet, D. J. Moss, B. J. Eggleton, T. P. White, L. O'Faolain, T. F. Krauss, *Nat. Photonics* **2009**, *3*, 206.

[34]   C. J. Hernandez, T. G. Mason, *J. Phys. Chem. C* **2007**, *111*, 4477.

[35]   P. Panda, K. P. Yuet, T. A. Hatton, P. S. Doyle, *Langmuir* **2009**, *25*, 5986.

[36]   K. P. Herlihy, J. Nunes, J. M. Desimone, *Langmuir* **2008**, *24*, 8421.

[37]   M. J. Hampton, S. S. Williams, Z. Zhou, J. Nunes, D. H. Ko, J. L. Templeton, E. T. Samulski, J. M. DeSimone, *Adv. Mater.* **2008**, *20*, 2667.

[38]   N. Tétreault, G. Von Freymann, M. Deubel, M. Hermatschweiler, F. Pérez-Willard, S. John, M. Wegener, G. A. Ozin, *Adv. Mater.* **2006**, *18*, 457.

[39]   T. Ruhl, P. Spahn, C. Hermann, C. Jamois, O. Hess, *Adv. Funct. Mater.* **2006**, *16*, 885.

[40]   C. López, *Adv. Mater.* **2003**, *15*, 1679.

[41]   S. M. George, *Chem. Rev.* **2010**, *110*, 111.

[42]   A. Stein, R. C. Schroden, *Curr. Opin. Solid State Mater. Sci.* **2001**, *5*, 553.

[43]   M. E. Leunissen, C. G. Christova, A.-P. Hynninen, C. P. Royall, A. I. Campbell, A. Imhof, M. Dijkstra, R. van Roij, A. van Blaaderen, *Nature* **2005**, *437*, 235.

[44]   T. Gong, D. W. M. Marr, *Langmuir* **2001**, *17*, 2301.

[45]   S. A. Asher, S. F. Peteu, C. E. Reese, M. X. Lin, D. Finegold, *Anal. Bioanal. Chem.* **2002**, *373*, 632.

CHAPTER 5

HIERARCHICAL FULLERENE ASSEMBLY: SEEDED CO-PRECIPITATION AND ELECTRIC FIELD DIRECTED- ASSEMBLY

Introduction

Hierachical assembly provides an avenue for controlling the formation of complex topologies over a range of length scales and is a hallmark of natural systems such as viruses, nacre, bone, and bamboo. Synthetic hierarchical materials have been prepared from block copolymers,[1] poly-(L-Lactic acid),[2] zeolites,[3] etc. for separations, filtration, catalyst supports, and scaffolds for tissue engineering. As well, fullerenes self-organize with molecular-scale precision into arrangements at multiple length scales and over all three dimensions.[4] Colloidal films from fullerene building blocks are a promising platform for photonics as C_{60} has high refractive index (n ~ 2.2) and transparency ($\lambda > 560$ nm).[5]

Monodisperse fullerene colloids with tunable shape have been prepared using co-solvent precipitation of C_{60} from emulsified solvent-nonsolvent mixtures.[6] In this approach, the interdiffusion of the miscible liquids causes local supersaturation of fullerenes and particle nucleation. The molecular shape, fullerene solubility, solvent-antisolvent ratio, concentration, temperature, and mixing conditions influence the morphology and uniformity of the microcrystals. [7–9] For example, diverse colloid shapes have been prepared such as fibers, hexagonal platelets, spherocylinders, ellipsoids, and cubes, to name a few.[7,8,10] However, the production of such fullerene colloids in sufficient quantities for use as building blocks in self-assembly remains a challenge. Recently, the structure-directing amphiphile 2,4,6-trimethylpyridine has been applied in mixed solvent systems to expand the range of solvents with the capacity for scaling the synthesis of fullerene colloids.[11]

A challenge for self-assembly of anistropic colloids lies in the ability to control particle orientation, localization, and registry. Several approaches have been used to enhance the organization of anisotropic particles and expand the library of structures for these building blocks. For example, shear flows, electric fields, and magnetic fields align and orient colloidal suspensions; confinement between hard walls modifies the free volume landscape; and patchy particles exhibit selective coordination and high anisotropy in the interparticle potential. [12–14] In particular, electric fields have been applied to induce martensitic transitions,[15] binary superlattices,[16] centered-rectangular monolayers,[17] string fluids,[18–20] liquid crystals,[18,19,21] and lock-and-key couplings[22]. Even more complex processes are being pioneered in directed-asssembly, for example, switching between plastic crystals and body-centered cubic crystals has been achieved by manipulating E-field and double layer interactions.[23] However, only a handful of studies address electric field-directed assembly strictly in two dimensions. [24]

Here, we report the hierarchical assembly of C_{60} from nanoscale to macroscopic two-dimensional films. C_{60} colloids are grown in relatively large quantities using seeded co-solvent precipitation with solvent mixture (1,2,3,4-tetrahydronaphthalene/ 2,4,6-trimethyl-pyridine) and antisolvent 2-propanol. The fullerene solutions are aged under illumination to regulate the free monomer concentration *via* C_{60} aggregation into nanoparticle seeds. Diverse morphologies with high monodispersity are prepared and a 30-70% increase in quantity as compared to previous studies is acheived. The platelet-shaped C_{60} particles are confined in wedge cells and are assembled under alternating current electric field. In general, confinement in a wedge cell produces a cascade of phase transitions with cell height, since the gap size becomes incommensurate with integral layer numbers.[25] We observe reorientation of the platelets from in-plane to largely out-of plane on the transition from one to two layers. A wide range of structures were found including hexagonal, oblique, string fluid, hexagonal-rhombic

coexistence, and tetratic-like phases as a function of field strength, frequency, and system density. The complex crystal structures and partial orderings demonstrated here are appealing as templates for photonic crystals and mesophases and fall within the range of complex crystalline structures to partial order phases. Furthermore, this work demonstrates the enhanced structural diversity resulting from the tandem use of electric fields and confinement on anisotropic particle systems.

Results and Discussion

Solvated C_{60} microcrystals were prepared by addition of the fullerene solutions (C_{60}/THN/TMP) to well-stirred vials of 2-propanol or ethanol. Due to its high fullerene solubility (14.5 g L^{-1} at 22 °C)[26] and moderate viscosity, THN was selected as the good solvent. Figure 5.1(a) displays polydisperse submicron (100-500 nm) particles prepared in ethanol at relatively high fullerene concentration. The nucleation of fullerene colloids was observed immediately as the development of a characteristic yellow color and turbidity. Aging of the fullerene solution in a reflective chamber reduces the free monomer concentration due to fullerene aggregation (i.e, nanoparticle seed[27,28] formation) in the presence of polar solvent (i.e., TMP, dipole moment of 2.05 D, 20% v/v). Figure 5.1(b) shows monodisperse platelet-shaped particles precipitated in ethanol following aging of the fullerene solution under illumination in a reflective chamber. In this case, the color change and turbidity developed gradually following addition of the fullerene solution to the poor solvent. The fullerene aggregates seed the growth of microcrystals promoting monodispersity, while the reduced free monomer concentration slows growth. The microcrystal growth from aged fullerene solutions also enhanced the quantity of monodisperse particles produced by 30-70% for relatively concentrated fullerene solutions.
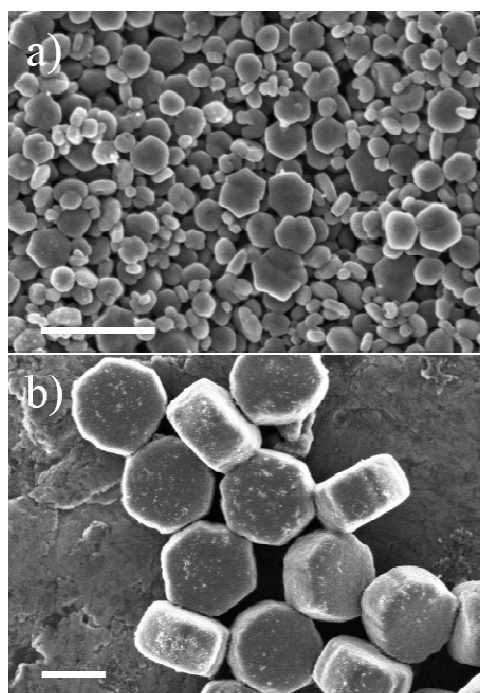
Figure 5.1. Effect of solution aging on fullerene solvate morphology, using ethanol as a poor solvent. a) Solvates prepared without aging; and b) aged 4 hours under 170 mW white light. Fullerene solutions are 2 mM C_{60} in THN with 20% v/v TMP. Injected volumes are 300 uL. Scale bars represent 1 μm.
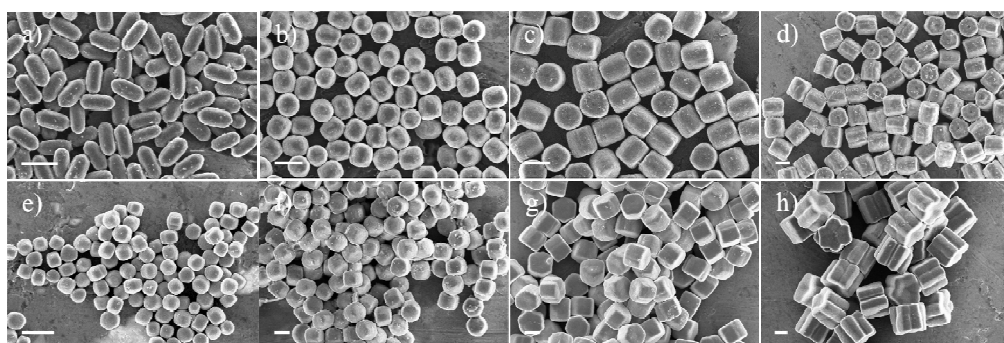
Figure 5.2. Systematic variation of particle morphology based on injected volume of fullerene solutions, using (a-d) 2-propanol and (e-h) 1:1 2-propanol/ethanol as poor solvents. Injected volumes are (a,e) 150 µL, (b,f) 300 µL, (c,g) 450 µL, and (d,h) 600 µL. Fullerene solution concentrations are 2.6 mM. Scale bars represent 1 µm.
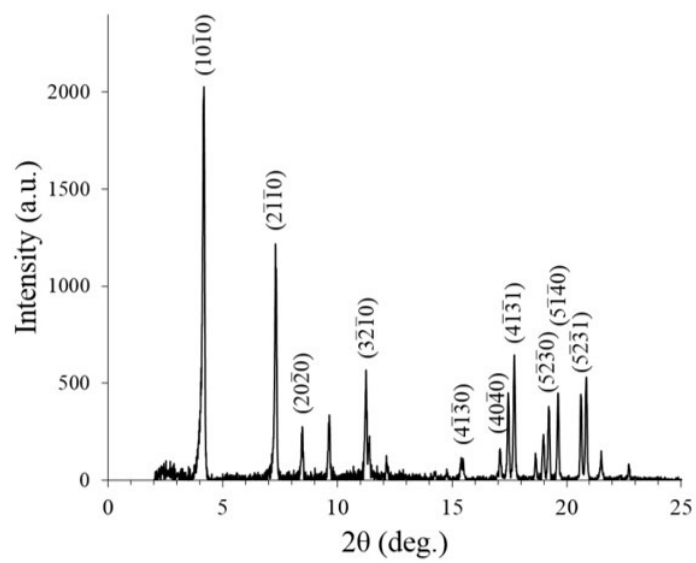
Figure 5.3. Powder x-ray diffraction pattern for C_{60}/THN/TMP solvates in Figure 5.2c.

Table 5.1. Particle size characteristics for C_{60} microparticles in Figure 5.2. CV is given as the standard deviation divided by the mean for at least 50 particles.

Sample	Length [μm]	Width [μm]	AR
2-a	0.959 (CV = 2.97%)	0.459 (CV = 5.67%)	2.09
2-b	0.896 (CV = 1.96%)	0.781 (CV = 3.66%)	1.15
2-c	1.13 (CV = 1.23%)	1.09 (CV = 2.74%)	1.04
2-d	1.52 (CV = 1.66%)	1.49 (CV = 2.24%)	1.02
2-e	0.457 (CV = 4.24%)	0.517 (CV = 8.24%)	0.88
2-f	1.14 (CV = 3.34%)	1.30 (CV = 4.17%)	0.88
2-g	1.30 (CV = 3.41%)	1.68 (CV = 3.71%)	0.77
2-h	2.16 (CV = 2.81%)	2.72 (CV = 3.99%)	0.80

Figure 5.2 provides SEM images of the fullerene microcrystal morphology as a function of injection volume of fullerene solutions in 2-propanol and 1:1 2-propanol/ethanol. For samples precipitated in 2-propanol, short rods and ellipsoids are formed at high and low injection volumes, respectively. The particle aspect ratios (ARs) decrease as the injection volume increases (Table 1). As well, higher monodispersity and faceting are found on increasing injection volume. With the poor solvent mixture 1:1 2-propanol/ethanol, particles had AR < 1 that varied little with injection volume. The C_{60} microcrystals were prepared in batch sizes of $\sim 5 \times 10^8$ particles. The characterization of internal structure by powder x-ray diffraction (Figure 5.3) indicated that the solvates had hexagonal crystal structures (space group $P6_3$) with lattice constants a = 2.38 nm and c = 1.05 nm.

The aging time to sufficiently reduce free monomer concentration in the fullerene solution is given by equation 1:

$$t_2 = t_1 \cdot \frac{C_2}{C_1} \cdot \frac{m_2}{m_1}$$
(Equation 5.1)

In practice, an initial co-precipitation was performed with a given poor solvent and light dose. If monodisperse microcrystals were obtained for a given aging time, mass of fullerenes, and solution concentration, then the above could be substituted in equation 1 as t_1, m_1 and C_1. The required aging time (t_2) under illumination (170 mW) is 1.3% of that in the dark. For aging times significantly longer than t_2, injection of the solution into alcohol did not yield microcrystals and no sedimentation was apparent over several months.

A solvatochromic effect was observed throughout the aging process as illustrated in Figure 5.4. The fullerene solution color changed from royal purple to dark reddish-brown, with corresponding changes in the optical absorption spectra. The spectra were normalized at 600 nm, the wavelength for a vibronic component of the symmetry-forbidden $S_1 \leftarrow S_0$ transition. Absorption intensity increased with aging time up to 12 hrs, most notably in the region of 425-600 nm. In this range, the absorption may be attributed to the promotion of
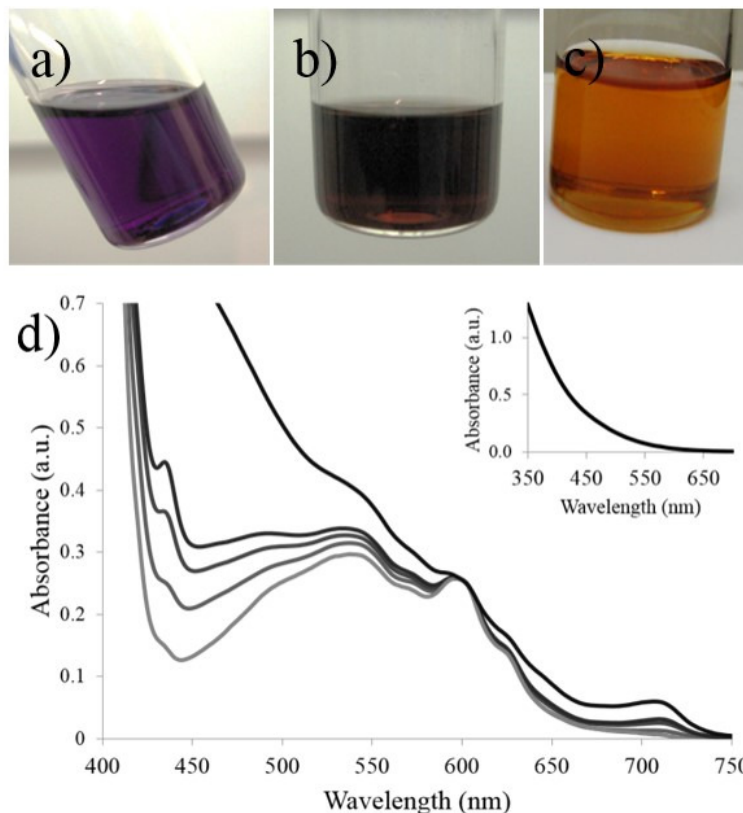
Figure 5.4. Color changes of aged fullerene solutions. a) C_{60}/THN/TMP solution prior to aging and b) after aging for 6 hours under light. c) Solution prepared from C_{60} in pure TMP aged for a month in the dark. d) Optical absorption spectra of C_{60}/THN/TMP solution (3 mM, 4:1 THN:TMP) aged under light. Spectra are normalized at 600 nm. Increasing absorption indicates 0, 2, 4, 6, and 12 hr aging times. Inset shows absorption spectrum for the solution in c).

intermolecular charge-transfer states due to fullerene aggregation.[29] Figure 5.5 shows the size

distribution (d > 30 nm) of nanoparticles as measured by nanoparticle tracking analysis. For 6

hrs aging time, the majority of the nanoparticle population had diameters less than 50 nm,

while at longer times (12 hrs) more particles were detected and the majority of the

nanoparticles had sizes less than 120 nm. In addition, the mode size may be smaller than 30

nm, i.e., below the detection limit of the instrument. Fullerene aggregation is assisted by the

formation of donor-acceptor complexes between electron-deficient C_{60} molecules and the

structure-directing agent.[7,8,29,30] The sensitivity of aging time to light exposure suggests that

an activation energy is involved with complex formation. Growth occurs from complexes to

clusters to nanoparticles. Amphiphilic TMP molecules become segregated to the perimeter of

the particles, resulting in a lyophilic core surrounded by a lyophobic shell.[31] As the

nanoparticles continue to grow, this stabilizing shell achieves greater coverage and eventually

causes the nanoparticles to form stable dispersions in polar solvents.[31–33]

The experimental schematic for the assembly of C_{60} platelets under confinement and

electric field is displayed in Figure 5.6(a) and 5.6(b). The particle solution was injected into

the confinement cell, and centrifuged to concentrate the particles in the monolayer height

region. Particle assembly was observed *in situ* between the electrodes with a microscope. The

electric field (amplitude E_o) was applied in the plane of the monolayer, resulting in dipolar

interactions between the platelets. Figure 5.6(c) shows the frequency-dependence of the

effective polarizability of C_{60} platelets in the solvent, as determined by the real component of

the Clausius-Mossotti factor $(Re|K(\omega)|)$,[34] where—

$$K(\omega) = \frac{\varepsilon_p^* - \varepsilon_s^*}{\varepsilon_p^* + 2\varepsilon_s^*}.$$
`(Equation 5.2)

The complex permittivity is given by $\varepsilon^* = \varepsilon - \frac{i\sigma}{\omega}$ where ε is the dielectric constant, σ is the

conductivity and ω is the frequency of the applied field. ε_p^* and ε_s^* refer to the particle and
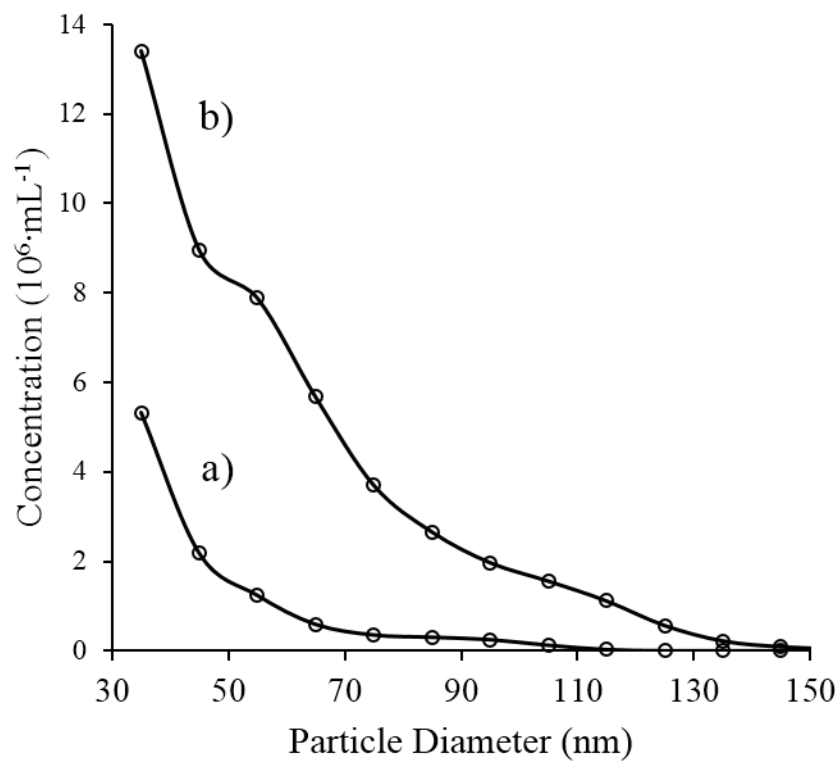
Figure 5.5. C_{60} nanoparticle size distribution observed by nanoparticle tracking analysis. 3 mM C_{60} in 4:1 THN/TMP, aged under 170 mW white light for a) 6 hr and b) 12 hr.
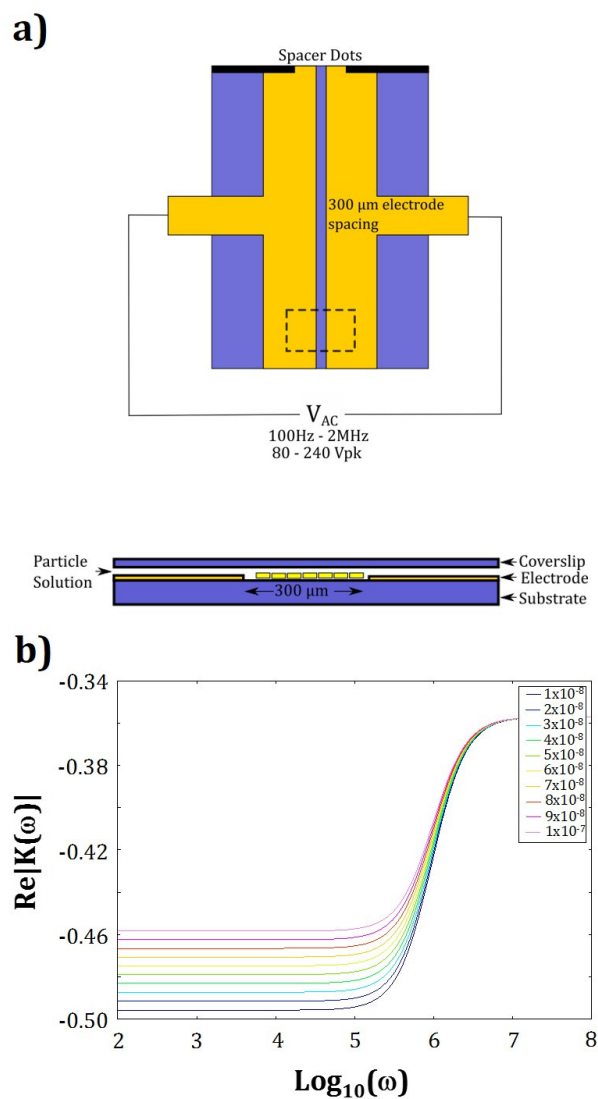
Figure 5.6. a) Schematic of electric field confinement cell with a top- and side view. The region of monolayer-confined assembly is outlined by a dotted line. Electrodes are attached via soldered wire to an AC voltage source. Particles (not to scale) are shown on side view within the region between the electrodes. **b)** Real component of the Clausius-Mossotti factor ($Re|K(\omega)|$) for C_{60} platelets as a function of electric field frequency. Colored lines represent $Re|K(\omega)|$ for particle conductivity values at intervals of 10^{-8} (S/cm).

solvent, respectively. For the calculation of $Re|K(\omega)|$, fluid values were measured and the static dielectric constant for C$_{60}$ from reference [35] was used. Conductivity of the particles was calculated from the Maxwell-Wagner charge relaxation time $\tau_{MW} = \frac{\varepsilon_p + \varepsilon_s}{\sigma_p + 2\sigma_s}$ which is inversely proportional to the crossover frequency (f_c). This curve suggests that the system should demonstrate a transition in self-assembly behavior at the crossover frequency, as the effective polarization of the particle in the medium sharply decreases in magnitude.

Dielectrophoretic forces on the particles due to gradients in the electric field distribution depend on the effective polarizability of the particles as shown below—

$$F_{DEP} = 2\pi\varepsilon_s Re|K(\omega)|V_p\nabla(\tfrac{E_o}{\sqrt{2}})^2 \qquad\qquad \text{(Equation 5.3)}$$

The dipole moment within a platelet can be estimated as—

$$p = 3\varepsilon_s\varepsilon_o Re|K(\omega)|V_p E_o \qquad\qquad \text{(Equation 5.4)}$$

where V_p is the volume of the particle. The dipole moment of the particle is anti-parallel with the applied field at all frequencies. A dimensionless prefactor that describes the relative strength of the dipolar interactions, γ, is defined as:

$$\gamma = \frac{9V_p}{2\pi}\frac{\varepsilon_s\varepsilon_o}{k_BT}Re|K(\omega)|^2\left(\frac{E_o}{\sqrt{2}}\right)^2 \qquad\qquad \text{(Equation 5.5)}$$

For this system, γ is equal to $5.3\times10^{-4}\,Re|K(\omega)|^2 E_o{}^2$ and lies in the range of [460, 8280]. Strictly, the Clausius-Mossotti relationship is derived for spherical particles; however, for anisotropic particles the internal electric field is not necessarily parallel to the applied field.[19]

The behavior of platelets confined to in-plane orientation at high packing fraction as a function of field strength and frequency below f_c is shown in Figure 5.7. Assemblies at 100 Hz and 10 kHz displayed dense hexagonal packing, as indicated by the inset fast Fourier transforms (FFTs). Large grains were apparent along with occasional dislocations and
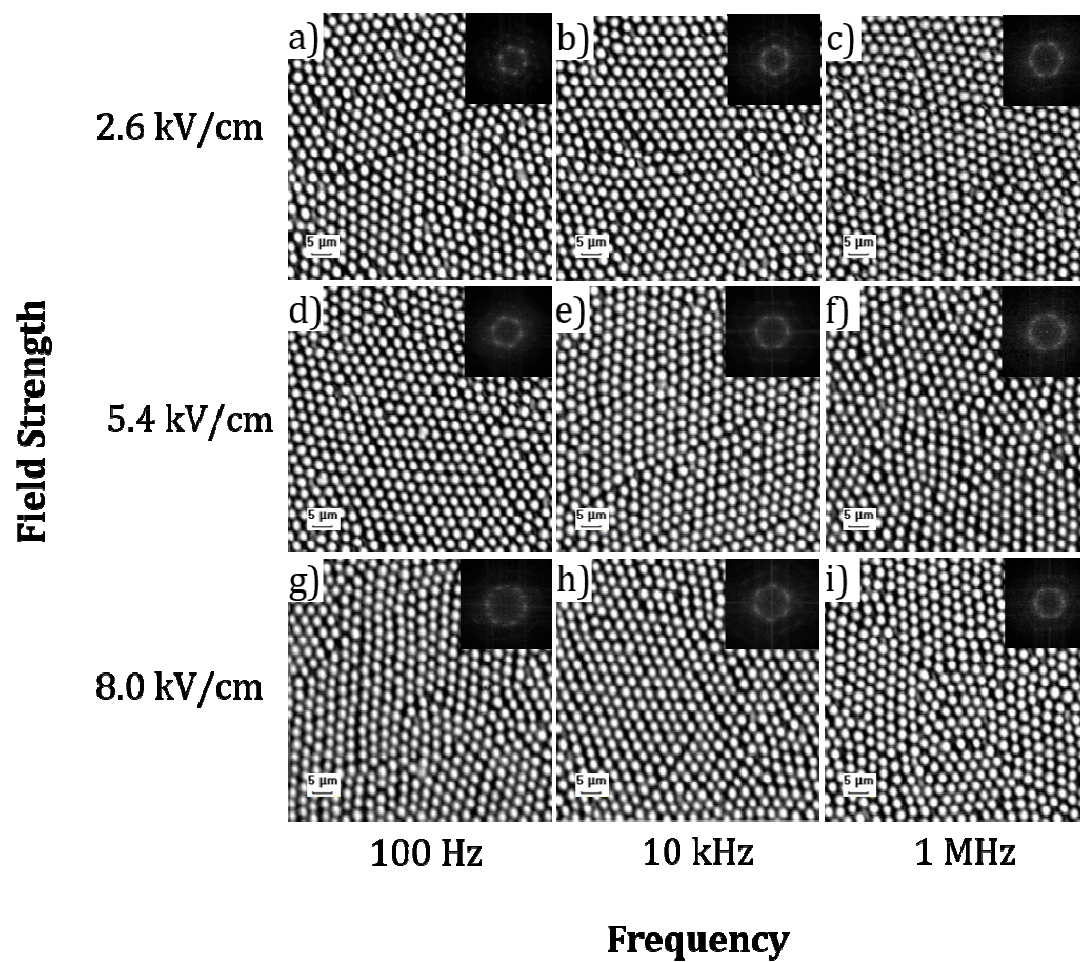
Figure 5.7. Assembly of platelets with in-plane monolayer confinement under electric field as a function of field strength and frequency for high volume fraction. FFTs are inset.

structured grain boundaries. The structured boundary configurations are due to repulsion for chains aligned across the boundary.[36] Optimal packing with large grain size occured for 5.4 kV/cm. As the frequency (field strength) is increased to 1 MHz (8 kV/cm), smaller grains were observed as illustrated by relatively diffuse rings in the FFTs.

Figure 5.8 displays the directed assembly of in-plane oriented platelets for intermediate packing fraction. Compared to the high packing fraction arrangements, the particles assembled at 2.6 kV/cm exhibited less order. As the field strength was increased to 5.4 kV/cm, dipolar interactions between the particles induced chaining, forming string fluids at all frequencies. Longer, more highly oriented chains were apparent for higher field strengths where the chaining force is greater.[34] As expected, chain coalescence was observed on a longer time scale than particle chaining and was dependent on the initial particle configuration when the E-field was applied.[36] In the strictly confined system, chains will only attract and coalesce if they are displaced with respect to each other by a particle radius, presumably due to the free energy cost to displace entire chains. We found that chains did not percolate or coarsen in the time scale of the experiments, in contrast to previous studies.[18]

Platelet assemblies at high packing fraction and with confinement allowing out-of-plane particle orientation are shown in Figure 5.9. The colloids arrange into oblique structures (i.e., out-of-plane particle orientation) for low field strengths and frequencies of 100 Hz and 10 kHz, as confirmed by the FFTs. As field strength is increased, the platelets preferentially re-orient to lie parallel to the substrate leading to the coexistence of hexagonal (in-plane particles) and oblique (out-of-plane particles) structures. The volume fraction was too high to allow all particles to re-orient. Hexagonal in-plane regions dominate for 100 Hz and 10 kHz at high field strength (8.0 kV/cm), and the FFTs display arcs of intensity in the hexagonal pattern. At 1 MHz the effective polarization of the particles is weaker and the overall assembly is more disordered. A number of forces may contribute to the in-plane particle

Figure 5.8. Assembly of platelets with in-plane monolayer confinement under electric field as a function of field strength and frequency for intermediate volume fraction. FFTs are inset.
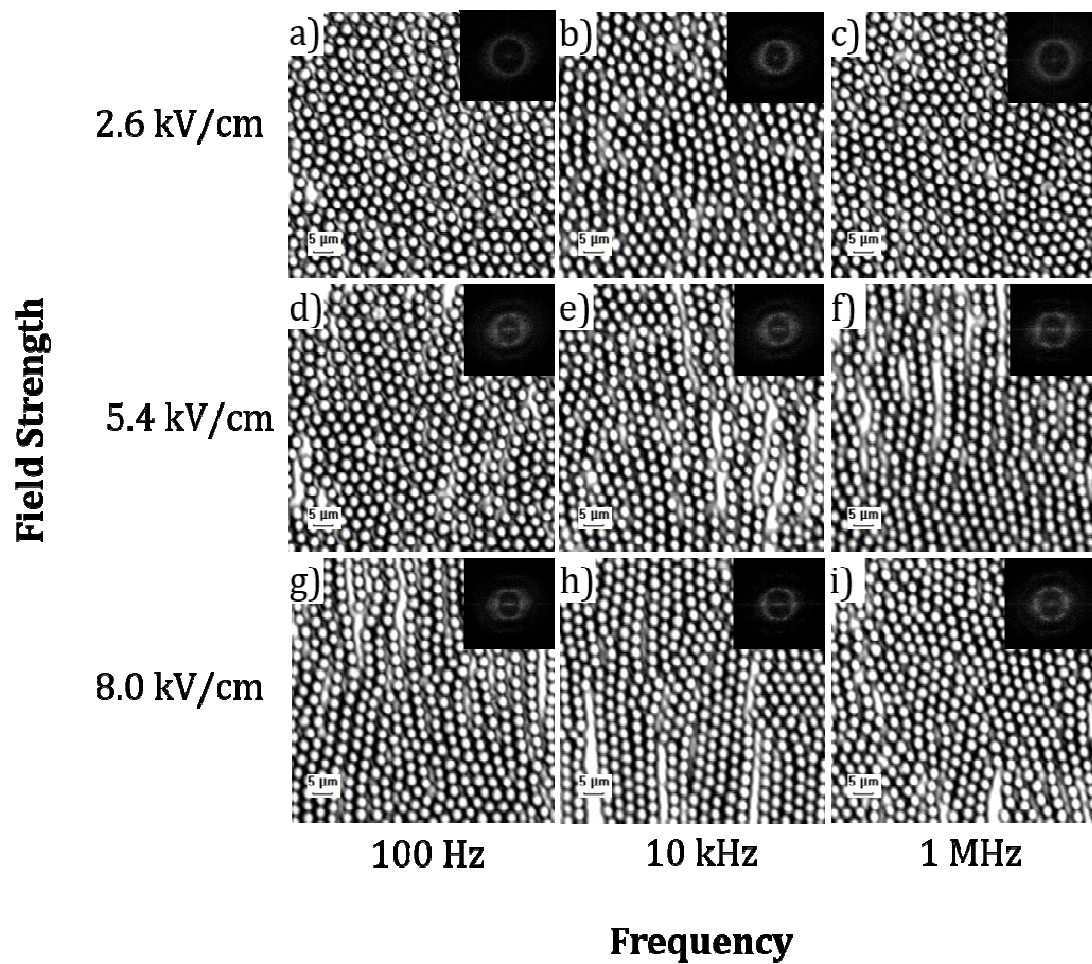
Figure 5.9. Assembly of platelets with out-of-plane monolayer confinement under electric field as a function of field strength and frequency for high volume fraction. FFTs are inset. White (light gray) particles are oriented in-plane (out-of-plane).

orientation at this gap height including isotropic and anisotropic dipolar particle interactions[37] and dielectrophoretic forces.[34]

Figure 5.10 displays the directed assembly for platetets at intermediate packing fraction and with out-of-plane confinement. For intermediate to high field strengths, larger grains of hexagonal order were observed as compared to those in Figure 5.9, which can be attributed to the enhanced free volume and the chaining force. The majority of particles had in-plane configurations at 5.4 kV/cm and 8 kV/cm and the particle chains readily coalesced. The increased crystallinity is illustrated in the FFT patterns. Chains of out-of-plane oriented platelets were common defects present in 100 Hz and 10 kHz assemblies.

Platelets assembled at low packing fraction are presented in Supplemental Figures 5.S1 and 5.S2. For particles confined in-plane (Figure 5.S1), isolated chains oriented along the E-field are predominate at moderate to high field strengths. FFTs show linear intensity perpendicular to the real space chains. For out-of-plane confinement (Figure 5.S2), chains show stronger coalescence because conformational changes are allowed including buckling, twisting and bending. FFTs from coalesced chains (8.0 kV/cm, 100 Hz) show a six-fold spot pattern, as expected. At high frequency and/or low field strength, the alignment in-plane was decreased and the structures became more disordered.

For frequencies above f_c, an electrohydrodynamic flow of platelets toward the electrode edge causes assembly. At high frequencies (above 1 MHz), field strength-dependent flow and dipolar interactions are the dominant forces controlling assembly. Electrical double layers typically can no longer respond to the field switching and so have a negligible effect.[38] Notably, we observe tetratic-like order for out-of-plane confinement [Figure 5.11(a)]. The particles preferentially orient out-of-plane and in-plane particles act as defects. We observed assembly at different particle flow velocities up to 4 μm/sec (controlled by the E-field strength), and tetratic-like structures were formed consistently. The long-range orientational
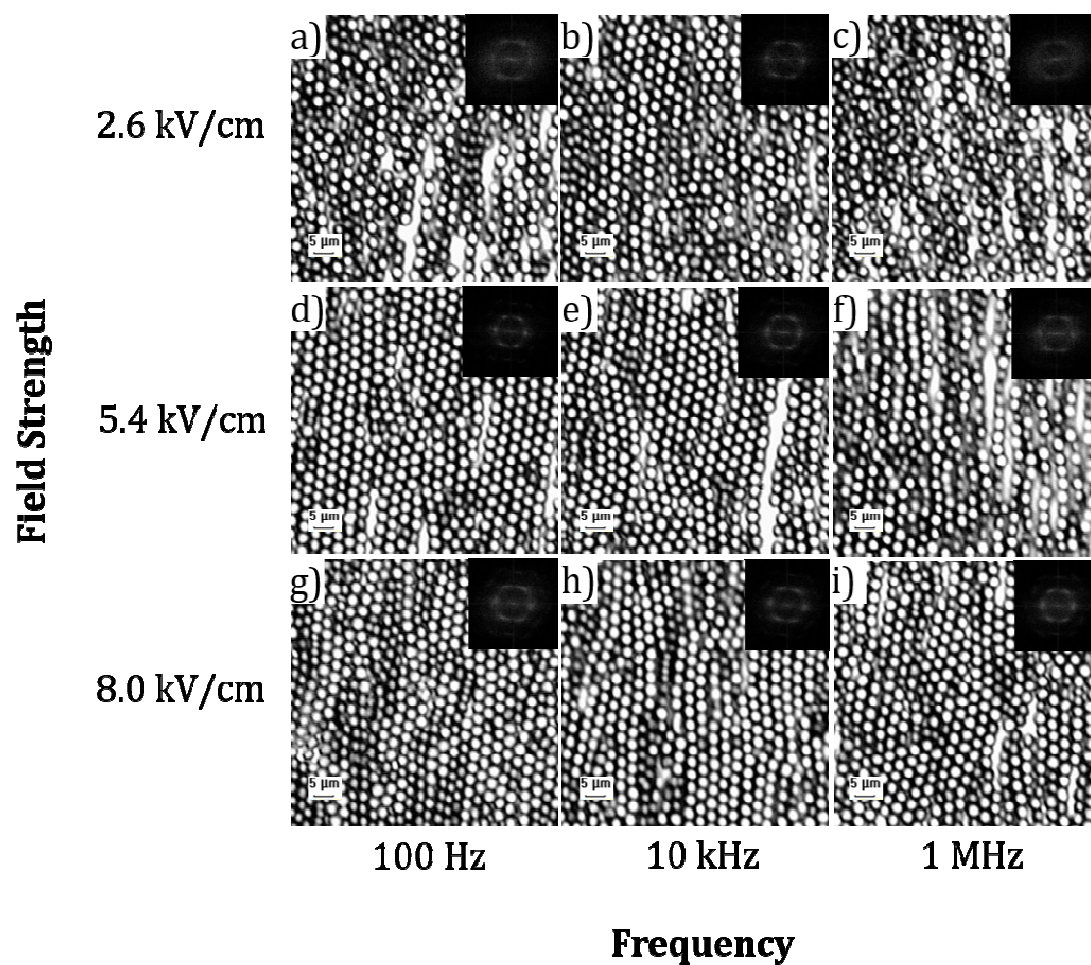
Figure 5.10. Assembly of platelets with out-of-plane monolayer confinement under electric field as a function of field strength and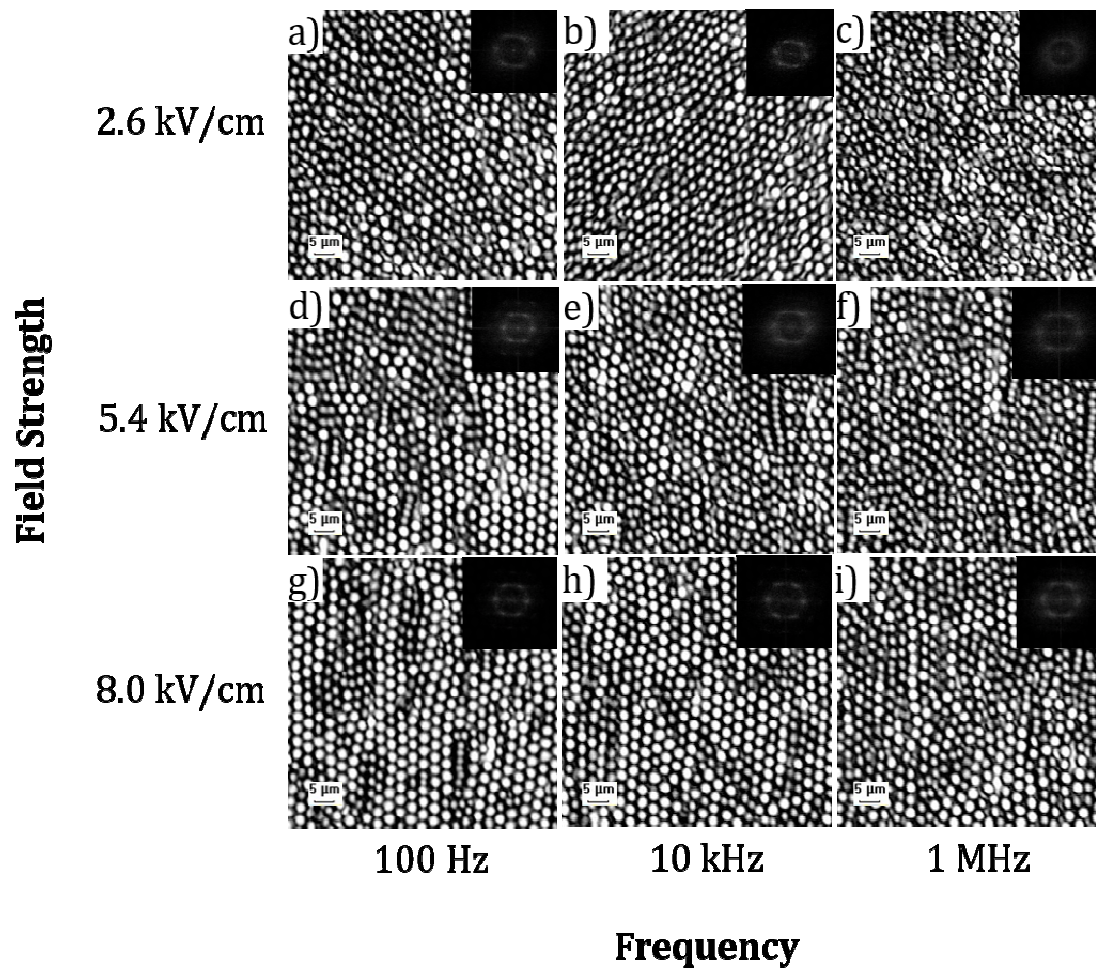 frequency for intermediate volume fraction. FFTs are inset. White (light gray) particles are oriented in-plane (out-of-plane).
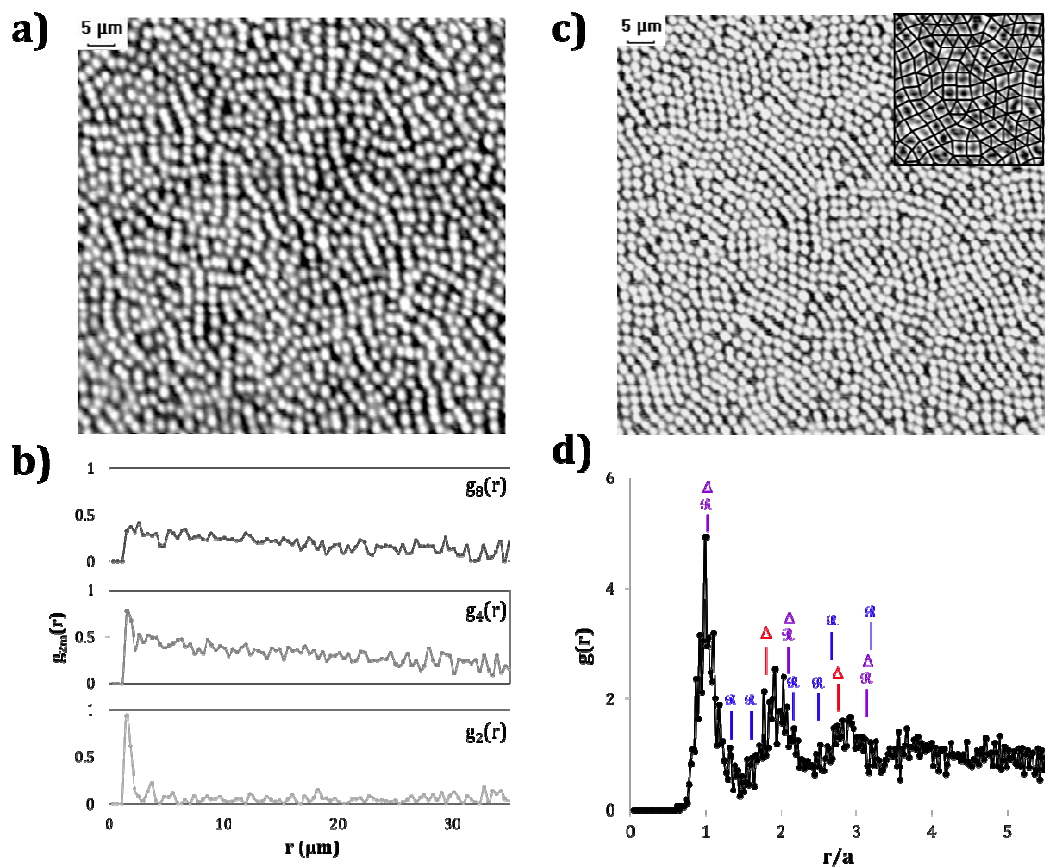
Figure 5.11. a) Assembly of platelets with out-of-plane confinement under electric field into a tetratic-like phase at 2 MHz, 5.4 kV/cm. **b)** Orientational correlation functions $g_{2m}(r)$ with m = 1, 2 and 4 for the image in a). **c)** Assembly of platelets with in-plane confinement under electric field into coexistent hexagonal-rhombic packings at 2 MHz, 5.4 kV/cm. **d)** Radial distribution function g(r) with hexagonal (red), rhombic (blue) and hexagonal-rhombic overlapping (purple) peaks labeled. Rhombic angle is $\varphi = 80°$.

114

order of the tetratic state was characterized by the orientational correlation function

$$g_{2m}(r) = \langle cos\{2m[\theta(0) - \theta(r)]\}\rangle,$$ where m = 1, 2, 3 corresponds to nematic, tetratic, hexatic order. The correlation functions $g_4(r)$ and $g_8(r)$ in Figure 5.11(b) demonstrate long range decay, confirming tetratic order. The faster decay of $g_8(r)$ occurs due to its high angular sensitivity. The rapid decay of $g_2(r)$ indicates a lack of nematic order in the system. The tetratic phase has been predicted for cubes and 'dominoes' but it has rarely been observed in experiment. One such study found columnar and 'almost-tetratic' order for photoresist platelets oriented out-of-plane by electric fields perpendicular to the substrate.[39]

The assembly of in-plane confined platelets for frequencies above f_c yielded hexagonal and rhombic phase coexistence as shown in Figure 5.11(c). The inset of Figure 5.11(c) outlines the particle bonds to clarify the hexagonal and rhombic regions. The pair correlation function for the structure is given in Figure 5.11(d), with the peaks marked for hexagonal (Δ) and high-angle rhombic ($\mathscr{R}$) ($\varphi = 80°$) ideal crystals. Peaks and troughs in the experimental plot match the predicted peak distributions. Both rhombic and hexagonal grain sizes are slightly increased by slower flow rates and lower field strengths.

Conclusion

In summary, monodisperse fullerene microcrystals are obtained with diverse morphologies using seeded co-solvent precipitation from fullerene solutions (C_{60}/THN/TMP) aged under illumination. We use THN as the good solvent because its high fullerene solubility enables the production of microcrystals in greater quantities as compared to previous studies. In the presence of TMP, aging under illumination reduces the free monomer concentration via fullerene aggregation into nanoparticles. Donor-acceptor complexes between C_{60} molecules and TMP aid the development of aggregates. These nanoparticles serve as seeds for the

growth of monodisperse microcrystals on addition to the poor solvent. Additionally, regulating the free monomer concentration slows growth and promotes colloid uniformity. Our method thus stabilizes the crystallization of fullerene solvates from relatively concentrated solutions and increases the quantity of particles obtained by 30-70%.

Hierarchically ordered films from these C_{60} platelets are organized via electric field and confinement. Strong dipolar interactions induce order for high field strengths and additional weaker effects are observed for changes in frequency. Transitions from crystalline phases (i.e., hexagonal and oblique) to string fluids arise from lowering volume fraction for both in-plane and out-of-plane confined platelets. Phase transitions also occur at a critical crossover frequency, f_c, where the effective polarizability of the platelets in the medium drops dramatically. Above f_c, assembly behavior is influenced by electrohydrodynamic flows and dipolar interactions, resulting in tetratic-like mesophases and hexagonal-rhombic phase coexistence. This system is particularly appealing for photonic applications due to the diverse phase behavior as a function of assembly conditions, as well as the optical characteristics of the C_{60} building blocks, which possess a high refractive index and and transparency ($\lambda > 560$ nm).[5] Further modeling and theoretical work to elucidate fully the mechanisms of assembly at frequencies above f_c would be useful.

Methods

A 10 mL aliquot of 2-propanol (Sigma-Aldrich, >99.8%) or ethanol (Emplura, >99.5%) was stirred at 500 rpm in a scintillation vial. Fullerene C_{60} (Sigma-Aldrich, >99.9%) was dissolved in THN [(1,2,3,4-tetrahydronaphthalene), Sigma-Aldrich, 99%] in an ultrasonic bath. 2,4,6-trimethylpyridine (Sigma-Aldrich, 99%) was added, and solutions were homogenized with a vortex mixer. Fullerene solutions were placed inside a reflective chamber, and illuminated using a set of three white LEDs in series (ThorLabs LEDWE-15, 8.5

V, 10 mA). After an appropriate aging time, fullerene solutions were added to the alcohol to induce microcrystal nucleation, observed as an onset of turbidity and a characteristic color. The vial was removed from stirring for 5 s, then returned to stirring for 10 s. The stirring bar was removed and the dispersion was left uncapped to evaporate excess alcohol for 24 h. Samples were resuspended via sonication and purified by centrifugation and reconstitution in fresh alcohol.

The morphology of the fullerene microcrystals was examined using scanning electron microscopy (FE-SEM, Zeiss Ultra 55, 2.3 kV). The crystal structures were evaluated using powder X-ray diffraction (XRD, Scintag PAD-X, Cu K_α). Optical absorption measurements were conducted using a UV-vis-NIR spectrometer (Shimadzu UV-3600). Nanoparticle tracking analysis was performed using a Malvern NS300.

To fabricate the electrode substrates, borosilicate wafers were patterned with Au electrodes with 300μm spacing. A 10 nm Cr adhesion layer and 40 nm Au were deposited via thermal evaporation (CHA thermal evaporation system). Each wafer yielded two substrates, and wafers were partitioned with a laser engraver (Versalaser VSL3.50). Substrates were soaked in acetone for a minimum of one day and adhered to 2 in. x 3 in. glass slides for enhanced mechanical stability. Prior to cell assembly, substrates and coverslips (24 x 50 mm coverslip, VWR) were washed in isopropanol, soap and 18.2 M□ de-ionized water and dried with nitrogen. A row of spacer dots (cured Norland UV adhesive) was deposited at the top of the substrate. The bottom edge (i.e., zero confinement height) was lined with cyanoacrylate (Insta-cure+, Bob Smith Industries) and the coverslip was overlaid. Pressure was applied by two magnets (10 lb-pull) along the bottom edge. The sides of the cell were sealed with 5-minute epoxy (Devcon). The adhesives were allowed to cure for several hours. Confinement cells were plasma cleaned (Harrick Plasma) for 30 seconds to remove organics from the surface.

C_{60} platelets were tumbled in 2.3 mM solution of 40,000 MW Polyvinylpyrrolidone (Sigma Aldrich) in isopropanol overnight to prepare them for assembly. A 20 μL aliquot of particle solution (concentration 6 x 10^8/mL) was filled into the cell. The cell opening was wrapped with Parafilm to prevent leaking and evaporation. Cells were centrifuged in a custom-built holder at 1500 rpm for 2-6 hours.

Confinement cells were imaged during electric field-induced assembly using a BX-51 Olympus microscope in bright field transmission mode at 100x magnification. Leads were attached to the electrodes using lead-tin solder, and fields were applied using a function generator (Tektronix), and a wide-band power amplifier (Krohn-White Corp. 7602M). Electric fields were applied for 2-6 minutes for low-frequency experiments, with periods of 1-5 minutes between experiments. In these periods, short pulses of low voltage and frequency fields (2 Hz, 2.6 kV/cm) were utilized to induce oscillatory osmotic currents that returned particle disorder to the system. Electric fields were applied in order of increasing voltage and increasing frequency. Assembly was observed more than 20 μm from the electrode edge to avoid regions with strong field gradients.

The crossover frequency was determined by examining the electrode edge and observing the particle behavior transition from attractive to repulsive with respect to the electrode. The crossover frequency (f_c) observed was 1.8 MHz (+/- 0.1 MHz) for field strength 5.4 kV/cm. The conductivity of the medium was predicted to be 1.75 x 10^{-6} S/cm at field strength of 5.4 kV/cm from control experiments performed on polystyrene colloids (Duke Scientific). The static dielectric constant of the medium was measured as 1.7 x 10^{-12} F/cm.

ImageJ was used to process images, produce fast Fourier transforms (FFTs), and calculate particle flow velocity. Matlab graphical input was used to calculate the radial distribution functions and orientational correlation functions.

Figure 5.S1. Assembly of platelets with in-plane monolayer confinement under electric field as a function of field strength and frequency for low volume fraction. FFTs are inset.
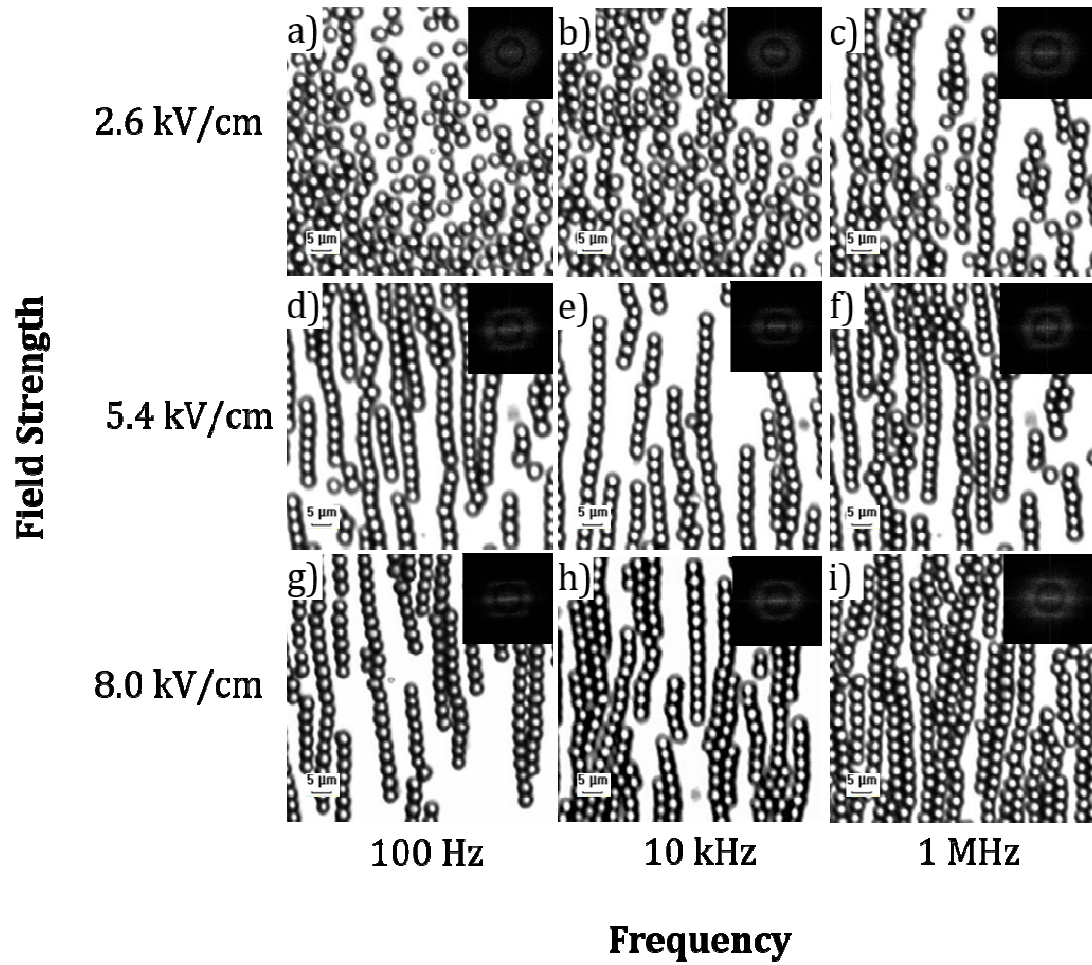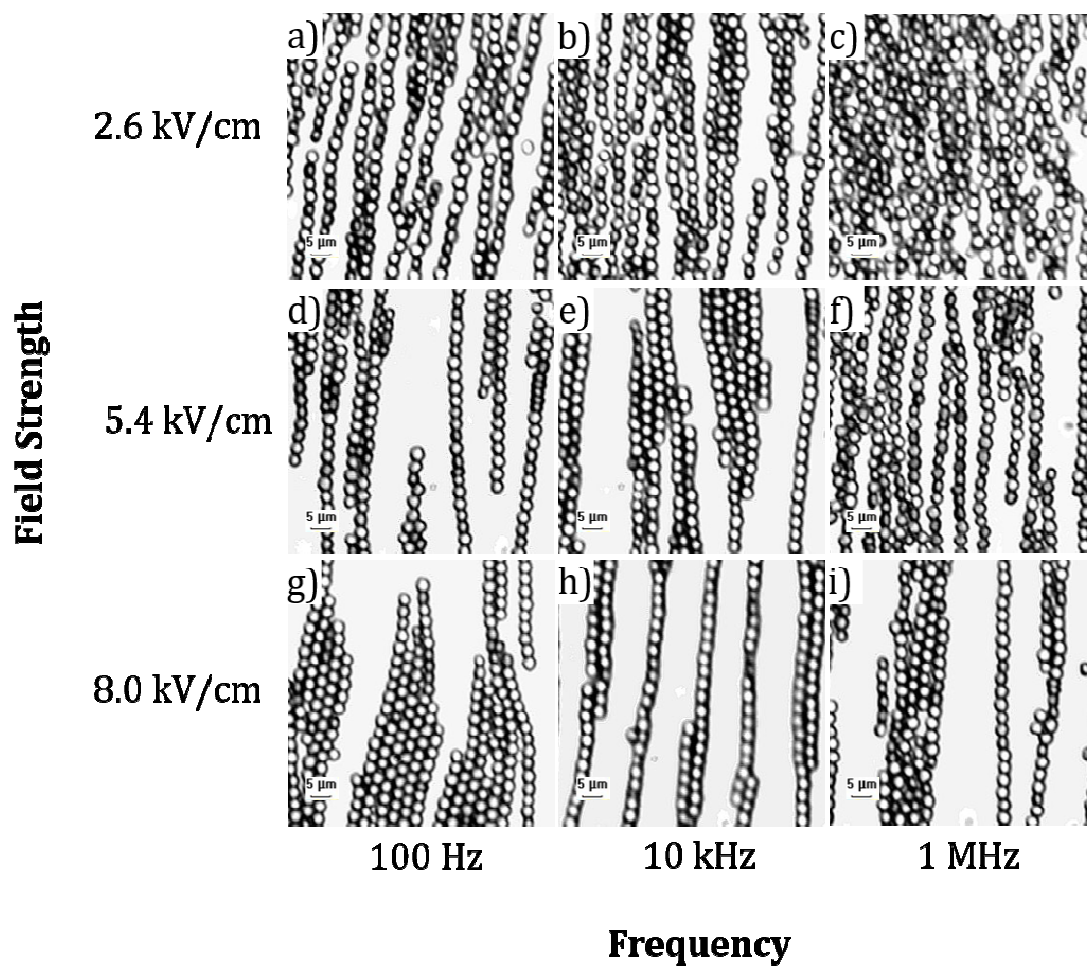
Figure 5.S2. Assembly of platelets with out-of-plane monolayer confinement under electric field as a function of field strength and frequency for low volume fraction. FFTs are inset. White (light gray) particles are oriented in-plane (out-of-plane).

REFERENCES

[1]   H. Sai, K. W. Tan, K. Hur, E. Asenath-Smith, R. Hovden, Y. Jiang, M. Riccio, D. a
        Muller, V. Elser, L. a Estroff, S. M. Gruner, U. Wiesner, *Science (80-.).* **2013**, *341*,
        530.

[2]   L. Xie, H. Xu, Z. M. Li, M. Hakkarainen, *Macromol. Rapid Commun.* **2016**, 745.

[3]   T. C. Keller, K. Desai, S. Mitchell, J. Pérez-Ramírez, *ACS Catal.* **2015**, *5*, 5388.

[4]   L. K. Shrestha, Q. Ji, T. Mori, K. Miyazawa, Y. Yamauchi, J. P. Hill, K. Ariga, *Chem.
        - An Asian J.* **2013**, *8*, 1662.

[5]   H. Kataura, Y. Endo, Y. Achiba, K. Kikuchi, T. Hanyu, S. Yamaguchi, *J. Phys. Chem.
        Solids* **1997**, *58*, 1913.

[6]   R. G. Alargova, S. Deguchi, K. Tsujii, *J. Am. Chem. Soc.* **2001**, *123*, 10460.

[7]   J. Jeong, W. S. Kim, S. I. Park, T. S. Yoon, B. H. Chung, *J. Phys. Chem. C* **2010**, *114*,
        12976.

[8]   A. Masuhara, Z. Tan, H. Kasai, H. Nakanishi, H. Oikawa, *Jpn. J. Appl. Phys.* **2009**, *48*,
        502061.

[9]   †,‡ Heng-Xing Ji, † Jin-Song Hu, †,‡ Qing-Xin Tang, † Wei-Guo Song, † Chun-Ru
        Wang, † Wen-Ping Hu, *,† and Li-Jun Wan, § Shuit-Tong Lee*, **2007**, DOI
        10.1021/JP071912R.

[10]   J. Hong, D. S. Yoon, M. Il Park, J. Choi, T. S. Kim, G. Im, S. Kim, Y. Eugene Pak, K.
        No, *Japanese J. Appl. Physics, Part 1 Regul. Pap. Short Notes Rev. Pap.* **2004**, *43*,
        5639.

[11] S. J. Penterman, C. M. Liddell Watson, *CrystEngComm* **2016**, *18*, 1775.

[12] H. Loewen, *Eur. Phys. J. Spec. Top.* **2013**, *222*, 2727.

[13] S. Gangwal, A. Pawar, I. Kretzschmar, O. D. Velev, Velev, O. D., *Soft Matter* **2010**, *6*, 1413.

[14] E. K. Riley, C. M. Liddell, *Langmuir* **2010**, *26*, 11648.

[15] A. F. Demirörs, P. M. Johnson, C. M. van Kats, A. van Blaaderen, A. Imhof, *Langmuir* **2010**, *26*, 14466.

[16] W. Ristenpart, I. Aksay, D. Saville, *Phys. Rev. Lett.* **2003**, *90*, 128303.

[17] A. A. Shah, H. Kang, K. L. Kohlstedt, K. H. Ahn, S. C. Glotzer, C. W. Monroe, M. J. Solomon, *Small* **2012**, *8*, 1551.

[18] J. Martin, J. Odinek, T. Halsey, R. Kamien, *Phys. Rev. E* **1998**, *57*, 756.

[19] H. R. Vutukuri, F. Smallenburg, S. Badaire, A. Imhof, M. Dijkstra, A. van Blaaderen, *Soft Matter* **2014**, *10*, 9110.

[20] J. P. Singh, P. P. Lele, F. Nettesheim, N. J. Wagner, E. M. Furst, *Phys. Rev. E. Stat. Nonlin. Soft Matter Phys.* **2009**, *79*, 50401.

[21] N. Osterman, D. Babič, I. Poberaj, J. Dobnikar, P. Ziherl, *Phys. Rev. Lett.* **2007**, *99*, 1.

[22] M. Kamp, N. A. Elbers, T. Troppenz, A. Imhof, M. Dijkstra, R. van Roij, A. van Blaaderen, *Chem. Mater.* **2016**, acs. chemmater.5b04152.

[23] B. Liu, T. H. Besseling, M. Hermes, A. F. Demirörs, A. Imhof, A. van Blaaderen, *Nat. Commun.* **2014**, *5*, 3092.

[24]   a. Blaaderen, M. Dijkstra, R. Roij, A. Imhof, M. Kamp, B. W. Kwaadgras, T. Vissers,

B. Liu, *Eur. Phys. J. Spec. Top.* **2013**, *222*, 2895.

[25]   A. Reinmueller, E. C. O??uz, R. Messina, H. Loewen, H. J. Sch??pe, T. Palberg, *Eur. Phys. J. Spec. Top.* **2013**, *222*, 3011.

[26]   K. N. Semenov, N. A. Charykov, V. N. Keskinov, *J. Chem. Eng. Data* **2011**, *56*, 230.

[27]   N. Stock, S. Biswas, *Chem. Rev.* **2012**, *112*, 933.

[28]   M. Okubo, H. Minami, K. Morikawa, *Colloid Polym. Sci.* **2001**, *279*, 931.

[29]   S. Bhattacharya, M. Banerjee, A. K. Mukherjee, *Spectrochim. Acta Part A Mol. Biomol. Spectrosc.* **2003**, *59*, 3147.

[30]   Lin Wang, * Bingbing Liu, Shidan Yu, Mingguang Yao, Dedi Liu, Yuanyuan Hou, and Tian Cui, G. Zou, B. Sundqvist, Han You, and Dingke Zhang, D. Ma, **2006**, DOI 10.1021/CM060997Q.

[31]   a Mrzel, a Mertelj, a Omerzu, M. Copic, D. Mihailovic, *J. Phys. Chem. B* **1999**, *103*, 11256.

[32]   V. Aksenov, T. Tropin, O. Kyzyma, M. Avdeev, M. Korobov, L. Rosta, *Phys. Solid State* **2010**, *52*, 1059.

[33]   T. V. Tropin, M. V. Avdeev, O. A. Kyzyma, V. L. Aksenov, *Phys. Status Solidi Basic Res.* **2010**, *247*, 3022.

[34]   O. D. Velev, in *Colloids Colloid Assem.* (Ed: F. Caruso), **2004**, pp. 437–464.

[35]   A. F. Hebard, R. C. Haddon, R. M. Fleming, A. R. Kortan, *Appl. Phys. Lett.* **1991**, *59*, 2109.

[36]   R. Tao, J. Sun, *Phys. Rev. Lett.* **1991**, *67*, 398.

[37]   B. W. Kwaadgras, M. Verdult, M. Dijkstra, R. Van Roij, *J. Chem. Phys.* **2011**, *135*, DOI 10.1063/1.3637046.

[38]   A. Kuijk, T. Troppenz, L. Filion, A. Imhof, R. van Roij, M. Dijkstra, A. van Blaaderen, *Soft Matter* **2014**, *10*, 6249.

[39]   K. Zhao, C. Harrison, D. Huse, W. B. Russel, P. M. Chaikin, *Phys. Rev. E - Stat. Nonlinear, Soft Matter Phys.* **2007**, *76*, 1.

CHAPTER 6

CONCLUSION

The complex structure and ordering that are accessible *via* colloidal templates present an avenue for enhanced photonic properties including larger bandgaps, slow light and negative refraction. To date, PC research has been focused primarily on properties and applications in two-dimensional crystals designed to be fabricated using lithographic patterning (i.e., uniform cross-section and one component systems). By expanding the scope of computational studies to include systems inspired by complex self-assembled systems, a deeper understanding of structure-property relationships in photonic crystals can be achieved. In particular, recent advances in PC theory indicate that crystallinity is not a pre-requisite to promote photonic bandgaps.[1] Initial studies of disordered photonic systems have focused exclusively on translational disorder,[1,2] but self-assembled systems generate a wide range of partial order structures combining translational and orientational order and disorder that may possess unique photonic properties.[3–5] Furthermore, properties beyond bandgaps including slow light and negative refraction have not been investigated in disordered photonic systems. Systematic studies that investigate both the photonic properties (e.g. photonic bandgap, slow light, etc.) and the physical origin of the photonic bandgap in systems with diverse ordering are necessary to understand the effect of disorder in photonic systems.

Self-assembly has been used to create crystalline and partial order structures from diverse particle morphologies at low cost and over large areas.[5–9] These structures form *via* a variety of assembly effects including confinement, electric and magnetic fields, shear flows,

and enthalpic particle interactions. However, reports investigating the photonic bandgap properties of colloidal crystals beyond the simplest opal structure are limited.[10–12] This thesis seeks to investigate novel self-assembly techniques for photonic applications and to explore diverse photonic properties in systems that can be manufactured using self-assembled colloidal templates. This thesis points self-assembly researchers toward high payoff structures for photonic applications.

Chapters 2-4 of this thesis systematically investigated three different classes of structure accessible through self-assembly: crystals with complex basis, semi-regular tilings, and mesophases. The square bilayer slab PC investigated in Chapter 2 had the unique feature of a complex basis shape with variation in cross section. The structure has been demonstrated using mushroom cap-shaped particles assembled under confinement.[13] Large photonic bandgaps were supported over a wide range of materials and structural parameters, and negative refraction was demonstrated. The distribution of the displacement field in the structure was examined to determine the Bragg scattering nature of the photonic bandgap and to elucidate the dependence of the bandgap size on the degree of particle anisotropy. This finding confirmed that the reduction of particle symmetry was key in promoting large photonic bandgaps. This study demonstrates that self-assembled slab structures support photonic bandgaps on par with the champion structures designed using lithography, and that reduced basis symmetry paired with high lattice symmetry results in enhanced photonic properties.

Chapter 4 investigated a semi-regular $3^2 \cdot 4 \cdot 3 \cdot 4$ Archimedean tiling inspired by self-assembly of binary colloidal mixtures. The high rotational symmetry (almost 12-fold) of this semi-regular tiling has been shown to support isotropic bandgaps that have been applied in enhancing LED out-coupling.[14,15] Previous models have consisted of circular rods at the apex

of the triangular and square motifs. Here, the model structure was a shape-binary system comprised of triangle and square rods with independently varied materials properties (i.e. dielectric constant). Mode field distributions indicated this semi-regular symmetry supported bandgaps originating both from Lorenz-Mie and Bragg scattering, dependent on the distribution of the high dielectric within the structure. Large bandgaps originated from Lorenz-Mie scattering for high dielectric particles in an air matrix (i.e., direct structures). For the inverted structures, large bandgaps arose due to the redistribution of the mode field into air pores or into complementary regions of high dielectric material. Additionally, slow light and atypical refraction properties were investigated and almost all angle negative refraction leading to sub-wavelength imaging, self-collimation, and slow light effects were predicted. This work demonstrates that frontier band-dependent properties are promoted in the Archimedean tiling structure as well as the band gap properties.

Disorder has been widely regarded as a hindrance to large photonic bandgaps. Variations in the radii of spheres or their random displacements from lattice sites in the inverse opal structure, reduce the band gap and disorder as small as 2% of the lattice constant completely closes it.[16] In Chapter 3, the impacts of orientational randomness were investigated for rotator crystals of cut-rods. Rotator crystals have translational periodicity and orientational randomness. The structure was a two-dimensional approximation of a cut-sphere assembly observed experimentally and predicted by Monte Carlo simulations.[17,18] Large, stable bandgaps with high gap isotropy in the inverted and direct structures were found as a function of cut fraction, dielectric contrast, and filling fraction. The Lorenz-Mie resonance induced bandgaps were insensitive to the degree of disorder and particle anisotropy, while Bragg scattering induced bandgaps varied in size as a function of disorder and system conformation. Additionally, slow light properties were investigated in waveguide geometry and slowdown factors larger than those for common PCs were predicted. This study

demonstrated that certain types of disorder enhance photonic properties and the work lies at the frontier of manipulating disorder for colloid-based photonics.

In Chapter 5, the synthesis and directed assembly of colloidal C_{60} microcrystals under electric field and confinement was presented. Fullerene molecular crystals were grown in quantities sufficient for assembly via seeded co-solvent precipitation. Diverse morphologies including platelets, rods and gear-shapes were prepared as a function of injection volume and fullerene solution concentration. Electric fields were applied to colloidal C60 platelets confined to two dimensions and the particles assembled under dipolar forces, dielectrophoretic forces and electrohydrodynamic flows. Structures formed as a function of field strength, frequency and confinement included hexagonal, oblique, string fluid, coexistent hexagonal-rhombic and tetratic. This work enhances fundamental understanding of how multiple assembly effects (electric fields and confinement) combine to promote control of particle position, orientation and registry in self-assembled systems for photonics.

A range of future research paths exist in the emerging field of disordered photonics as well as colloidal self-assembly. Of particular interest are the properties of Lorenz-Mie resonance induced bandgaps. Very recent reports investigate the properties of Mie resonances in dielectric nanostructured materials under the context of dielectric metamaterials, and show promising new properties including optical magnetism and refractive indices of zero.[19] This work builds heavily on findings from the photonic crystal community, and has not yet branched out to explore the impact of partial order or diverse building block morphology that self-assembled systems provide. Random lasing, a property that has been studied exclusively until now in truly disordered systems such as random colloidal glasses, is another promising application for self-assembled systems.[20] Until now, only the simplest spherical particles

have been investigated, and the impact of partial order and basis morphology on random lasing has not been explored.

In the context of self-assembling anisotropic basis morphologies, recent work has pointed toward the phase diversity promoted by the interaction of multiple assembly effects (e.g. electric field, enthalpic "patches", flow, confinement and more) applied to a single system.[7,21,22] However, such assemblies are technically challenging, and the thermodynamics of modelling these systems to understand the assembly is far more complex and computationally intensive. Research into the combinations of assembly effects in anisotropic particle systems has the potential for unprecedented control over particle orientation and position, to truly realize "programmable" assembled materials. This level of tunable structural control paired with the cost-effectiveness and scalability of self-assembled systems would enhance the viability of colloidal templates for frontier photonic applications.

REFERENCES

[1]   M. Florescu, S. Torquato, P. J. Steinhardt, *Proc. Natl. Acad. Sci. U. S. A.* **2009**, *106*, 20658.

[2]   J. F. Galisteo-López, M. Ibisate, R. Sapienza, L. S. Froufe-Pérez, A. Blanco, C. López, *Adv. Mater.* **2011**, *23*, 30.

[3]   A. Pal, J.-M. Meijer, J. R. Wolters, W. K. Kegel, A. V. Petukhov, *J. Appl. Crystallogr.* **2015**, *48*, 238.

[4]   S. Całus, B. Jabłońska, M. Busch, D. Rau, P. Huber, A. V. Kityk, *Phys. Rev. E - Stat. Nonlinear, Soft Matter Phys.* **2014**, *89*, 1.

[5]   K. Zhao, C. Harrison, D. Huse, W. B. Russel, P. M. Chaikin, *Phys. Rev. E - Stat. Nonlinear, Soft Matter Phys.* **2007**, *76*, 1.

[6]   S. Gangwal, A. Pawar, I. Kretzschmar, O. D. Velev, Velev, O. D., *Soft Matter* **2010**, *6*, 1413.

[7]   B. Liu, T. H. Besseling, M. Hermes, A. F. Demirörs, A. Imhof, A. van Blaaderen, *Nat. Commun.* **2014**, *5*, 3092.

[8]   K. Muangnapoh, C. M. Liddell, **n.d.**

[9]   B. Sun, H. Sirringhaus, *J. Am. Chem. Soc.* **2006**, *128*, 16231.

[10]   E. K. Riley, E. Y. Fung, C. M. Watson, *J. Appl. Phys.* **2012**, *111*, 93504.

[11]   T. T. Ngo, C. M. Liddell, M. Ghebrebrhan, J. D. Joannopoulos, *Appl. Phys. Lett.* **2006**,

88, 2.

[12] E. K. Riley, C. M. Liddell Watson, *J. Appl. Phys.* **2014**, *115*, DOI 10.1063/1.4880743.

[13] E. K. Riley, C. M. Liddell, *Langmuir* **2010**, *26*, 11648.

[14] M. Rattier, H. Benisty, E. Schwoob, C. Weisbuch, T. F. Krauss, C. J. M. Smith, R. Houdré, U. Oesterle, *Appl. Phys. Lett.* **2003**, *83*, 1283.

[15] D. Jovanović, R. Gajić, K. Hingerl, *Opt. Express* **2008**, *16*, 4048.

[16] Z.-Y. Li, J. Wang, B.-Y. Gu, *Phys. Rev. B* **1998**, *58*, 3721.

[17] E. Y. K. Fung, K. Muangnapoh, C. M. Liddell Watson, *J. Mater. Chem.* **2012**, *22*, 10507.

[18] C. Avendaño, C. M. Liddell Watson, F. a. Escobedo, *Soft Matter* **2013**, *9*, 9153.

[19] M. V. Rybin, D. S. Filonov, K. B. Samusev, P. A. Belov, Y. S. Kivshar, M. F. Limonov, *Nat. Commun.* **2015**, *6*, 1.

[20] P. D. García, R. Sapienza, á. Blanco, C. López, *Adv. Mater.* **2007**, *19*, 2597.

[21] S. Gangwal, O. J. Cayre, O. D. Velev, *Langmuir* **2008**, *24*, 13312.

[22] N. Osterman, D. Babič, I. Poberaj, J. Dobnikar, P. Ziherl, *Phys. Rev. Lett.* **2007**, *99*, 1.